

Ion Strings for Quantum Computation

Dissertation

zur Erlangung des Doktorgrades an der
naturwissenschaftlichen Fakultät
der Leopold-Franzens-Universität Innsbruck

vorgelegt von

Hanns-Christoph Nägerl

durchgeführt am Institut für Experimentalphysik
unter der Leitung von
o. Univ. Prof. Dr. R. Blatt

Innsbruck
September 1998

Abstract

This thesis reports on the setup of a new experimental apparatus for the storage and control of strings of Calcium ions to be used for quantum computation. The ions are trapped in a linear Paul trap, cooled and excited by laser light, and observed by detection of their fluorescence on a photon counting photomultiplier and on a highly sensitive CCD camera. High resolution spectroscopy of the narrow $S_{1/2} - D_{5/2}$ quadrupole transition is used to characterize the ions' motion in the trap and to test the possibility to use the $S_{1/2}$ and $D_{5/2}$ levels as a quantum bit for the application of fundamental quantum gate operations.

A major requirement for the use of trapped ions for quantum computation is the ability to cool the ions to the ground state of the trapping potential. This requires several stages of laser cooling. First, Doppler cooling on the $S_{1/2} - P_{1/2}$ dipole transition is applied so that the ions crystallize to strings with a temperature near the Doppler limit. Lower temperatures can be achieved with more refined cooling mechanisms such as sideband cooling on the $S_{1/2} - D_{5/2}$ transition. To determine the success of further cooling stages the ability to measure the ions' temperature is required. This measurement is done by recording the oscillation sidebands in absorption spectra of the $S_{1/2} - D_{5/2}$ transition.

The motion of a string of crystallized ions can be described by normal modes. These normal modes are selectively excited by applying radio-frequency fields near the resonance frequencies of these modes. By gating the CCD camera in phase with the radio-frequency excitation a movie is recorded of the center-of-mass mode and the next higher mode, the breathing mode.

With the realization of the trap, the laser systems at five different wavelengths, the preparation and control of a string of crystallized ions, and the ability of high resolution spectroscopy the basis is laid for further experiments involving the quantum features of the ion motion in the trap. With the preparation of a pure state of motion it will be possible to apply the ions to quantum gate operations, the building blocks for a quantum computer. This will allow for the deterministic entanglement of massive particles in so-called Bell and GHZ-states.

Zusammenfassung

Im Rahmen dieser Arbeit wurde ein neuer Meßplatz zur Speicherung und Kontrolle von Kalzium Ionenketten in Hinblick auf die Anwendung als Quantenrechner realisiert. Die Ionen werden in einer Paul-Falle gespeichert, mit Laserlicht gekühlt und angeregt und mit einem Photomultiplier und einer hochempfindlichen CCD Kamera beobachtet. Hochauflösende Spektroskopie auf dem schmalen $S_{1/2} - D_{5/2}$ Quadrupol-Übergang dient dazu, die Bewegung der Ionen in der Falle zu charakterisieren und die Möglichkeit zu testen, die $S_{1/2}$ und $D_{5/2}$ Niveaus als Quantenbit für die Anwendung von fundamentalen Quantengattern zu benutzen.

Die Fähigkeit, die Ionen in den Grundzustand des Fallenpotentials zu kühlen, ist eine notwendige Voraussetzung für die Anwendung der Ionen in einem Quantenrechner. Dieses verlangt mehrere Stufen der Laserkühlung. Zuerst wird Doppler-Kühlen auf dem $S_{1/2} - P_{1/2}$ Dipol-Übergang benutzt, damit die Ionen zu Ketten kristallisieren und eine Temperatur in der Nähe des Doppler-Kühlgrenze erreichen. Tiefere Temperaturen können nur mit komplizierteren Kühlverfahren erreicht werden wie zum Beispiel dem Seitenbandkühlen auf dem $S_{1/2} - D_{5/2}$ Übergang. Um den Erfolg von weiteren Kühlverfahren zu bestimmen, bedarf es der Fähigkeit, die Ionentemperatur auch bei tiefen Temperaturen zu messen. Dieses Messung wird mit Hilfe von Absorptionsspektren auf dem $S_{1/2} - D_{5/2}$ Übergang durchgeführt.

Die Bewegung einer Ionenkette wird durch Normalmoden beschrieben. Dieses Moden können selektiv angeregt werden mit Radiofrequenzfeldern in der Nähe der jeweiligen Resonanzfrequenzen. Es wurden Filme der Schwerpunktsbewegungsmode und der ersten höheren Mode aufgenommen.

Durch die Konstruktion der Falle, den Aufbau der Lasersysteme bei fünf unterschiedlichen Wellenlängen, die Präparation und Kontrolle von Ionenketten und die Fähigkeit zur hochauflösenden Spektroskopie wurde die Grundlage geschaffen zu weiteren Experimenten, welche die quantenmechanischen Eigenschaften der Schwingungsbewegung der Ionen in der Falle ausnutzen. Die Präparation eines reinen Bewegungszustandes wird es erlauben, Quantengatter zu implementieren. Des weiteren wird die Möglichkeit geschaffen, massive Teilchen in sogenannten Bell- und GHZ-Zuständen determiniert zu verschränken.

Contents

1	Introduction	1
2	Theory	5
2.1	Linear Paul trap	5
2.1.1	Trap function	5
2.1.2	Ion positions and modes of oscillation	9
2.2	Dark resonances	12
2.3	Laser cooling	13
2.4	Quantum computation with cold trapped ions	17
2.4.1	Introduction	17
2.4.2	Basic operations	18
2.4.3	The requirements for a physical system and the Cirac/Zoller scheme	19
2.4.4	Two-level system and the harmonic oscillator	21
2.4.5	Quantum logic with trapped ions: The CNOT gate	25
2.4.6	Bell states	27
3	Experimental Setup	29
3.1	Experimental setup: Ion trap apparatus	30
3.1.1	Vacuum vessel, trap electrodes, rf drive, fluorescence detection	30
3.2	Experimental setup: Lasers	37
3.2.1	Frequency doubled Ti:Sapphire laser for 397 nm	37
3.2.2	Ultra stable Ti:Sapphire laser for 729 nm	39
3.2.3	Diode lasers at 850, 854, and 866 nm	40
4	Ion Storage	45
4.1	Trap operation	45
4.1.1	Loading process	45
4.1.2	Linear, zigzag, and large ion crystals	48
4.1.3	Compensation of micromotion	49
4.2	Normal mode oscillation	54
4.2.1	Ion orbits	55
4.2.2	Normal mode excitation	56
5	Spectroscopy	61
5.1	Excitation spectra	62
5.1.1	Scans at 397 nm	64

5.1.2	Scans at 866 nm	65
5.1.3	Dark resonances	66
5.2	Absorption spectra on the quadrupole transition	69
5.2.1	Laser optimization	69
5.2.2	Pulsed spectroscopy	70
5.2.3	Zeeman components	72
5.2.4	Sideband spectrum	74
5.2.5	Carrier of the sideband spectrum	81
5.2.6	Line broadening	82
5.2.7	Coherent dynamics	83
5.2.8	Discussion	86
6	Summary and Outlook	89
7	Appendix	91
7.1	Ca ⁺ energy levels	91
7.2	Zeeman structure	92
7.2.1	Dipole transitions S _{1/2} - P _{1/2} and P _{1/2} - D _{3/2}	92
7.2.2	Quadrupole transition S _{1/2} - D _{5/2}	93
7.3	Possible qubit candidates	93
7.4	New trap design	96

1 Introduction

It has been shown [1] that ion traps can provide an ideal environment for isolated quantum systems such as a single, trapped, and laser-cooled atom. Ion storage has long been applied to ultra-high precision spectroscopy and the development of frequency standards. More recently, single trapped ions have been used to demonstrate and test some of the intriguing features of quantum mechanics [2, 3]. In particular, both the internal electronic state and the motional state of a trapped ion can be modified using laser light. Decoherence of internal and external states is nearly negligible even for very long interaction times. To explore these properties, several schemes have been proposed for the preparation of non-classical states of motion in a trap [4]. Their experimental realization [2] promises further improvement for the precision of spectroscopic measurements [5, 6]. With almost perfect control of the quantum state of a single ion, the attention has turned to systems of few ions with well-controlled interactions between them. Manipulations of their overall quantum state include the preparation of entangled states that have no classical counterpart. The possibility to entangle massive particles opens up many prospects for new experiments including measurements with Bell states and GHZ states [7] which would allow for new tests of quantum mechanics. Moreover, entanglement of particles will allow one to study quantum measurements such as the investigation of decoherence processes [3, 8, 9] in more detail.

I. Cirac and P. Zoller have recently proposed the application of linear ion traps and the collective quantum motion of a trapped string of ions to the realization of a quantum gate [10]. Quantum gates are the basic building blocks of a quantum computer. So far, practical quantum computers of any kind have not been realized, but it has been shown that they have the potential to implement radically new (quantum) algorithms which could solve problems that are intractable on a classical computer. The most striking algorithm so far deals with the factorization of large numbers into their prime factors [11]. Using the known classical algorithms, this problem grows exponentially with the length of the number to be factorized, but on a quantum computer it is reduced to a polynomial algorithm. The ability to factorize large numbers is interesting from the viewpoint of cryptography because most of the best codes rely on the fact that large numbers cannot be efficiently factorized. For this reason, the field of quantum computing in the last three years has experienced an explosive development with thousands of publications and many groups striving for an experimental realization. Apart from ion traps, other systems have been suggested for the use as a quantum computer. The most noteworthy involve molecules subject to nuclear magnetic resonance (NMR) [12, 13] and atoms coupled to a mode of light [14] or to a microwave field [15] in the context of cavity quantum-electrodynamics.

1 Introduction

In more detail, a quantum computer works with quantum registers made up of quantum bits (qubits) which can be manipulated analogously to classical bits using gate operations. In contrast to a classical bit given by the states 0 and 1, a qubit is represented by a two-level quantum system ($|0\rangle, |1\rangle$) which can be in a coherent superposition of both states. A gate on these qubits then preserves these coherences, being given by the unitary evolution according to some Hamiltonian which acts on the Hilbert space of qubits. It has been shown that the quantum mechanical analogue of a classical XOR-gate, the so-called controlled-NOT (CNOT) gate operation, is a realization of a universal quantum gate [16]. This means that any (quantum) logic operation on a quantum register can be constructed from this 2-qubit gate together with simple 1-qubit operations. In their proposal, Cirac and Zoller have been able to show that the CNOT gate can be realized using a linear string of ions cooled to the ground state of the trap and a series of laser pulses to address different ions. The realization of this gate operation based on a string of ions would therefore be of fundamental interest for the field of quantum computation. Furthermore, all basic algorithms could be tested using a string of trapped ions.

Quantum mechanical information is delicate and must be stored in systems which are essentially free of environmental perturbations. Any interaction with the environment, such as interactions in a solid, or, for the gaseous state, collisions with walls or atoms of a background gas have an effect similar to measurement processes in that they tend to alter or destroy the quantum mechanical information by inducing decoherence. Furthermore, the necessity to manipulate quantum states in order to implement algorithms requires that the quantum information has to be stored for times which are long enough to allow for coherent interaction of the ions with external fields. These requirements are all met by the ion storage technique, and for that reason stored ions have been proposed for the first experiments on quantum computation. In this spirit, the group of D. Wineland at NIST has used a single laser cooled ${}^9\text{Be}^+$ atom to demonstrate all the manipulations necessary for the implementation of a CNOT gate [17]. The single qubit quantum information (so-called target bit) was stored in two hyperfine ground states of Be^+ while the other qubit (so-called control bit) was encoded in the quantized vibration of the ion in the trap. The gate operation was realized with optical Raman transitions. Thus the potential of trapped ions for quantum bits has been clearly demonstrated. However, since in that experiment the control and the target bit were internal and external states of the same single ion, the scheme cannot be scaled up to realize a larger quantum register. Instead, several ions with controlled interaction between them will be required.

In that light, we have set out to realize the principles of quantum computation in a linear ion trap. The idea of using a linear trap for quantum computing is ingenious and simple: A qubit of the quantum computer is represented by two electronic levels of a trapped ion. The register consists of cold ions which line up along the longitudinal (symmetry) axis of the trap. The bus of the quantum computer, i. e. the (quantum) channel along which the qubits communicate with each other, is given by the combined oscillatory motion of the ions along this direction as a result of the inter-ion Coulomb repulsion. The state of the qubits is prepared using a laser beam focused onto the individual ions, and the gate operation is done by a series of laser pulses. Finally, the readout of the register at the end of the computation is done by measuring the state of all qubits.

The subject of this thesis is thus the construction of a linear ion trap and the preparation of ions for the use in quantum information processing. Calcium ions have been chosen to serve as carriers of the qubits because of the relatively easy availability of laser sources for the various transitions needed for laser cooling and state preparation. As a first candidate for a qubit transition the narrow quadrupole transition $S_{1/2} - D_{5/2}$ is used. The major requirement for using trapped ions for quantum computation is the ability to prepare the quantum bus in a pure quantum state. In practice this means that the ions need to be laser cooled to the ground state of the trap. For this, sideband cooling on the quadrupole transition will be used. The thesis reports on the setup of the vacuum vessel, the detection systems, and the laser systems. It is shown that trapped ions crystallize to strings, and that these strings can be laser cooled and stored for many hours. High resolution spectroscopy on the quadrupole transition is carried out to test its viability as a qubit transition. One of the goals of this spectroscopy is to measure the ions temperature so that the success of further laser cooling techniques such as sideband cooling can be tested.

The thesis is structured as follows: Chapter 1 is of theoretical nature. First, the function of a linear ion trap is explained together with the ions' modes of oscillation in the trap. In order to understand excitation spectra on trapped ions the appearance of dark resonances in these spectra is discussed. I will then consider laser cooling schemes which allow for ground state preparation. Finally, at the end of the theoretical chapter, I will discuss the requirements for quantum computation with strings of ions. This includes a review of the proposal by Cirac and Zoller [10].

The second chapter then describes the experimental setup. This includes the vacuum vessel, the trap electrodes, and the detection systems. A large part is devoted to the laser systems which are needed for laser cooling, spectroscopy, and for state measurements.

Experimental results concerning the storage and control of ions and the excitation of normal modes by radio-frequency fields are presented in chapter 3. The next chapter is the heart of this thesis. There, I will discuss the spectroscopic measurements, in particular the high resolution spectroscopy of the quadrupole transition in Ca^+ that will be used for sideband cooling and which is the first candidate for a qubit transition.

Finally, in the summary I will discuss the future prospects of the experiment and in particular the next immediate steps that need to be taken. All supplementary information which would otherwise interrupt the flow of this work can be found in the appendix.

2 Theory

This chapter will focus on the theoretical side of the ion trap quantum computer. The first two sections will review the function of the linear ion trap and the equations which govern the storage of individual particles and their motion in the trap potential. The next section will present the laser cooling techniques which are necessary to prepare the ions in the ground state of the trapping potential. In the case of our trap we expect to need at least two stages of cooling in order to reach this lowest temperature. Then the concept of a quantum computer will briefly be reviewed in order to explain the requirements which need to be fulfilled for ion trap quantum computing. Then, because the ion trap quantum computer consists of ions as two-level systems coupled to a mode of oscillation, the Hamiltonian describing such a system will be discussed. In our experiment, the two-level system is given by two Zeeman sublevels of the $S_{1/2}$ and $D_{5/2}$ states, and it is driven by a laser on the $S_{1/2}$ to $D_{5/2}$ quadrupole transition. Hence, the interaction of a two-level system with a mode of oscillation in the presence of laser light is discussed. Then, the basic mechanisms needed for quantum computation are presented. As examples, I will consider the CNOT gate as the fundamental building block of a quantum algorithm and how Bell states of the quantum register can be prepared.

2.1 Linear Paul trap

In this section the parameters needed to understand the trapping of particles in a linear Paul trap are discussed. A general overview of the physics of stored ions in Paul and Penning traps can be found in [19]. For a further discussion of linear traps, in particular regarding the application of linear traps to improved frequency standards, the reader is referred to the earlier work on linear traps ([20]-[27]).

2.1.1 Trap function

A schematic drawing of a linear Paul trap is shown in Fig. 3.4. Four elongated electrodes generate a two-dimensional quadrupole field, and two ring electrodes serve for axial ion confinement. The configuration without the ring electrodes is identical to the quadrupole mass spectrometer invented by W. Paul and co-workers [28]. For the quadrupole field a radio-frequency voltage $U(t) = U_0 + V_0 \cos(\Omega t)$ is applied to two of the four elongated electrodes (connected diagonally), the other two are held at ground potential. The resulting potential near the trap axis is of the form

$$\phi(x, y, t) = \frac{x^2 \leftrightarrow y^2}{2R^2}(U_0 + V_0 \cos(\Omega t)).$$

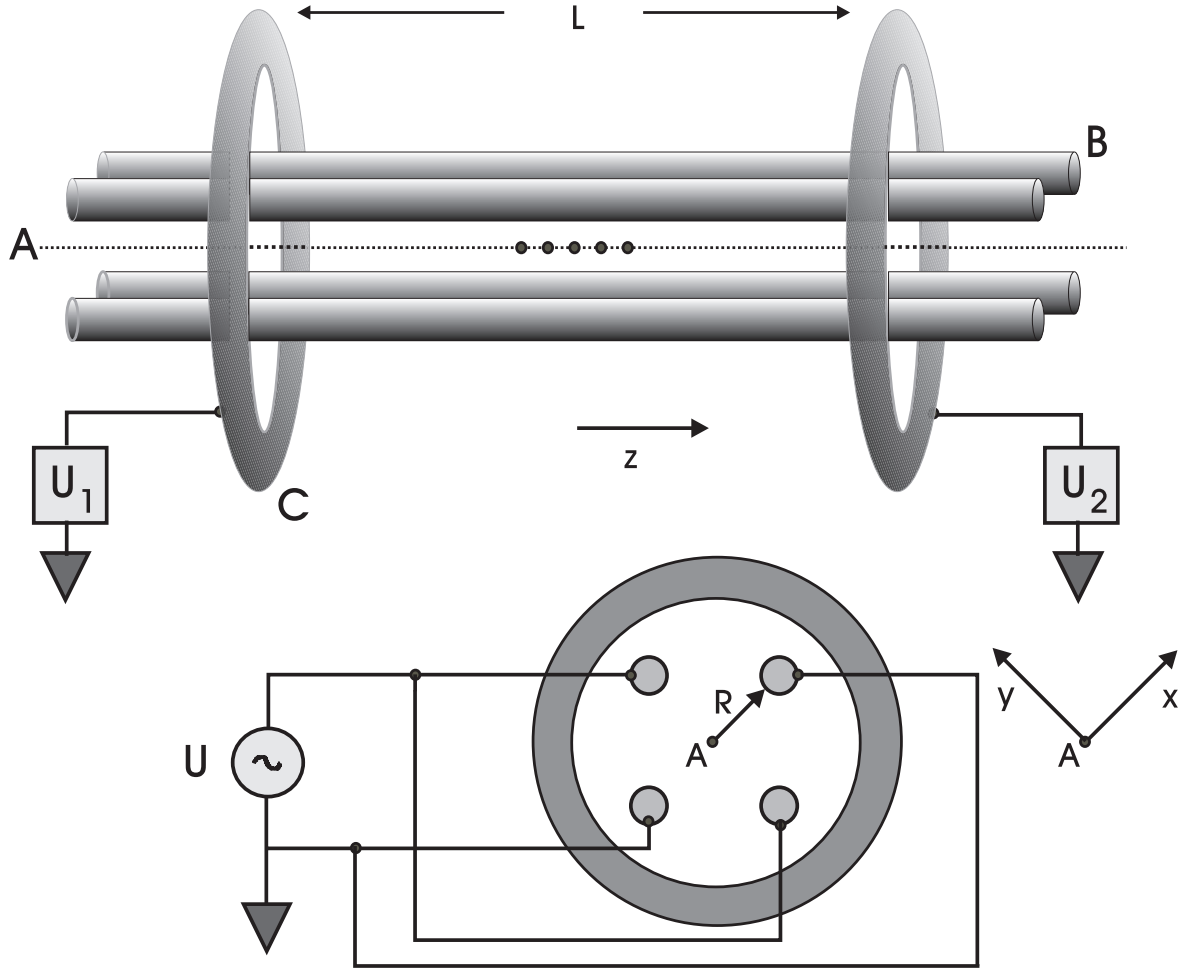


Figure 2.1: Electrode configuration for the linear trap. A: Trap axis. In the center of the trap the inter-ion spacing is exaggerated. B: Quadrupole electrodes. C: Ring electrode. R: Distance from trap center to quadrupole electrodes. Voltages at dc (U_1 and U_2) are applied to the ring electrodes. The radio-frequency voltage U is applied to two diagonally connected quadrupole electrodes, the other two are grounded.

The equations of motion for a single ion of mass M and charge Q in the x - y -plane are then given by

$$\ddot{x} = \Leftrightarrow \frac{Q}{MR^2} (U_0 + V_0 \cos(\Omega t)) x \quad \text{and} \quad \ddot{y} = \frac{Q}{MR^2} (U_0 + V_0 \cos(\Omega t)) y.$$

With the substitution

$$a_x = \Leftrightarrow a_y = \frac{4QU_0}{M\Omega^2 R^2} \quad \text{and} \quad q_x = \Leftrightarrow q_y = \frac{2QV_0}{M\Omega^2 R^2}.$$

the equations take the form of the Mathieu equation

$$\ddot{x} + (a_x + 2q_x \cos(\Omega t)) \frac{\Omega^2}{4} x = 0 \quad \text{and} \quad \ddot{y} + (a_y + 2q_y \cos(\Omega t)) \frac{\Omega^2}{4} y = 0. \quad (2.1)$$

For the practical case that $|a_x|, |a_y| \ll 1$ and $|q_x|, |q_y| \ll 1$ stable solutions to these equations exist. Their approximate form is ([19], [29])

$$x(t) = x_0 \cos(\omega_x t + \phi_x) \left(1 + \frac{q_x}{2} \cos(\Omega t)\right) \quad \text{and} \quad y(t) = y_0 \cos(\omega_y t + \phi_y) \left(1 + \frac{q_y}{2} \cos(\Omega t)\right),$$

where x_0, y_0, ϕ_x , and ϕ_y are determined by initial conditions, and where

$$\omega_x = \frac{\Omega}{2} \sqrt{\frac{q_x^2}{2} + a_x} \quad \text{and} \quad \omega_y = \frac{\Omega}{2} \sqrt{\frac{q_y^2}{2} + a_y}. \quad (2.2)$$

Hence, the motion of a single ion in the x-y-plane is harmonic with frequencies ω_x and ω_y , and the amplitude is modulated at the drive frequency Ω . The ion's harmonic oscillation is called 'secular motion', whereas the small contribution oscillating with Ω is termed 'micromotion'. Neglecting this contribution, the ion's motion in the x-y-plane of the trap is equivalent to the motion in a harmonic pseudo-potential ψ of the form

$$\psi = \frac{M}{2} (\omega_x^2 x^2 + \omega_y^2 y^2).$$

The depth of the pseudo-potential well in the two directions is then given by

$$\psi_x = \frac{M}{2} \omega_x^2 R^2 = \frac{Q^2 V_0^2}{4m\Omega^2 R^2} + \frac{QU_0}{2} \quad \text{and} \quad \psi_y = \frac{M}{2} \omega_y^2 R^2 = \frac{Q^2 V_0^2}{4m\Omega^2 R^2} \Leftrightarrow \frac{QU_0}{2}.$$

In our trap, $U_0 = 0$ and hence $a_x = \Leftrightarrow a_y = 0$ so that the oscillation frequencies in x and y direction are degenerate. Typical operating parameters for this trap are $V = 800$ V, $\Omega = 18$ MHz, $R = 1.2$ mm, so that we achieve oscillation frequencies of $\omega_x/2\pi = \omega_y/2\pi = 1.4$ MHz, a well depth of about 20 eV, and a q-parameter of $q = q_x = \Leftrightarrow q_y = 0.2$.

In order to confine particles in all three dimensions it is necessary to 'close up' the quadrupole trap in the axial (z) direction. This is achieved by applying static potentials U_1 and U_2 to the ring electrodes on each side of the trap center (see Fig. 2.1). Ideally, the static potentials on the ring electrodes should be equal: $U_1 = U_2 = U_{12}$. Numerical calculations show that the potential near the trap center is harmonic and can be approximated by the ansatz¹

$$\frac{1}{2} M \omega_z^2 z_0^2 = \kappa Q U_{12}.$$

Here, $z_0 = L/2$ is the distance from trap center to the ring electrodes, ω_z is the axial oscillation frequency, and κ is a geometric factor ($\kappa \simeq 0.025$) which describes how much of the static

¹The pseudo-potential well in the radial direction is slightly weakened by the addition of the static potential ([25]). The radial frequencies change according to $\omega_{x,y} \mapsto \omega'_{x,y} = \sqrt{\omega_{x,y}^2 - \frac{1}{2}\omega_z^2}$. For the parameters in our trap this change is less than 0.5%.

field from the ring electrodes is present along the trap axis. Typical parameters for our trap are $\omega_z/2\pi = 110$ kHz for $U_{12} = 100$ V. The well depth along this direction is then $\phi_z = \frac{M}{2}\omega_z^2 z_0^2 = 2.5$ eV.

Fig. 2.2 shows the resulting anisotropic harmonic pseudo-potential

$$\psi = \frac{M}{2}(\omega_x^2 x^2 + \omega_y^2 y^2 + \omega_z^2 z^2)$$

for typical oscillation frequencies in our trap ($\omega_x \simeq \omega_y = 1.4$ MHz, $\omega_z = 150$ kHz).

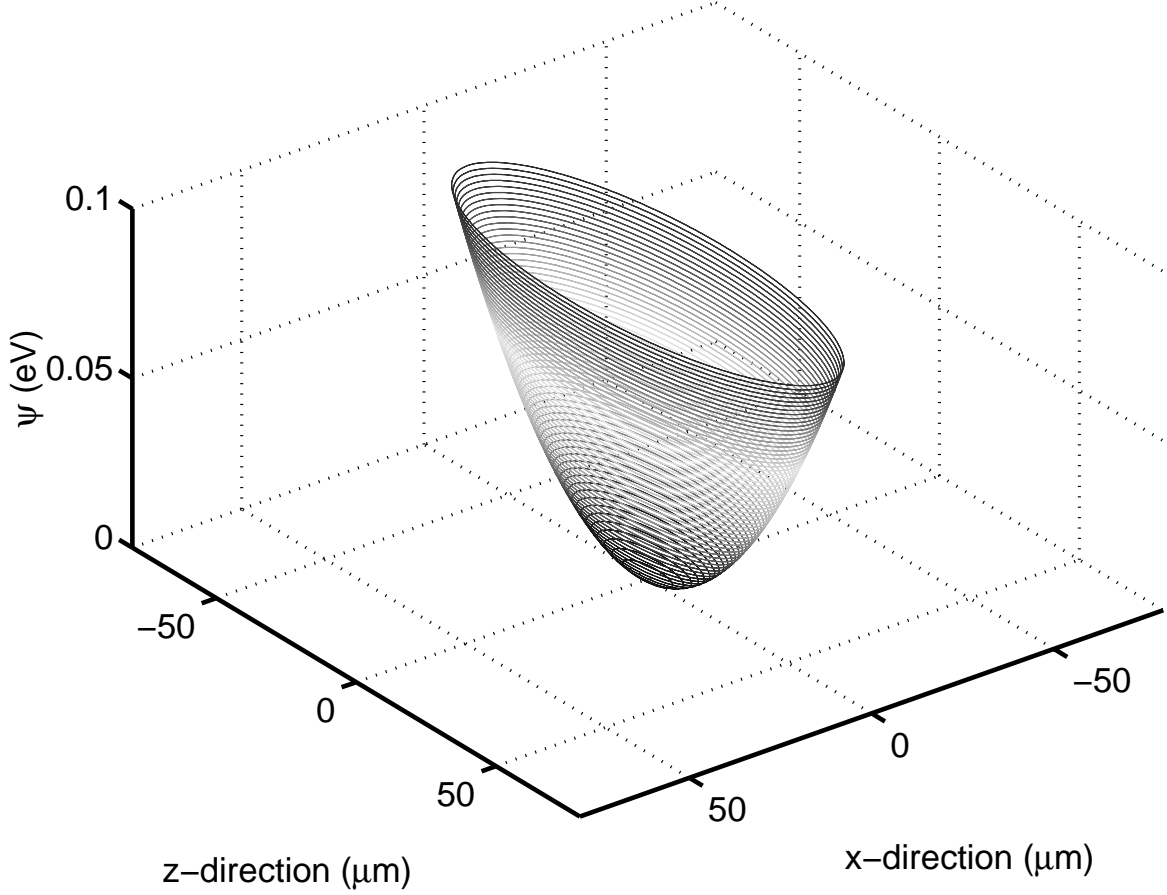


Figure 2.2: Schematic illustration of the anisotropic harmonic pseudo-potential ψ for typical trapping frequencies ($y=0$): $\omega_x \simeq \omega_y = 1.4$ MHz, $\omega_z = 150$ kHz.

In practice, a trapped ion is subject to additional static fields. These fields are, for example, caused by charged surfaces nearby or by electrode imperfections. Ring electrodes which are not perfectly circular or whose axis of symmetry does not agree with the trap axis result in dc electric field components along the x- and y-direction. In the presence of such additional

electric field components² E_x and E_y the Mathieu equations (2.1) become

$$\ddot{x} + (a_x + 2q_x \cos(\Omega t)) \frac{\Omega^2}{4} x = \frac{QE_x}{m} \quad \text{and} \quad \ddot{y} + (a_y + 2q_y \cos(\Omega t)) \frac{\Omega^2}{4} y = \frac{QE_y}{m}. \quad (2.3)$$

The approximate solution is then ([29])

$$\begin{aligned} x(t) &= (x_1 + x_0 \cos(\omega_x t + \phi_x)) \left(1 + \frac{q_x}{2} \cos(\Omega t)\right), \\ y(t) &= (y_1 + y_0 \cos(\omega_y t + \phi_y)) \left(1 + \frac{q_y}{2} \cos(\Omega t)\right), \end{aligned} \quad (2.4)$$

where

$$x_1 = \frac{QE_x}{m\omega_x^2} \quad \text{and} \quad y_1 = \frac{QE_y}{m\omega_y^2}. \quad (2.5)$$

The static electric field thus displaces the ion from the trap center by x_1 and y_1 and causes extra micromotion with amplitude $\frac{x_1 q_x}{2}$ along the x-direction and $\frac{y_1 q_y}{2}$ along the y-direction.

At this point, before proceeding, I would like to briefly point out the difference between conventional Paul traps and linear ion traps. In contrast to conventional Paul traps the linear ion trap combines dynamical and static potentials for trapping. It has the advantage that linear quadrupole electrodes provide a radio-frequency driving field which generates a two-dimensional trapping (pseudo) potential whose minimum is not just a single point in space but essentially a line along the symmetry axis. Consequently, more than one ion can be stored in this trap without the problem that one or more of the ions are not located at the minimum of the pseudo potential. This problem is severe because ions which are not precisely located at this minimum experience additional micromotion as shown above and hence acquire additional energy. In particular, ions which experience excess micromotion cannot be cooled to very low temperatures, a necessary ingredient of the ion trap quantum computer as we will see shortly.

2.1.2 Ion positions and modes of oscillation

The equilibrium positions for N ions in the linear trap are given by the minima of the potential energy

$$V = \sum_{j=1}^N \frac{M}{2} \omega_z^2 z_j^2 + \sum_{i,j=1, i \neq j}^N \frac{Q^2}{8\pi\epsilon_0} \frac{1}{|z_j \leftrightarrow z_i|}. \quad (2.6)$$

Here, we assume that the ions are strongly bound in the radial (x,y) directions, and only weakly bound in the axial (z) direction. This results in a one-dimensional geometry. Also, we assume that the ions move in a harmonic potential along the z axis as discussed in the last section and that the only additional forces they are subjected to are the Coulomb repulsion

²It is assumed that components along the z-direction are included in the static field caused by the ring electrodes and thus need not to be considered separately.

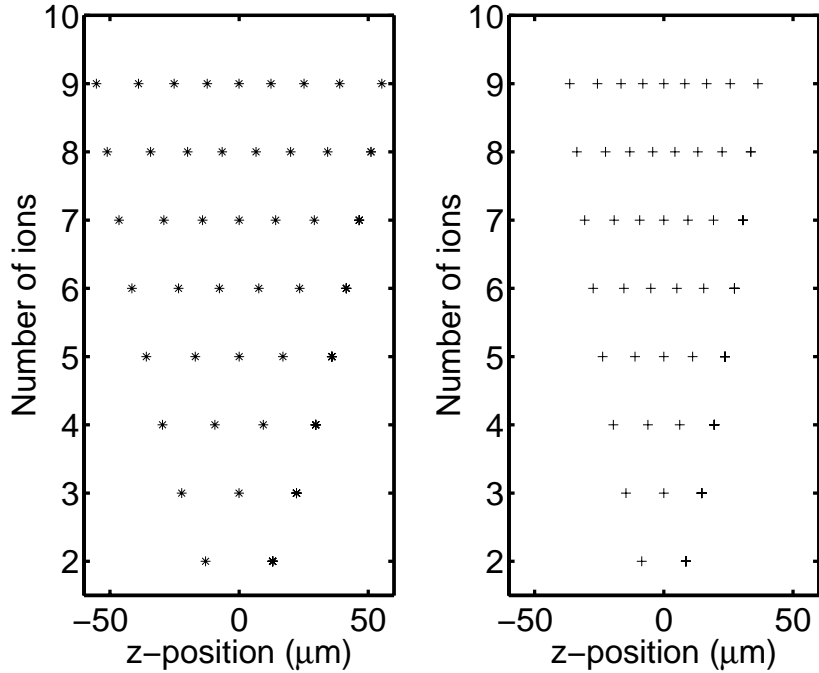


Figure 2.3: Positions of up to 9 Ca^+ ions in the linear trap for trap frequencies $\nu_z = 100$ kHz (left) and $\nu_z = 200$ kHz (right).

forces. The assumption of one-dimensionality is only true if the ratio of the radial oscillation frequency ν_r to the axial oscillation frequency ν_z exceeds the critical ratio given by [30]

$$\frac{\nu_r}{\nu_z} \simeq 0.73 N^{0.86}. \quad (2.7)$$

As an example, for $N = 10$ ions and $\nu_r = 1.4$ MHz the axial frequency ν_z needs to be smaller than 265 kHz. Fig. 2.3 shows the equilibrium positions for up to 9 ions according to Eq. 2.6 for $\nu_z = 100$ and 200 kHz. The spacing between the ions in a linear string is not uniform. The length scale of the ion spacing is given by $d = (Q^2 / (4\pi\epsilon_0 M \omega_z^2))^{1/3}$ [31], and the separation for two ions is then $d^{(2)} = 2^{1/3} d$. A plot of this separation is shown in Fig. 2.4. For Ca^+ ions the separation is approx. $26 \mu\text{m}$ for $\nu_z = 100$ kHz and $16 \mu\text{m}$ for $\nu_z = 200$ kHz. These distances are important if one wants to address individual ions in the string with a focused laser beam.

Small oscillations of the ions around their equilibrium positions are described by $3N$ normal modes. In what follows, we are mainly interested in the N normal modes along the axial direction. Following [31], the position of the i -th ion is approximated by

$$z_i(t) = z_i^{(0)} + q_i(t).$$

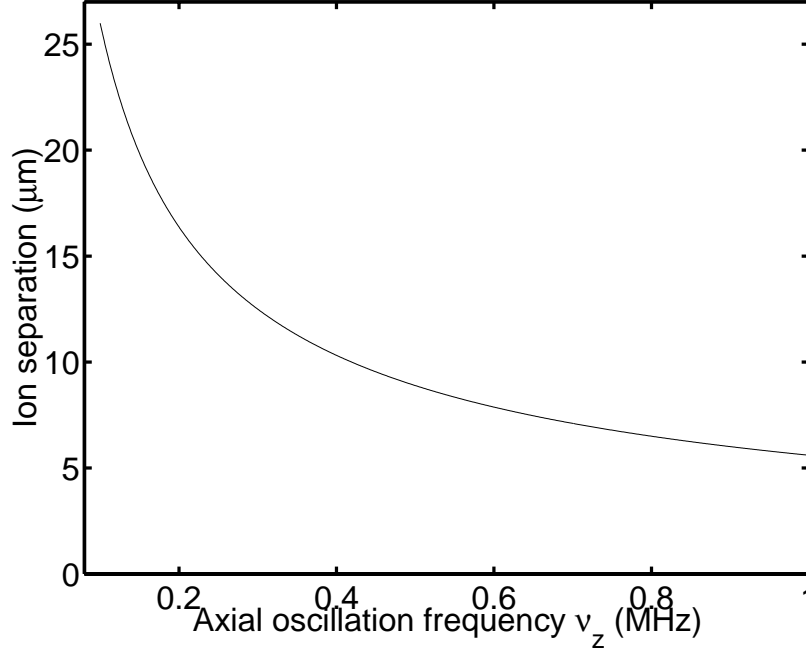


Figure 2.4: Separation of two ions as a function of the axial oscillation frequency ν_z .

The Lagrangian for the motion is then

$$L = \frac{M}{2} \sum_{j=1}^N (\dot{q}_j)^2 \Leftrightarrow \frac{1}{2} \sum_{i,j=1}^N q_i q_j \left[\frac{\partial^2 V}{\partial z_i \partial z_j} \right]_0,$$

where the double partial derivatives are evaluated at the equilibrium position. The normal modes Q_p of oscillation are then given by the N (normalized) eigenvectors $\mathbf{b}^{(p)}$, $p = 1, \dots, N$, of the matrix

$$A_{ij} = \left[\frac{\partial^2 V}{\partial z_i \partial z_j} \right]_0 \quad i, j = 1, \dots, N,$$

through the relation

$$Q_p(t) = \sum_{j=1}^N \mathbf{b}_j^{(p)} q_j(t),$$

and the frequencies corresponding to these normal modes are given by

$$\nu_p = \sqrt{\mu_p} \nu_z,$$

where the μ_p are the eigenvalues of matrix A . For $p = 1$ and $p = 2$ these can be given as $\mu_1 = 1$ and $\mu_2 = 3$, for higher p they need to be determined numerically. Remarkably, these

higher eigenvalues are nearly independent of the number of ions N . For up to 9 ions, they are given by [31] $\mu_3 = 5.82(2)$, $\mu_4 = 9.35(6)$, $\mu_5 = 13.54(7)$, $\mu_6 = 18.34(7)$, $\mu_7 = 23.72(7)$, $\mu_8 = 29.67(4)$, and $\mu_9 = 36.16$. The indicated error is the deviation given by varying N up to 9 ions.

In this work we will mostly concentrate on $p = 1$, the center-of-mass mode, where all ions oscillate back and forth in phase with the same amplitude, and on $p = 2$, the breathing mode, where the ions on one side of the trap center move 180° degrees out of phase with the ones on the other side of the center. In particular, for an odd number of ions, the center ion does not move.

2.2 Dark resonances

Even though $^{40}\text{Ca}^+$ has no nuclear spin and hence no hyperfine structure, it has a very diverse level scheme. A discussion of $^{40}\text{Ca}^+$ and its various transitions can be found in the appendix. A level scheme is shown in Fig. 7.1. To some extent this diversity is not needed for our experiments on quantum computation. In fact, the richness of the level scheme introduces additional difficulties, some of which are related to the two 3D levels which lie below the 4P levels. An obvious complication is the necessity to have a repumper laser at 866 nm to prevent pumping into the metastable $D_{3/2}$ level. Even for simple experiments such as ion storage and Doppler cooling we always have to take into account that we are dealing with a 3-level system in Λ configuration (not counting Zeeman sublevels), and, in reality, an 8-level system when counting Zeeman sublevels (see Fig. 7.2). This kind of system in many aspects shows a completely different behavior than an ideal two-level system.

One of the most prominent effects associated with a 3-level Λ system (where an upper level is coupled via dipole transitions to two lower lying ground or metastable levels, see (A) in Fig. 2.5) is the occurrence of Raman or so-called dark resonances [32, 33] (see Fig. 2.6). In this system it is possible that the lasers on the dipole transitions create a coherent superposition of the two lower levels when the Raman condition for the lasers is fulfilled, i. e. when the detuning of both lasers from the transition frequencies is equal (see (B) in Fig. 2.5). In this case, because the upper level is not involved, no fluorescence is scattered from the ion i. e. the excitation spectrum shows a 'dark' resonance for this detuning. The precise shape, width, and depth of the dark resonance is given by laser power and laser linewidth. Multiple dark resonances can be seen in Fig. 5.6, where experimental data are shown together with a fit. Here, the situation is a bit more involved than in the 3 level case because, as mentioned above, 8 levels are involved which allow for 12 possible dark resonances depending on the choice of magnetic field and polarization³. For the fit the 8-level Bloch equations describing the system a zero temperature have been used. A detailed discussion of the 3- and the 8-level system involving dark resonances (for $^{138}\text{Ba}^+$) can be found in [33].

Dark resonances allow for a resolution which is not limited by the natural linewidth of the transitions. They therefore allow for the possibility to deduce information about laser perfor-

³4 of the 12 possible dark resonances are degenerate, so a maximum of 8 dark resonances can be observed

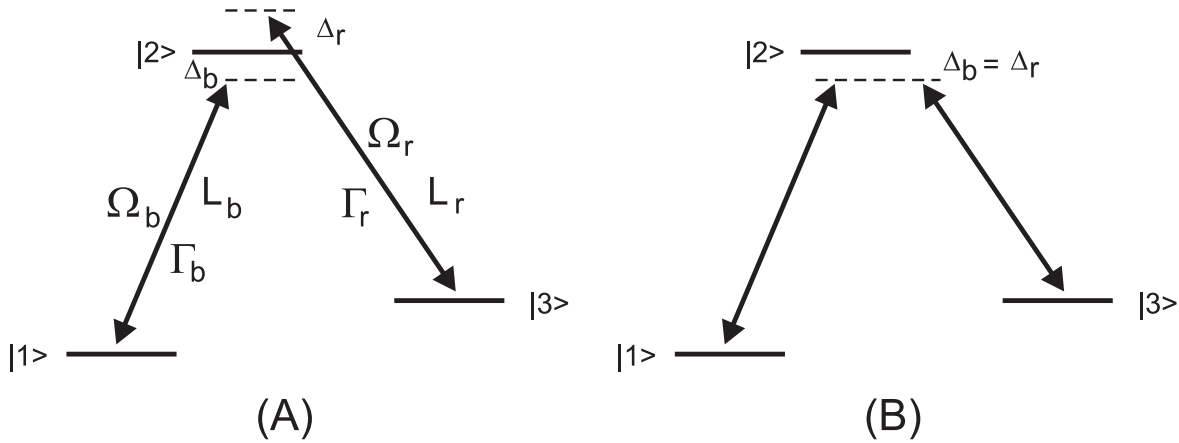


Figure 2.5: (A) Three-level system in Λ configuration. The upper level ($|2\rangle$) is coupled to two lower (ground) levels ($|1\rangle$, $|3\rangle$) via dipole transitions. These transitions are driven by lasers b (blue) and r (red). The relevant parameters are the decay rates (Γ), the Rabi frequencies (Ω), laser linewidths (L), and detunings (Δ). For $^{40}\text{Ca}^+$, transition b corresponds to the $S_{1/2} - P_{1/2}$ transition at 397 nm, and transition r corresponds to the $D_{3/2} - P_{1/2}$ transition at 866 nm. (B) Raman condition for dark resonance: ($\Delta_b = \Delta_r$).

mance (at 397 and 866 nm) from a fit to the data. It is important to note that our fit does not include a non-zero temperature for the ions. The ions' oscillatory motion should in fact produce oscillation sidebands to the dark resonance, which, if not resolved by small linewidth lasers, should broaden the dark resonance. At a minimum we are able to get an upper bound for laser linewidth and saturation parameter. Also, the positions of the dark resonances for the 8 level system provide information about laser detuning and magnetic field strength.

2.3 Laser cooling

As we shall see in the next section, at the outset for any quantum mechanical computation according to the proposal of I. Cirac and P. Zoller [10] the ions need to be prepared in a well defined pure state. This is not difficult for the internal electronic degrees of freedom where standard optical pumping can be applied to prepare a specified state. A more serious problem is posed by the external (motional) degrees of freedom. Preparation of the ions in a pure state of motion requires cooling to the quantum regime. This can be achieved by using laser cooling [1] to optically pump the ions into the lowest state of the quantized harmonic trapping potential.

Laser cooling of single atomic particles has been applied routinely for almost two decades. Proposed by T. Hänsch and A. Schawlow [34] and by D. Wineland and H. Dehmelt [35] in 1975, laser cooling was first observed by Neuhauser et al. [36] on Ba^+ ions by and Wineland et al. [37] on Mg^+ ions in 1978. For a bound two-level system, such as an ion in a Paul

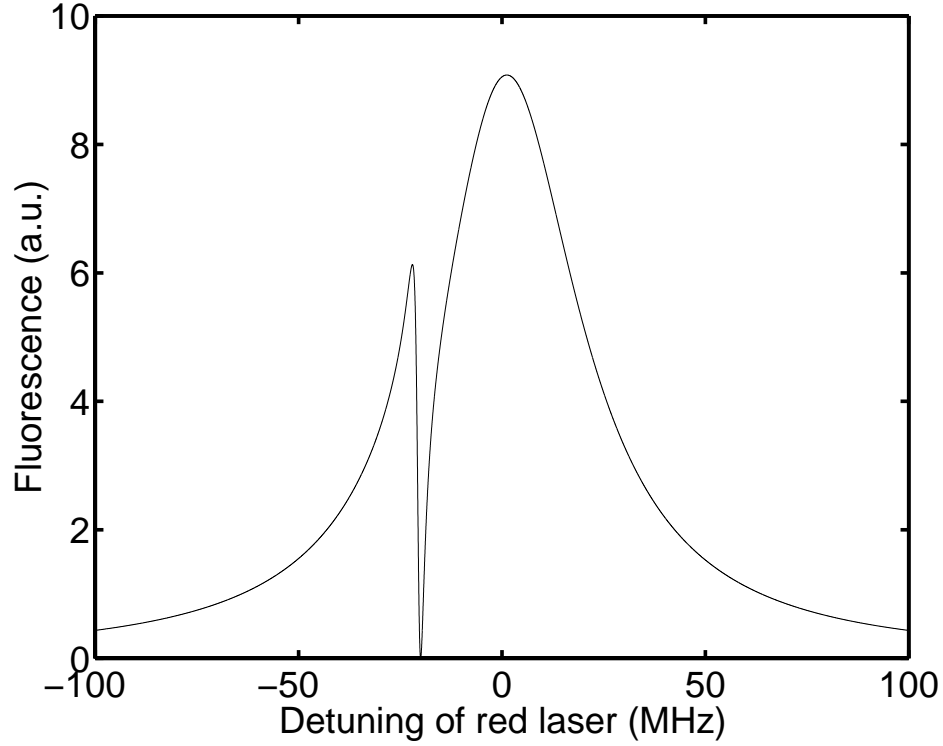


Figure 2.6: Dark resonance for three-level system. Parameters: $\Gamma_b = 20$ MHz, $\Gamma_r = 1.5$ MHz, $\Omega_b = 10$ MHz, $\Omega_r = 2.25$ MHz, $L_b = L_r = 0$ MHz. The blue laser is red detuned by 20 MHz. The parameters are explained in Fig. 2.5).

trap, two limiting cases are of interest. If the trap frequency ν is much smaller than the natural linewidth Γ of the optical transition used for laser cooling ($\nu \ll \Gamma$), the final temperature is limited by $T = \hbar\Gamma/2k_B$, where k_B is Boltzmann's constant. This regime is called the weak-binding regime, the limit is called the Doppler limit, and the laser cooling in this regime is called Doppler cooling. On the other hand, for trap frequencies $\nu \gg \Gamma$ (the strong binding regime), the trapped particle develops well-resolved absorption sidebands at the trap frequency and can be optically pumped to the lowest vibrational state by exciting selectively the lower sideband (sideband cooling). In this case the trapping potential has to be treated quantum mechanically. In general, a harmonic oscillator potential is assumed. The particle's temperature can be very low and is given by the probability of not being in the lowest state of the quantum mechanical oscillator. Sideband cooling is only effective if the particle is confined to a region in space which is much smaller than the wavelength of the laser light used for cooling. More precisely, this condition is expressed as $(k^2 \langle z^2 \rangle)^{1/2} = kz_0 < 2n_z + 1 \rangle^{1/2} \ll 1$ and is called the Lamb-Dicke regime [40]. In this formula $k = 2\pi/\lambda$ is the wavenumber and $z_0 = (\hbar/2m\omega_z)^{1/2}$ is the spread of the zero-point wavefunction along the z -direction in the trap. $\eta = kz_0$ is called the Lamb-Dicke parameter.

In our experiment we expect to need two or three stages of laser cooling to reach the desired ground state in the trap. In the following I will discuss the cooling schemes that we use or plan to use to reach this ground state. Doppler cooling (on a dipole transition) is routinely applied by all groups who store single ions. Doppler cooling on a quadrupole transition has, to my knowledge, not been realized yet. Sideband cooling with single ions, on the other hand, has been achieved on quadrupole [38] and on Raman [39] transitions. In the group of D. Wineland, the ground state in a trap for a single Hg^+ ion was reached for more than 95% in two dimensions. For a single Be^+ ion the ground state was reached for more than 92% in three dimensions.

Doppler cooling on the dipole $S_{1/2}$ to $P_{1/2}$ transition: The first stage that we routinely apply to stored ions is Doppler cooling, where the ions are cooled on a dipole transition which scatters a lot of light (and thus initially yields a high cooling rate) but which limits the ions' temperature to the Doppler temperature. This temperature is essentially given by the uncertainty in energy of the respective transition ($E_{min} = \hbar\Gamma_{SP}/2$, where Γ_{SP} is the natural linewidth). For trapped ions, this translates into a minimum average quantum number in the axial direction [40]:

$$\langle n_z \rangle_{min} = \frac{1}{2} \left(\frac{\Gamma_{SP}}{\omega_z} \Leftrightarrow 1 \right).$$

For the current parameters in our trap we have $\langle n_z \rangle_{min}$ on the order of 100 when Doppler cooling on the $S_{1/2}$ - $P_{1/2}$ dipole transition is applied. This temperature is most likely still too high to directly continue with sideband cooling on the $S_{1/2}$ - $D_{5/2}$ quadrupole transition. In particular, the Lamb-Dicke regime is not reached. Hence, an intermediate stage is needed. One possibility for an intermediate stage is to apply Doppler cooling on the quadrupole transition.

Doppler cooling on the quadrupole $S_{1/2}$ to $D_{5/2}$ transition: As with sideband cooling on this transition (see below), it is necessary to 'quench' the upper $D_{5/2}$ level by applying laser light at 854 nm to the $D_{5/2}$ - $P_{3/2}$ transition (see Fig. 2.7). The purpose of this laser is to broaden this level to the extent that Doppler cooling with a reasonable cooling rate is possible. In contrast to Doppler cooling on the dipole $S_{1/2}$ to $P_{1/2}$ transition, where the natural linewidth is so broad that we do not resolve the Zeeman components, we will select one of the Zeeman lines for cooling, preferably $S_{1/2}(m_J = 1/2)$ to $D_{5/2}(m_J = 5/2)$ component. The cooling limit is then essentially the same formula as above, the only difference being that Γ_{SP} is replaced by Γ'_{SD} which is the effective linewidth given in the presence of the quenching laser:

$$\langle n_z \rangle = \frac{1}{2} \left(\frac{\Gamma'_{SD}}{\omega_z} \Leftrightarrow 1 \right).$$

For low saturation parameter on the $D_{5/2}$ - $P_{3/2}$ transition an analytical expression can be given for this effective linewidth [41]

$$\Gamma'_{SD} = \frac{(\Omega_{DP}/2)^2}{((\Gamma_{SP} + \Gamma_{DP})/2)^2 + \Delta_{DP}^2} \Gamma_{SP}. \quad (2.8)$$

According to this formula it should be possible to design a linewidth on the order of a few hundred kHz by appropriately choosing laser power (given by the Rabi frequency Ω_{DP}) and detuning (given by Δ_{DP}) on the quenching transition. Γ_{SP} and Γ_{DP} denote the linewidths of the $S_{1/2} - P_{3/2}$ and on the $D_{5/2} - P_{3/2}$ transitions, respectively. With this linewidth, we expect to achieve $\langle n_z \rangle \simeq 10$ with cooling times on the order of a few ms.

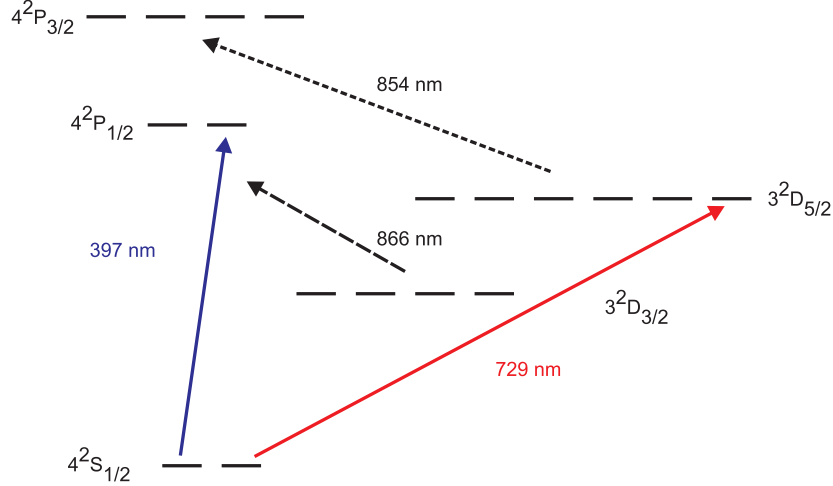


Figure 2.7: The relevant transitions in Ca^+ for Doppler and sideband cooling on the qubit transition at 729 nm. The laser at 729 nm is tuned to the $S_{1/2}(m_J = 1/2) - D_{5/2}(m_J = 5/2)$ Zeeman component, the laser at 854 nm serves for quenching and repumping, the laser at 866 nm is solely a repumper, and the laser at 397 nm recycles the ion if optical pumping into the $S_{1/2}(m_J = \pm 1/2)$ state has occurred.

Sideband cooling on the quadrupole $S_{1/2}$ to $D_{5/2}$ transition: Sideband cooling is possible when the (effective) linewidth of the cooling transition is much smaller than the frequency of oscillation in the trap and when the Lamb-Dicke criterion is fulfilled. For the quadrupole transition the first requirement means that $\Gamma'_{SD} \ll \omega_z$. By modifying the power and the detuning of the quenching laser one can continuously tune from the Doppler regime to the sideband regime [41]. In the sideband regime with the Lamb-Dicke criterion fulfilled, the minimum oscillation quantum number is given by [40]

$$\langle n_z \rangle = C \left(\frac{\Gamma'_{SD}}{\omega_z} \right)^2.$$

C is a constant of the order of 1 depending on the atomic transition. Outside the Lamb-Dicke regime sideband cooling does not lead to such low temperatures because the possibility of spontaneous transitions which change the oscillation quantum number is greatly increased. In general, this results in a higher diffusion constant and hence in higher final temperatures. Sideband cooling outside the Lamb-Dicke regime seems only possible with more elaborate cooling sequences [42]. For sideband cooling in the Lamb-Dicke regime, further improvements

can be expected by placing the ions at the node of a standing wave laser when heating due to off resonant transitions is not present [41].

Finally, some difficulties associated with ground state laser cooling of a trapped string of Ca^+ ions should be mentioned. First, it is important to note that a collection of N ions with $3N$ normal modes needs to be cooled. In principle, cooling one of the modes should be equivalent to cooling a single ion, so one would have to cycle through all $3N$ modes repeatedly (since the recoil will heat all modes). Hopefully, it will only be necessary to cool the N modes along the axial direction in the trap, and possibly it might suffice just to cool the mode which is used as the quantum bus for quantum computation (details below).

A second difficulty is associated with the fact that the quadrupole transition in Ca^+ does not provide a simple two or three level system. This can be seen in Fig. 2.7. For example, from the $P_{3/2}(m_J = 3/2)$ state there is decay not only to the ground state $S_{1/2}(m_J = 1/2)$, from which the cooling cycle starts again, but also decay back to the $D_{5/2}$ and to the $D_{3/2}$ levels. The decay to some Zeeman component of the $D_{3/2}$ level requires that the repumping laser at 866 nm needs to depopulate this level with the possibility that the ion ends up in the $S_{1/2}(m_J = \pm 1/2)$ state. Therefore, an additional pumping laser is required to occasionally recycle the electron to the $S_{1/2}(m_J = 1/2)$ state, for example a σ^+ laser at 397 nm (a laser at this wavelength would have to be chopped on only briefly during cooling in order not to perturb the qubit transition). Luckily, the favorable branching ratio of the $P_{3/2}$ state greatly reduces these unwanted transitions which add to additional diffusion in n -space.

A third difficulty is the power available at 729 nm to drive the qubit transition for either Doppler or sideband cooling. The scattering rate on this transition will ultimately determine the cooling rate and hence the final temperature if external heating processes are present. Currently, we expect a Rabi frequency on the order of 10 kHz. Starting from $\langle n_z \rangle \simeq 100$, we expect that cooling will take a time on the order of about 1 ms. For the present time, this is acceptable, but this time certainly limits the maximum possible rate at which the experiment can be carried out.

2.4 Quantum computation with cold trapped ions

2.4.1 Introduction

Quantum computation has its origins in the early 1980s when R. Feynman pointed out that the computational effort to simulate a quantum system on a digital computer seems to increase exponentially with the number of degrees of freedom of this system [43]. He thus suggested that a quantum computer, i. e. a quantum system whose evolution is interpreted as computation, might be better suited to this task. D. Deutsch subsequently realized that the counterpart of a classical computation, carried out on a quantum computer, could lead to an exponential speed-up of the calculation [44]. The first quantum algorithm of practical interest was then found by P. Shor [11]. His algorithm, implemented on a quantum computer,

allows one to factor a large number L into its prime factors in polynomial time⁴. The important point is that there is no known classical counterpart to this algorithm. This result is of great relevance in cryptography because all standard encryption systems rely on the fact that factorization of large numbers is exponentially difficult.

A good introduction to quantum computing can be found in [45] and [46]. For our purposes, a very basic realization of a quantum computer consists of a set of N quantum mechanical two-level systems (or, equivalently, spin $1/2$ systems), also called qubits, which strongly interact with each other via some quantum bus and whose interaction with the outside world can be switched on and off to allow for state preparation, state manipulation, and state measurement. This set of N qubits, each denoted by the set $\{|0\rangle, |1\rangle\}$ or, alternatively, $\{|\downarrow\rangle, |\uparrow\rangle\}$, shall be called the quantum register⁵. The 2^N -dimensional state space of this register is thus spanned by the vectors $\{|000\dots 0\rangle, |100\dots 0\rangle, |010\dots 0\rangle, \dots, |111\dots 1\rangle\}$. Quantum computation basically means that the wave function of this combined system undergoes an evolution according to Schrödinger's equation with a Hamiltonian that is designed for the algorithm which is to be carried out. In general, the wave function for computation will be a superposition of the 2^N basis states, i. e. an entangled state of the N qubits. Thus, in contrast to a classical computer, a quantum computer is able to do calculations with superpositions of numbers instead of just one discrete number from the set $\{(0, 0, 0, \dots, 0), (1, 0, 0, \dots, 0), (0, 1, 0, \dots, 0), \dots, (1, 1, 1, \dots, 1)\}$. Even though a measurement at the end of the computation collapses the wave function onto one of the basis states, this outcome in general depends on the entire superposition from which the computation was started. In principle, a quantum computer allows for (quantum) parallelism during its calculation. This means that the computation is carried out on a superposition of different paths which then interfere to give the final result. This parallelism possibly results in an exponential speedup of the calculation compared to classical computers.

2.4.2 Basic operations

In analogy to classical computation, the operations on single or more qubits at the one time are called gates. An example for a classical gate involving a single bit ϵ is given by the NOT-gate, which flips the state of the bit and results in $\neg\epsilon$. A classical gate involving two bits is the NAND-gate, which accepts two bits (ϵ_1, ϵ_2) as inputs and produces the output $\neg(\epsilon_1 \cdot \epsilon_2)$. This gate has the important feature that it is universal for classical computation, i. e. any classical operation on any finite number of bits can be constructed from this gate. For quantum computation the situation is similar. It has been shown [16] that any arbitrary unitary transformation on the quantum register, which is what one wants for quantum computation, can be constructed from one-qubit rotations and from a two-qubit gate called controlled-NOT (CNOT) gate. One-qubit rotations have the matrix form

⁴Polynomial (exponential) time means that the time required to run the algorithm grows as a polynomial (exponential) function of the number N of digits of L . In computer science problems which require polynomial time are considered solvable, whereas problems which require exponential time are considered intractable.

⁵The quantum bus is typically an auxiliary qubit which interacts with all qubits in the register with no direct interaction between the qubits of the register.

$$\begin{pmatrix} \cos(\theta/2) & \Leftrightarrow i e^{i\phi} \sin(\theta/2) \\ \Leftrightarrow i e^{-i\phi} \sin(\theta/2) & \cos(\theta/2) \end{pmatrix}$$

in the basis $\{|0\rangle, |1\rangle\}$ for some angles θ and ϕ and are well-known from the physics of spin $1/2$ systems in atomic physics and nuclear magnetic resonance. The CNOT gate, involving two qubits, has the matrix form

$$\begin{pmatrix} 1 & 0 & 0 & 0 \\ 0 & 1 & 0 & 0 \\ 0 & 0 & 0 & 1 \\ 0 & 0 & 1 & 0 \end{pmatrix}$$

in the basis $\{|00\rangle, |01\rangle, |10\rangle, |11\rangle\}$. The effect of this gate is to perform a NOT-operation on the second qubit (the target qubit) if the state of the first qubit (the control qubit) is 1. Otherwise, the state of the target qubit is left unchanged. At this point it should be noted that the quantum bus mentioned above is usually needed to implement this two-qubit gate. This will become clear when the implementation of the CNOT-gate with trapped ions is explained.

2.4.3 The requirements for a physical system and the Cirac/Zoller scheme

A very rudimentary quantum computer thus consists of a register of N qubits who can be manipulated according to the gates mentioned above. But even though a quantum computer is conceptually quite simple, an experimental realization poses some challenges. The reason is that quantum mechanical systems are usually microscopic systems. Their microscopic states need to be prepared at will, their (quantum mechanical) evolution needs to be controlled, and their final state needs to be read out with high efficiency. In addition, the information stored in a quantum system, called quantum information, is very delicate and subject to decoherence. Hence, very stringent requirements have to be fulfilled for a system to be a candidate for quantum computation. In more detail, the requirements for a physical system for quantum computation are the following:

1. The quantum system should consist of individual subsystems (the qubits) which are strongly coupled to each other, preferably via some quantum bus as we shall see later. 'Strongly' means that the coupling constant (in frequency units) dominates other rates such as decoherence rates.
2. The entire system (i. e. the qubits and the bus) must allow for deterministic⁶ preparation in a known quantum mechanical state before the computation.
3. The system must allow for easy coherent manipulation in order to realize the different gate operations.

⁶Deterministic means that a known quantum state must be prepared at a specified time. This is in contrast to a random process such as interaction of an atom in an atomic beam with a cavity mode [14, 15].

4. The evolution of the system is subject to no decoherence during computation.
5. The readout of the quantum information has to be done with high efficiency to preserve its quantum character.

Other requirements, which are important if quantum computation is used for large scale computing and if it wants to find technical applications, are:

6. The ability of fault tolerant computation and the possibility for error correction.
7. The scalability of the system, i. e. the possibility to use large quantum systems with many qubits for more intricate computations, or the possibility to create networks of quantum computers in order to scale up the system⁷.

A promising candidate for a model of a quantum computer has been suggested by I. Cirac and P. Zoller based on ions in a linear trap which interact via their Coulomb repulsion [10]. In principle, all 7 requirements listed above are met by this system. The quantum system consists of individual atoms, lined up along the axis of the trap, each of which carries a qubit, and these qubits are coupled to each other via their common motion in the trap. The register is thus provided by individual ions, and the bus is given by a quantized mode of (common) oscillation along the trap axis. It should be possible to prepare the entire system in a quantum state before computation. This is the ground state of motion in the trap for the bus achieved by laser cooling while all ions are in one well-defined electronic state. Laser pulses addressed to individual ions allow for the deterministic realization of any Hamiltonian evolution on the state space of the register. In particular, the building blocks of any quantum algorithm, the one-qubit rotations and the CNOT-gate, can be realized with appropriate laser pulses. The details of how to implement the operations will be discussed in the next section. Decoherence of internal states can be made arbitrarily small using ground states and/or metastable states (a coherence time of more than 10 minutes using hyperfine ground state levels in ${}^9\text{Be}^+$ has been achieved [47]), and decoherence on the bus should be small enough to allow for many computations. Finally, the quantum register can be read out with near unit efficiency using the quantum jumps technique⁸. All of this has already been achieved with a single ion [17], and there are no fundamental reasons why a generalization to more than one ion should not be possible. In addition, the requirements for large-scale computing could also be met. Recently, significant theoretical progress has been made on the field of quantum error correction [46]. Error correction will be needed because quantum superpositions are very susceptible to noise, and large quantum computers will need the ability of fault tolerant computation. Finally, networks of ion trap quantum computers could be constructed. This could be done by coupling individual ion trap quantum computers with the help of high finesse cavities and fibers to share common modes of light [51, 52].

⁷This requirement is for example not met by the NMR technique [12, 13].

⁸This technique [48, 49, 50] uses the presence of a third level. This level is coupled via a strongly fluorescing transition to only one of the states of the qubit, for example $|0\rangle$. Applying laser light to this transition then results in fluorescence if the atom is in state $|0\rangle$. On the other hand, no light is scattered if the atom is in state $|1\rangle$. Hence, the occupation probabilities in the two states can be measured with high efficiency by discriminating between fluorescence ON or fluorescence OFF.

2.4.4 Two-level system and the harmonic oscillator

This section describes in more detail the physics behind quantum computation with cold trapped ions. In particular, the basic mechanisms which are needed to implement simple quantum gates such as the CNOT gate are presented. For this, I will start out with the Hamiltonian describing the system and then discuss the relevant special cases.

In the linear ion trap quantum computer each qubit is represented by two electronic levels of a particular ion in a string of trapped ions. This is shown schematically in Fig. 2.8, where each ion carries a qubit. The analogy between a two-level system and a spin 1/2 system is used. The upper and lower level of the j -th ion are denoted by $|\uparrow\rangle_j$ and $|\downarrow\rangle_j$, respectively. The operators corresponding to this system are the raising and lowering operators

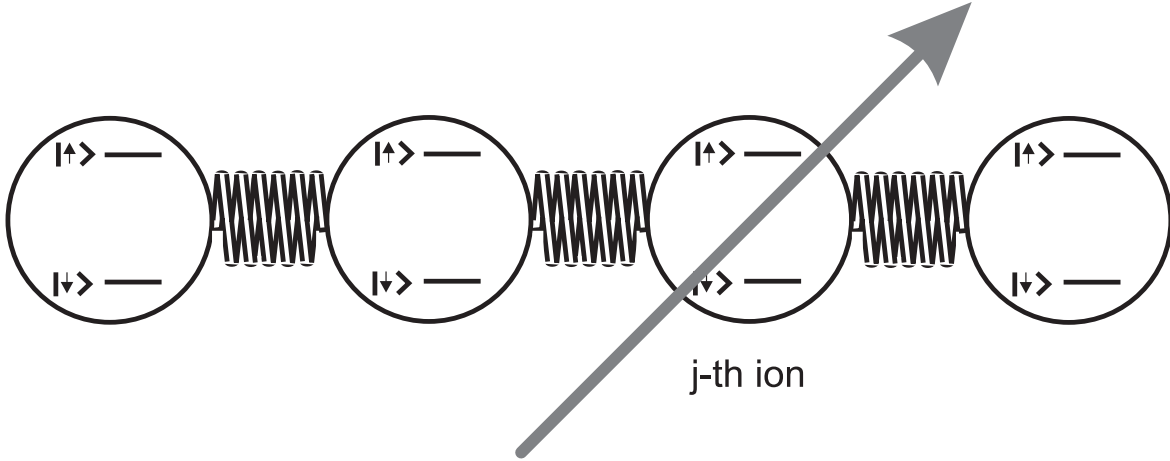


Figure 2.8: Schematic drawing of ions as qubits which are coupled harmonically. The j -th ion is addressed by a laser beam.

$\hat{\sigma}_+^j = |\uparrow\rangle_j\langle\downarrow|$ and $\hat{\sigma}_-^j = |\downarrow\rangle_j\langle\uparrow|$. The quantum bus (indicated schematically by the springs between the ions in Fig. 2.8) is represented by the mode operator \hat{a} of oscillation along the trap axis. It is assumed that the N qubits interact with only one of the possible N modes, e. g. with the center-of-mass mode with frequency $\omega_z = 2\pi\nu_z$, along the z -direction in the trap⁹. In any case, ideally, we have for each qubit the situation depicted in Fig. 2.9, where a two-level system is coupled to a harmonic oscillator. The harmonic oscillator states are denoted as usual by $|n\rangle = |0\rangle, |1\rangle, |2\rangle$ and so forth. Applying a laser with electric field $\mathbf{E}(\mathbf{r}) = \mathbf{E}_0 \cos(\mathbf{k} \cdot \mathbf{r} \Leftrightarrow \omega_L t + \phi)$ to the j -th ion in the string, the interaction Hamiltonian has the following form [53]:

$$\hat{H}_I = \hbar\Omega(\hat{\sigma}_+ + \hat{\sigma}_-)(e^{i(\mathbf{k}\cdot\hat{\mathbf{z}} - \omega_L t + \phi)} + e^{-i(\mathbf{k}\cdot\hat{\mathbf{z}} - \omega_L t + \phi)}). \quad (2.9)$$

In this formula the index j is omitted for clarity. Ω is the Rabi frequency and $\hat{\mathbf{z}} = z_0 \mathbf{e}_z (\hat{a} e^{-i\omega_z t} + \hat{a}^\dagger e^{i\omega_z t})$ is the axial position operator. \mathbf{e}_z denotes the unit vector in z -direction, and $z_0 =$

⁹This is possible because the mode frequencies are well separated. As an alternative, one might want to use one of the higher modes, e. g. the breathing mode.

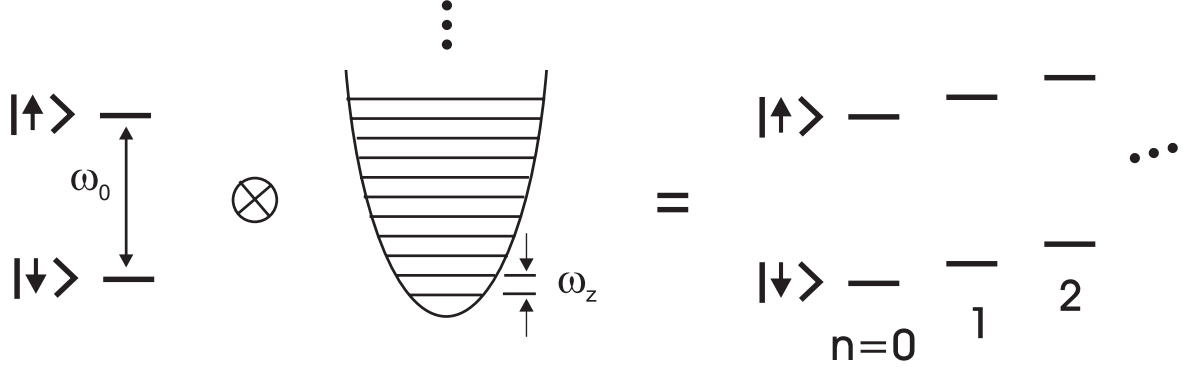


Figure 2.9: Two-level system with transition frequency ω_0 coupled to a harmonic oscillator with frequency ω_z .

$(\hbar/(2Nm\omega_z))^{1/2}$ is the spread of the ground state wave function for N ions with mass m . For a dipole transition, the Rabi frequency has the form $\Omega = \langle \uparrow | e\mathbf{r} | \downarrow \rangle \cdot \mathbf{E}_0 / (2\hbar)$. For a quadrupole transition, the case which is interesting to our experiment, the Rabi frequency is $\Omega = \langle \uparrow | (e\mathbf{r} \cdot \mathbf{E}_0)(\mathbf{r} \cdot \mathbf{k}) | \downarrow \rangle / (4\hbar)$. Here, \mathbf{r} denotes the (internal) position operator for the j -th ion and e is the electron's charge¹⁰. It is now assumed that the laser is tuned to $\omega_L = \omega_0 + (n' \Leftrightarrow n)\omega_z$, i. e. that it drives the $n' \Leftrightarrow n$ sideband. In a frame rotating with ω_L the interaction Hamiltonian is

$$\hat{H}_I = \hbar\Omega(\hat{\sigma}_+ e^{i\eta(\hat{a} + \hat{a}^\dagger) + i\phi} + \hat{\sigma}_- e^{-i\eta(\hat{a} + \hat{a}^\dagger) - i\phi}) \quad (2.10)$$

In this formula, the crucial parameter is $\eta = (\mathbf{k} \cdot \mathbf{e}_z)z_0$, the Lamb-Dicke parameter generalized to the case of N ions and including the angle between the propagation of the laser beam and the z -direction. As mentioned before, it describes the relative spread of the ground state wave function with respect to the laser wavelength and thus determines the coupling of the internal electronic to the external motional states.

In order to point out the basic operations which are needed for quantum gates I will, for the time being, assume that the amplitude of the ions' motion is much less than the laser wavelength, i. e. that $(2n+1)^{1/2}\eta \ll 1$. In the Lamb-Dicke limit the physics described by the Hamiltonian in Eq. (2.10) is reduced to three distinct processes. To see this, the exponential factors in Eq. (2.10) are expanded. Assuming $n' \Leftrightarrow n = 0$ and neglecting off-resonant terms, one gets¹¹

$$\hat{H}_I = \hbar\Omega(\hat{\sigma}_+ + \hat{\sigma}_-) \quad (2.11)$$

This Hamiltonian corresponds to excitation on the carrier of the qubit transition and is shown schematically in (A) of Fig. 2.10. For $n' \Leftrightarrow n = \Leftrightarrow 1$ one obtains

¹⁰Note that the definition of the Rabi frequency given here differs by a factor 2 from the definition given in [53]. It is therefore the frequency which describes the oscillation of the populations in a two-level system.

¹¹In the following the laser phase ϕ will sometimes be omitted for simplicity, but it is important to keep track of the phase when applying consecutive operations given by the Hamiltonian in Eq. (2.10).

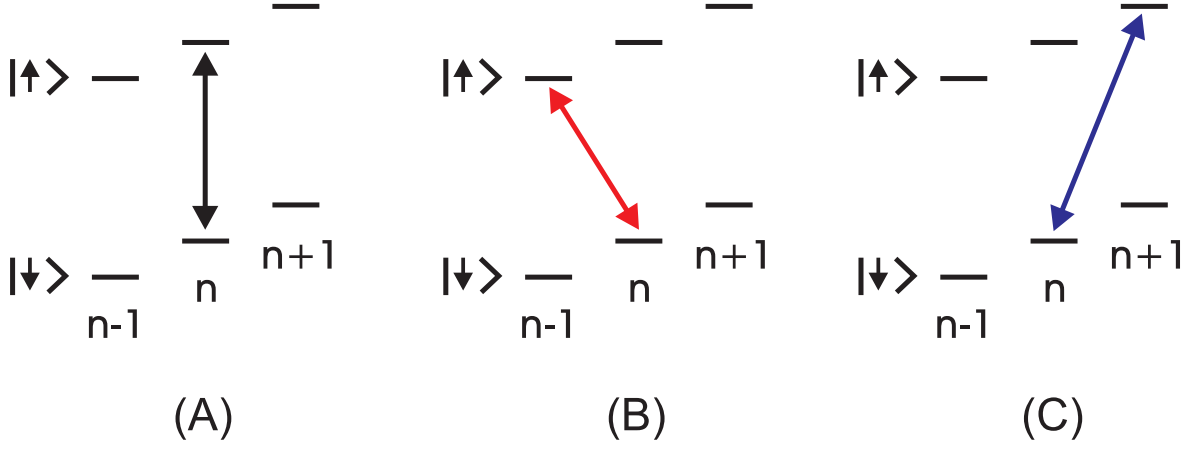


Figure 2.10: Basic processes in the Lamb-Dicke limit. (A) Transition on the carrier with Rabi frequency Ω . (B) Transition on the first red sideband with Rabi frequency $\eta n^{1/2}\Omega$. (C) Transition on the first blue sideband with Rabi frequency $\eta(n+1)^{1/2}\Omega$.

$$\hat{H}_I = i\eta\hbar\Omega(\hat{\sigma}_+\hat{a} \leftrightarrow \hat{\sigma}_-\hat{a}^\dagger). \quad (2.12)$$

And finally, for $n' \leftrightarrow n = +1$ one gets

$$\hat{H}_I = i\eta\hbar\Omega(\hat{\sigma}_+\hat{a}^\dagger \leftrightarrow \hat{\sigma}_-\hat{a}). \quad (2.13)$$

The last two processes are excitation on the first red sideband and first blue sideband, respectively. They are shown in Fig. 2.10 (B) and (C). The Hamiltonian for the excitation on the red sideband is the well known Jaynes-Cummings Hamiltonian introduced to describe the interaction of a two-level system with a single field mode. In this spirit, the Hamiltonian for blue sideband excitation is called the 'anti' Jaynes-Cummings Hamiltonian.

I will now focus on the lowest lying states of the combined spin 1/2 - harmonic oscillator system (see Fig. 2.9). As we will see later on, these are the ones which are important for quantum computation with trapped ions. From the Hamiltonians above we get the following evolution for the j-th ion: For excitation on the carrier the states $|\downarrow\rangle |n\rangle$ and $|\uparrow\rangle |n\rangle$ evolve according to (restoring the phase ϕ)

$$|\downarrow\rangle |n\rangle \mapsto \cos(\theta_c/2) |\downarrow\rangle |n\rangle \leftrightarrow ie^{i\phi} \sin(\theta_c/2) |\uparrow\rangle |n\rangle, \quad (2.14)$$

$$|\uparrow\rangle |n\rangle \mapsto \cos(\theta_c/2) |\uparrow\rangle |n\rangle \leftrightarrow ie^{-i\phi} \sin(\theta_c/2) |\downarrow\rangle |n\rangle. \quad (2.15)$$

Here, $\theta_c = \Omega t$ describes the 'rotation' between the two spin states. For $\theta_c = \pi/2, \pi$, or 2π one usually refers to a $\pi/2, \pi$, or 2π -pulse. These transformations are well known from nuclear magnetic resonance, and the oscillation between the two spin states is called Rabi flopping. In the language of quantum computing, these transformation are known as one-qubit rotations.

Excitation on the red sideband leaves the state $|\downarrow\rangle |0\rangle$ unaltered, whereas $|\downarrow\rangle |1\rangle$ and

2 Theory

$|\uparrow\rangle |0\rangle$ change to

$$|\downarrow\rangle |1\rangle \mapsto \cos(\theta_r/2) |\downarrow\rangle |1\rangle + e^{i\phi} \sin(\theta_r/2) |\uparrow\rangle |0\rangle, \quad (2.16)$$

$$|\uparrow\rangle |0\rangle \mapsto \cos(\theta_r/2) |\uparrow\rangle |0\rangle \Leftrightarrow e^{-i\phi} \sin(\theta_r/2) |\downarrow\rangle |1\rangle. \quad (2.17)$$

The angle $\theta_r = \eta\Omega t$ describes the rotation between states where the oscillation quantum number is changed. For e. g. $\theta_r = \pi$ the rotation is called a π -pulse on the red sideband.

Similarly, for excitation on the blue sideband we get the following evolution with $\theta_b = \eta\Omega t$:

$$|\downarrow\rangle |0\rangle \mapsto \cos(\theta_b/2) |\downarrow\rangle |0\rangle + e^{i\phi} \sin(\theta_b/2) |\uparrow\rangle |1\rangle, \quad (2.18)$$

$$|\uparrow\rangle |1\rangle \mapsto \cos(\theta_b/2) |\uparrow\rangle |1\rangle \Leftrightarrow e^{-i\phi} \sin(\theta_b/2) |\downarrow\rangle |0\rangle. \quad (2.19)$$

Here, the state $|\uparrow\rangle |0\rangle$ is unaffected.

Before proceeding to the next section where it is shown how these processes can be applied to implement quantum gates, I want to return briefly to the Hamiltonian in Eq. (2.10). Here, the Lamb-Dicke approximation has not been carried out yet. In fact, the potential of our linear trap with axial oscillation frequency ω_z of the order 100 to 200 kHz is so shallow that Doppler cooling (see section 2.7) does not carry us into the Lamb-Dicke regime. As we will see later, the spectra of the qubit transition show high order sidebands. This means that the assumption $(2n+1)^{1/2}\eta \ll 1$ is not fulfilled. Therefore, the full Hamiltonian in Equ. (2.10) has to be considered to understand these spectra. Coupling the states $|\downarrow\rangle |n\rangle$ and $|\uparrow\rangle |n'\rangle$ with a laser on the j -th ion, the generalized Rabi frequency is given by [53]

$$\begin{aligned} \Omega_{n,n'} &= \frac{1}{\hbar} \left| \langle n' | \langle \uparrow | \hat{H}_I | \downarrow \rangle | n \rangle \right| \\ &= \Omega \left| \langle n' | e^{i\eta(\hat{a} + \hat{a}^\dagger)} | n \rangle \right| \\ &= \Omega \eta^{|n'-n|} e^{-\eta^2/2} \sqrt{\frac{n_{<}!}{n_{>}!}} L_{n_{<}}^{|n'-n|}(\eta^2), \end{aligned} \quad (2.20)$$

where $n_{<}$ ($n_{>}$) is the greater (lesser) of n and n' and $L_\beta^\alpha(x)$ is the generalized Laguerre polynomial. Outside the Lamb-Dicke regime the Rabi frequencies in the formulas describing the evolution on the carrier and sidebands (see Eq. 2.14, 2.16, 2.18) have to be replaced by the generalized Rabi frequency $\Omega_{n,n'}^j$. As an example, consider the excitation of a single ion on the carrier of the qubit transition ($n = n'$). The probability of exciting the upper level P_\uparrow as a function of pulse duration t is given from Eq. (2.14) by

$$\begin{aligned} P_\uparrow &= \sum_{n=0}^{\infty} P_n \sin\left(\frac{\Omega_{n,n} t}{2}\right)^2 \\ &= \frac{1}{2} \left(1 \Leftrightarrow \sum_{n=0}^{\infty} P_n \cos(\Omega_{n,n} t) \right). \end{aligned} \quad (2.21)$$

In this equation an arbitrary occupation of the $|n\rangle$ -states is allowed by introducing the occupation probabilities P_n . For a thermal state these are given by

$$P_n = \frac{1}{(1 + \bar{n})} \left(\frac{\bar{n}}{(1 + \bar{n})} \right)^n, \quad (2.22)$$

where $\bar{n} = \langle n \rangle$ is the average occupation number. Equ. (2.21) is the usual formula one finds in textbooks (see e. g. [54]) which describes quantum collapses and revivals. Also, it is possible to phenomenologically introduce decoherence at this point. This can be done by inserting an exponential decay factor for each n :

$$P_{\uparrow} = \frac{1}{2} \left(1 \Leftrightarrow \sum_{n=0}^{\infty} P_n e^{-\gamma_n t} \cos(\Omega_{n,n} t) \right). \quad (2.23)$$

For our purposes it will suffice to use just a single decay constant $\gamma = \gamma_n$. We therefore get

$$P_{\uparrow} = \frac{1}{2} \left(1 \Leftrightarrow e^{-\gamma t} \sum_{n=0}^{\infty} P_n \cos(\Omega_{n,n} t) \right). \quad (2.24)$$

2.4.5 Quantum logic with trapped ions: The CNOT gate

In the following I will present the implementation of the CNOT gate along the lines of the proposal by Cirac and Zoller [10]. Because the CNOT gate is a two-qubit gate, I will consider 2 ions in the string, labeled by 1 and 2. The CNOT gate is then given by the transformation

$$\begin{aligned} |\downarrow\rangle_1 |\downarrow\rangle_2 &\mapsto |\downarrow\rangle_1 |\downarrow\rangle_2 \\ |\downarrow\rangle_1 |\uparrow\rangle_2 &\mapsto |\downarrow\rangle_1 |\uparrow\rangle_2 \\ |\uparrow\rangle_1 |\downarrow\rangle_2 &\mapsto |\uparrow\rangle_1 |\uparrow\rangle_2 \\ |\uparrow\rangle_1 |\uparrow\rangle_2 &\mapsto |\uparrow\rangle_1 |\downarrow\rangle_2. \end{aligned}$$

As mentioned before the target bit is flipped depending on the state of the control bit. The question then arises as to why it is so difficult to implement the CNOT gate? We will see below that the proposed implementation requires that the harmonic oscillator mode is in state $|0\rangle$ at the outset of the gate, i. e. that the string of ions has been cooled to the ground state of the mode.

It is first shown how a two-qubit gate with matrix

$$\begin{pmatrix} 1 & 0 & 0 & 0 \\ 0 & 1 & 0 & 0 \\ 0 & 0 & 1 & 0 \\ 0 & 0 & 0 & -1 \end{pmatrix}$$

can be realized with the operations from the last section. This gate is equivalent to the CNOT gate because one-qubit rotations transform this gate into the CNOT gate.

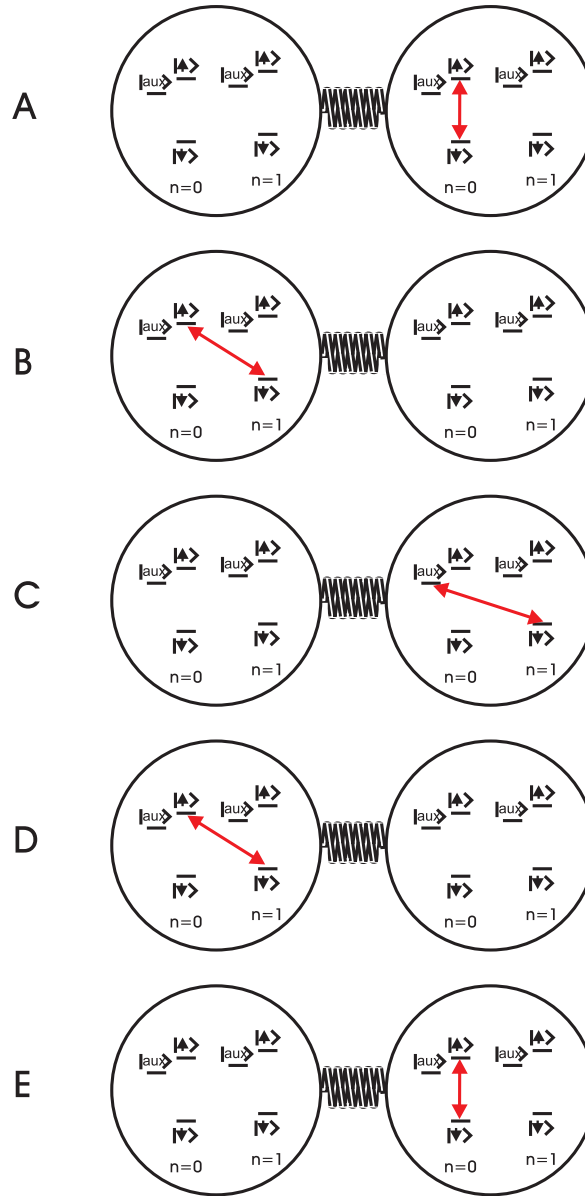


Figure 2.11: Pulse sequence for CNOT gate. A: $\pi/2$ -pulse on carrier for ion 2. B: π -pulse on the red sideband for ion 1. C: 2π -pulse on the red sideband for ion 2 on the auxiliary transition for ion 1. D: π -pulse on red sideband for ion 1. E: $\pi/2$ -pulse on carrier for ion 2.

For the two-qubit gate above, an auxiliary level is needed as shown in Fig. 2.11. The gate then requires 3 laser pulses. It is now assumed that the harmonic oscillator mode is in the ground state $|0\rangle$. First, a π -pulse is applied on the red sideband for ion 1. Then, the red sideband of the auxiliary transition for ion 2 is driven with a 2π -pulse. Finally, for step 3 the

first step is repeated.

$$\begin{aligned}
 |\downarrow\rangle_1 |\downarrow\rangle_2 |0\rangle &\mapsto |\downarrow\rangle_1 |\downarrow\rangle_2 |0\rangle \mapsto |\downarrow\rangle_1 |\downarrow\rangle_2 |0\rangle \mapsto |\downarrow\rangle_1 |\downarrow\rangle_2 |0\rangle \\
 |\downarrow\rangle_1 |\uparrow\rangle_2 |0\rangle &\mapsto |\downarrow\rangle_1 |\uparrow\rangle_2 |0\rangle \mapsto |\downarrow\rangle_1 |\uparrow\rangle_2 |0\rangle \mapsto |\downarrow\rangle_1 |\uparrow\rangle_2 |0\rangle \\
 |\uparrow\rangle_1 |\downarrow\rangle_2 |0\rangle &\mapsto \Leftrightarrow |\downarrow\rangle_1 |\downarrow\rangle_2 |1\rangle \mapsto |\downarrow\rangle_1 |\downarrow\rangle_2 |1\rangle \mapsto |\uparrow\rangle_1 |\downarrow\rangle_2 |0\rangle \\
 |\uparrow\rangle_1 |\uparrow\rangle_2 |0\rangle &\mapsto \Leftrightarrow |\downarrow\rangle_1 |\uparrow\rangle_2 |1\rangle \mapsto \Leftrightarrow |\downarrow\rangle_1 |\uparrow\rangle_2 |1\rangle \mapsto \Leftrightarrow |\uparrow\rangle_1 |\uparrow\rangle_2 |0\rangle
 \end{aligned}$$

Here, the second step is crucial because only $|\downarrow\rangle_2 |1\rangle$ is affected by the laser pulse. This introduces the sign change if and only if both ions are initially in the $|\uparrow\rangle$ state. Note that after the transformation the oscillator mode is back in the ground state. Also, before and after the gate the oscillator mode is not entangled with the ions' internal states. It has thus served as a quantum bus during the gate operation.

To show that this two-qubit gate is equivalent to the CNOT gate only one-qubit rotations on the second ion are needed. For this, consider $\pi/2$ -pulses with phases $\phi = \Leftrightarrow\pi/2$ and $\phi = \pi/2$ on the second ion. The spin states are transformed according to

$$\begin{aligned}
 |\downarrow\rangle &\mapsto \frac{1}{\sqrt{2}}(|\downarrow\rangle \mp |\uparrow\rangle), \\
 |\uparrow\rangle &\mapsto \frac{1}{\sqrt{2}}(|\downarrow\rangle \pm |\uparrow\rangle).
 \end{aligned}$$

A brief calculation shows that the CNOT gate is obtained when first applying the one-qubit gate with phase $\phi = \Leftrightarrow\pi/2$ on the second ion, then the two-qubit gate shown above, and finally the one-qubit gate with phase $\phi = \pi/2$ on the second ion.

2.4.6 Bell states

Another example of possible applications of cold trapped ions is the preparation of the so-called Bell states. These are 4 maximally entangled basis states for a two qubit system. They are the states which are usually used in textbooks to illustrate the famous EPR-paradoxon [55]. The states are given by

$$|\Phi^\pm\rangle = \frac{1}{\sqrt{2}}(|\downarrow\rangle_1 |\downarrow\rangle_2 \pm |\uparrow\rangle_1 |\uparrow\rangle_2), \quad (2.25)$$

$$|\Psi^\pm\rangle = \frac{1}{\sqrt{2}}(|\uparrow\rangle_1 |\downarrow\rangle_2 \pm |\downarrow\rangle_1 |\uparrow\rangle_2). \quad (2.26)$$

Again, one starts out with the ground state of the entire system: $|\downarrow\rangle_1 |\downarrow\rangle_2 |0\rangle$. The states $|\Phi^+\rangle$ and $|\Phi^-\rangle$ are then generated by first applying a $\pi/2$ -pulse on the blue sideband of the first ion (phase $\phi = 0$ for $|\Phi^+\rangle$ and phase $\phi = \pi$ for $|\Phi^-\rangle$). Subsequently, a π -pulse is

applied on the red sideband of the second ion:

$$\begin{aligned}
 |\downarrow_1 \downarrow_2 |0\rangle &\mapsto \frac{1}{\sqrt{2}}(|\downarrow_1 \downarrow_2 |0\rangle + |\uparrow_1 \downarrow_2 |1\rangle) \\
 &\mapsto \frac{1}{\sqrt{2}}(|\downarrow_1 \downarrow_2 |0\rangle + |\uparrow_1 \uparrow_2 |0\rangle) \\
 &= \frac{1}{\sqrt{2}}(|\downarrow_1 \downarrow_2 + |\uparrow_1 \uparrow_2\rangle)|0\rangle, \\
 |\downarrow_1 \downarrow_2 |0\rangle &\mapsto \frac{1}{\sqrt{2}}(|\downarrow_1 \downarrow_2 |0\rangle \Leftrightarrow |\uparrow_1 \downarrow_2 |1\rangle) \\
 &\mapsto \frac{1}{\sqrt{2}}(|\downarrow_1 \downarrow_2 |0\rangle \Leftrightarrow |\uparrow_1 \uparrow_2 |0\rangle) \\
 &= \frac{1}{\sqrt{2}}(|\downarrow_1 \downarrow_2 \Leftrightarrow |\uparrow_1 \uparrow_2\rangle)|0\rangle.
 \end{aligned}$$

For the states $|\Psi^- \rangle$ and $|\Psi^+ \rangle$, one first prepares $|\Phi^+ \rangle$ and $|\Phi^- \rangle$ and then applies a π -pulse on the carrier of the first ion to flip the spin:

$$\begin{aligned}
 |\downarrow_1 \downarrow_2 |0\rangle &\mapsto \frac{1}{\sqrt{2}}(|\downarrow_1 \downarrow_2 + |\uparrow_1 \uparrow_2\rangle)|0\rangle \\
 &\mapsto \frac{1}{\sqrt{2}}(|\uparrow_1 \downarrow_2 \Leftrightarrow |\downarrow_1 \uparrow_2\rangle)|0\rangle, \\
 |\downarrow_1 \downarrow_2 |0\rangle &\mapsto \frac{1}{\sqrt{2}}(|\downarrow_1 \downarrow_2 \Leftrightarrow |\uparrow_1 \uparrow_2\rangle)|0\rangle, \\
 &\mapsto \frac{1}{\sqrt{2}}(|\uparrow_1 \downarrow_2 + |\downarrow_1 \uparrow_2\rangle)|0\rangle.
 \end{aligned}$$

In general, higher order maximally entangled states such as GHZ states in the case of 3 qubits and so forth can be generated. States like these might in the future find applications in new tests of quantum mechanics [7] and improved spectroscopy [6, 56].

3 Experimental Setup

This chapter first describes the apparatus with the linear trap and then the laser systems

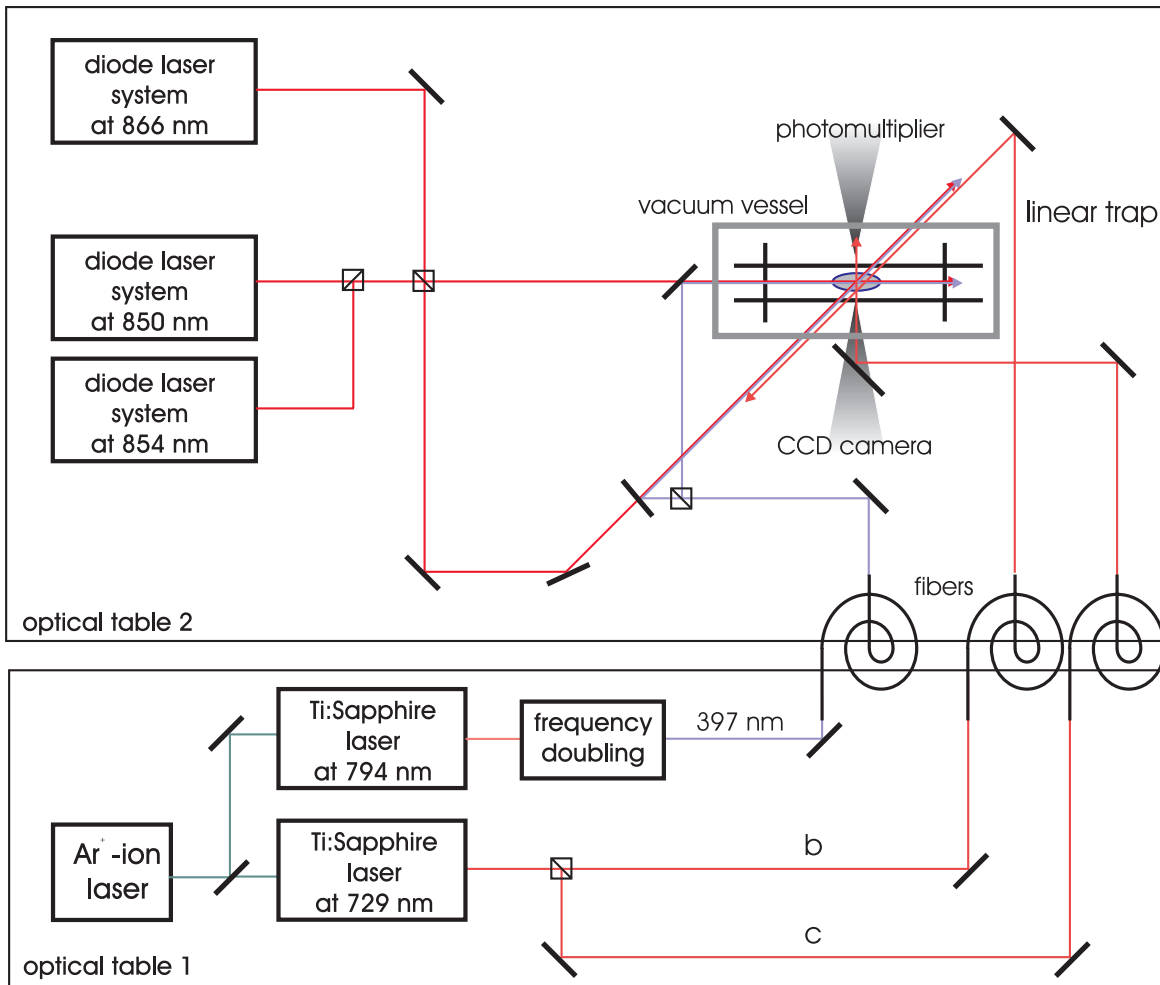


Figure 3.1: General experimental setup. The experiment is spread over two optical tables. The Ti:Sapphire lasers together with their Ar^+ pump laser are located on one table, the vacuum vessel containing the linear trap and the diode lasers are on the other table.

needed for trapping and manipulating individual Ca^+ ions. A general overview over the

entire setup is provided in Fig. 3.1. This consists of the linear trap (inside an ultra-high vacuum system, not shown in detail), detection systems (photomultiplier and CCD camera), and laser systems at five different wavelengths. One computer controls the CCD camera, another computer controls all laser wavelengths, pulse durations, and data acquisition. Two wavelengths are produced by Ti:Sapphire lasers. These are the wavelength at 397 nm, which is generated by frequency doubling and therefore requires a powerful pumping laser, and the wavelength at 729 nm, where narrow bandwidth light is needed which in turn requires a highly stable laser. Both Ti:Sapphire lasers are located on a separate table in order to isolate the ion trap from vibrations of the Argon ion pump laser. The light is then coupled into fibers and guided to the table with the ion trap. The lasers at 850, 854, and 866 nm are diode lasers. They are located close to the trap. Their light is superimposed with the light at 397 nm and 729 nm and shone onto the ions from various directions as can be seen in Fig. 3.2). The coordinate system used in the following is also indicated in this figure. Details on the laser beam geometry are given below.

3.1 Experimental setup: Ion trap apparatus

3.1.1 Vacuum vessel, trap electrodes, rf drive, fluorescence detection

Vacuum vessel: The requirements for a vacuum vessel include optical access for the laser beams from various directions and the possibility to place the lenses for fluorescence collection close enough to the trap. Consequently, as shown in Fig. 3.3, we chose a CF 63 double cross with extra CF 35 flanges in the plane $x = 0$ and in the plane $y = 0$. The directions for fluorescence collection are furnished with inverted viewports which allow one to place the front side of the lenses up to 45 mm to the trap center (see Fig. 3.7). The only directions which cannot be used for laser beams are the $(x, y, z) = \pm(0, 1, 1)$ directions which are used by the Ca oven and the electron gun. The Ca oven consists of a 40 mm long steel tube filled with Ca through which a current is sent for heating. An aperture 30 mm away from the trap center serves for narrowing the atomic beam so that deposition of Ca on the trap electrodes is reduced. The electron gun is a commercial oscilloscope electron beam unit¹. Most of the windows are tilted by 6° so that the back reflection from a beam exiting the vessel can be blocked with an aperture (not shown). The helical resonator for the rf-drive field (see below) is placed on top of the vessel close to the vacuum feedthroughs. The trap electrodes are attached close to these feedthroughs in the center of the vessel. During its lifetime, the vessel has been baked out a few times with temperatures above 300°C . After the last opening the vessel has been baked out at 200°C for a week. It is now continuously pumped by a 20 l/s ion getter pump² to a pressure of better than 10^{-9} mbar. The pressure is determined by measuring the current through the getter pump. In view of the fact that there is a leakage current of the same magnitude with removed magnets of the getter pump, this measurement leads only to an upper bound for the pressure. At these low pressures, other measurements would be more reliable, e. g. inferring the pressure from the quantum jump rate to the metastable $D_{5/2}$ level. For our purposes the vacuum is sufficient because the lifetime of trapped and laser-cooled ions

¹Elektronenkanone, System 13-620, AEG, Ulm.

²VacIon Plus 20 with controller MiniVac, Varian.

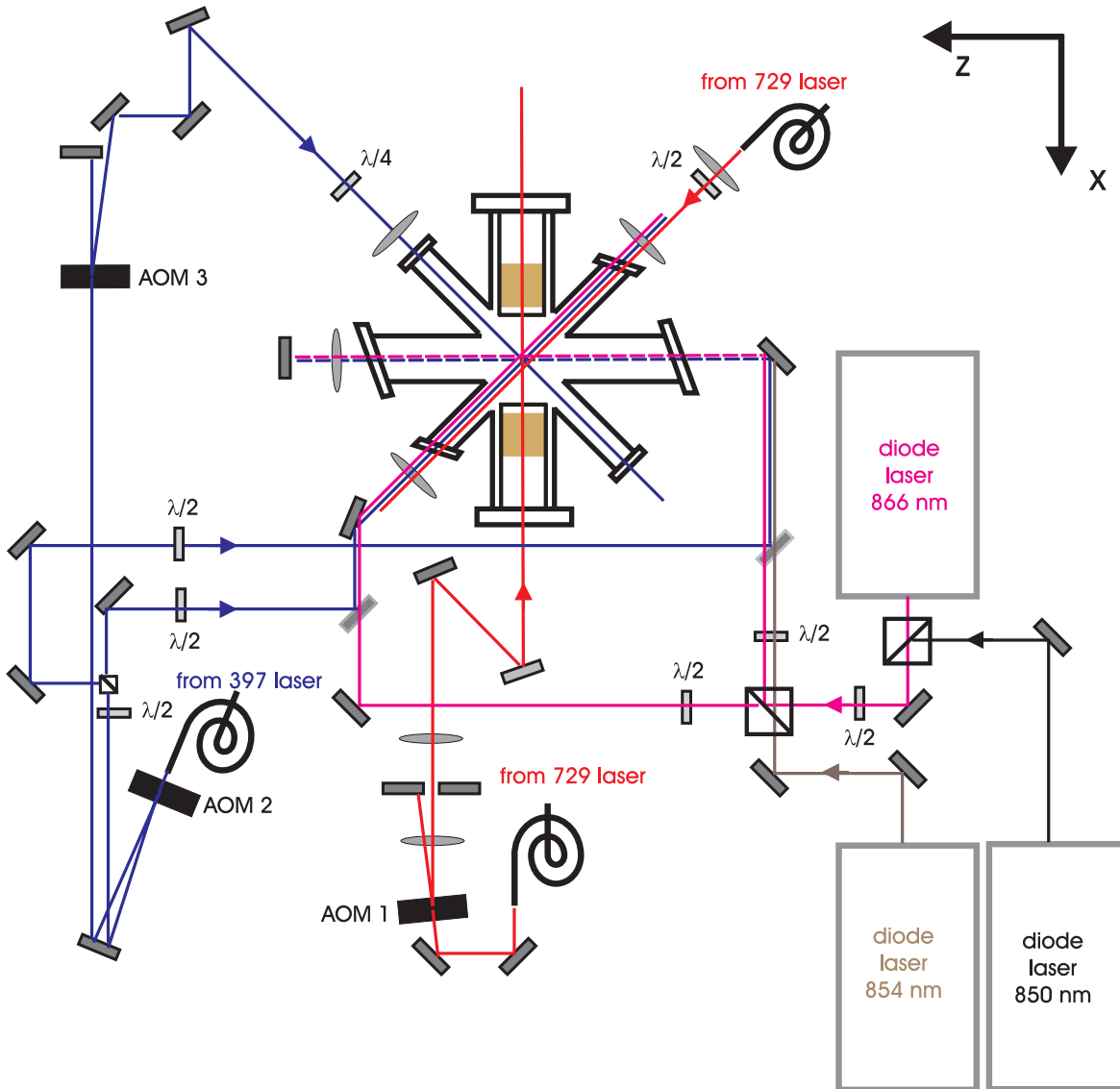


Figure 3.2: Laser setup near trap. The y -direction points out of the plane of the drawing. The dashed beams travel underneath the vacuum vessel from right to left and then enter the trap in the $(x, y, z) = (0, 1, \Leftrightarrow 1)$ direction. AOM 1 is used for spatially displacing the 1st order beam at 729 nm meant for addressing individual ions. AOMs 2 and 3 shutter the beams at 397 nm used for Doppler cooling and detection and for Zeeman ground state preparation, respectively. $\lambda/2$ and $\lambda/4$ denote half- and quarter-waveplates used for polarization control.

is many hours.

3 Experimental Setup

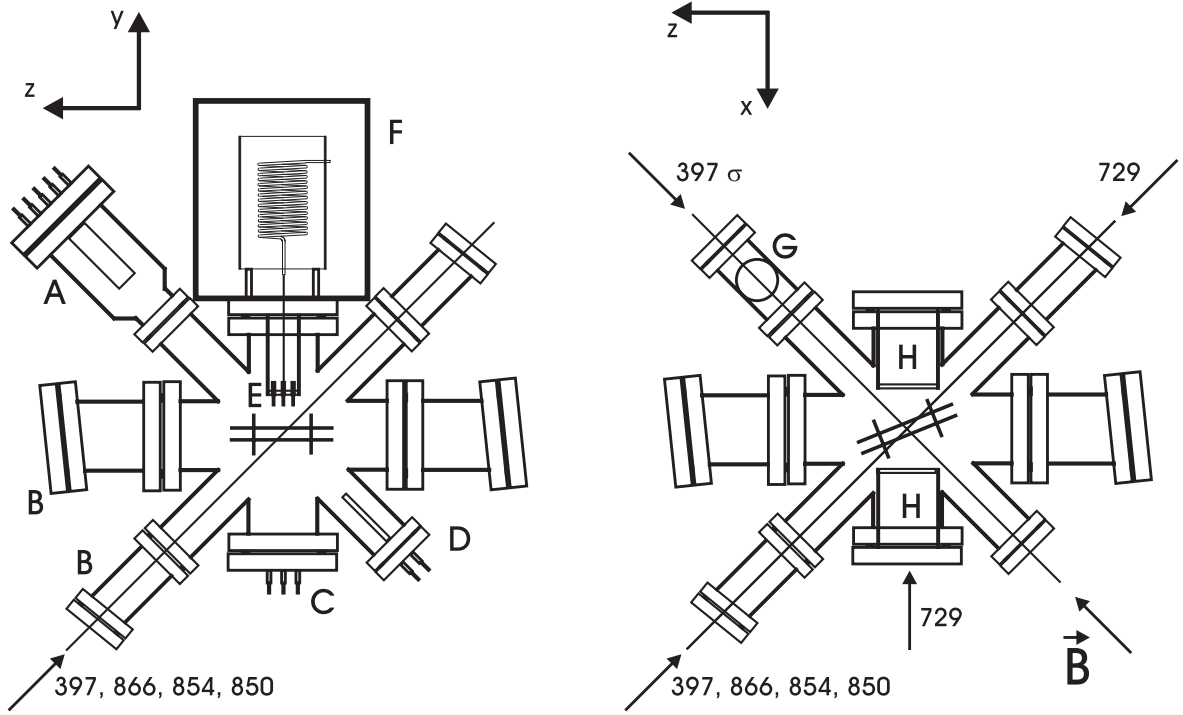


Figure 3.3: Vacuum vessel and geometry for laser excitation. Left: Plane $x = 0$. (A) electron gun, (B) tilted windows, (C) feedthroughs for compensation electrodes, (D) Ca oven, (E) feedthroughs for rf-drive field, (F) helical resonator with rf-shielding. Right: Plane $y = 0$. (G) CF 35 cross with ion getter pump and valve (not shown), (H) inverted viewports. The size of the linear trap in the center of the vessel is exaggerated for clarity.

Trap geometry: Our linear trap is the result of a compromise concerning the necessary storage parameters, the openness to laser beams from various directions and the openness for detection optics, and the belief that dangerous patch effects can be of minimal effect if the electrodes are far away from the ions. Therefore, as shown in Fig. 3.4 we have chosen a fairly large and open design. The trap consists of 4 stainless steel rods with a diameter of $d = 0.6$ mm and a radial distance $R = 1.18$ mm, diagonally connected to generate the quadrupole rf field for dynamic confinement in the radial direction. Two ring electrodes with dc potentials serve for static longitudinal confinement. These rings have an outer diameter of 6 mm, and the spacing between them is $L = 10$ mm. This spacing was chosen to allow for laser beam access under 45° and for suitable longitudinal oscillation frequencies (100 to 200 kHz) for reasonable ring voltages (50 to 200 V). The electrodes for micromotion compensation consist of two pairs of electrodes which are parallel to the quadrupole electrodes spaced approximately 20 mm away from the center axis of the trap (not shown in Fig. 3.4). Each pair is symmetric with respect to the trap center axis so that a voltage on these electrodes pushes the ions perpendicular to the plane defined by the pair. A rather large distance from these pairs to

the trap center was chosen so that it can be expected that the applied fields are constant across the ions and that patch effects on these electrodes play a reduced role. The drawback of this construction is the fact that we need to apply relatively high voltages ($\simeq 700$ V) to these electrodes.

As can be seen in Fig. 3.3 the electrodes are rotated in the plane $y = 0$ by an angle of 22.5° with respect to the z -axis³. It is thus possible to address the ions through the lenses inside the inverted viewports (Fig. 3.7) while still having a k -vector component in the axial direction of the trap.

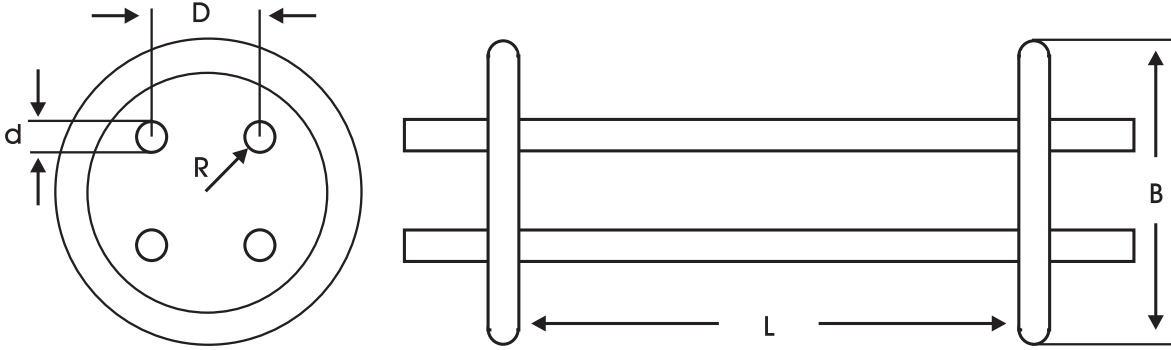


Figure 3.4: Electrode configuration. All electrodes have a diameter of $d=0.6$ mm. Other dimensions: $D=2.1$ mm, $R=1.18$ mm, $L=10$ mm, $B=6$ mm.

Rf drive: The drive voltage for the ac field on the quadrupole electrodes is produced in a helical resonator [57] (quality factor $Q \simeq 250$) which is driven by a function generator⁴ and a 5 W amplifier⁵ (see Fig. 3.5) at 18 MHz. In addition there is a variable attenuator for adjusting the power to the amplifier and a power and reflecto meter⁶ which measures forward and reflected power. The input power to the helical resonator is usually on the order of 1 W. This produces voltages around 800 V resulting in a radial secular frequency of about 1.4 MHz. A plot of the radial secular frequency as a function of input power to the helical resonator is shown in Fig. 3.6. The helical resonator, mounted on top of the vacuum chamber close to the vacuum feedthroughs to the electrodes, has a metal shielding to reduce the rf stray field. Without the shielding some of the diode laser electronics, photo diode amplifiers, and photon counting electronics do not work properly because of pick-up at 18 MHz. Most of the residual rf stray fields seem to exit from the vacuum windows where by necessity no perfect shielding is possible.

³The axial direction in the trap, also denoted by z in Fig. 2.1, does therefore not agree with the z -direction given by the coordinate system attached to the vacuum vessel. However, from the context it will always be clear which coordinate system is used.

⁴Synthesized function generator DS345, Stanford Research Systems.

⁵ZHL-5W, Mini Circuits.

⁶Daiwa CN-410M.

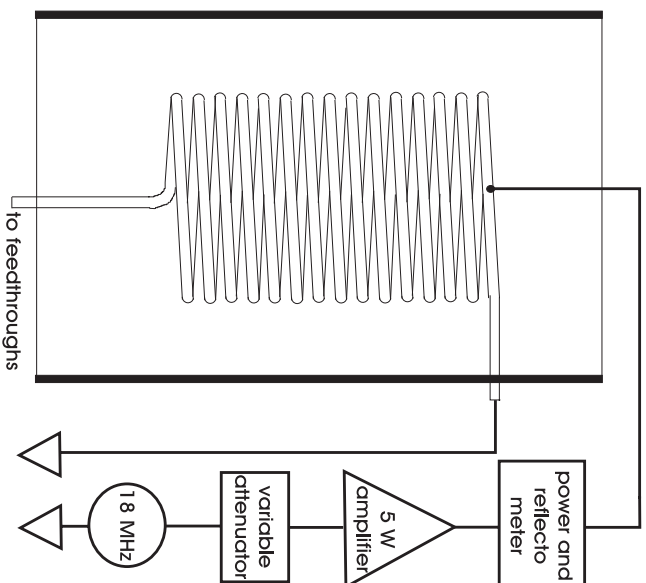


Figure 3.5: Helical resonator for voltage buildup. Copper coils and surrounding copper cylinder (diameter 100 mm) constitute a quarter wave resonator with resonances at $\lambda/4, 3\lambda/4, \dots$

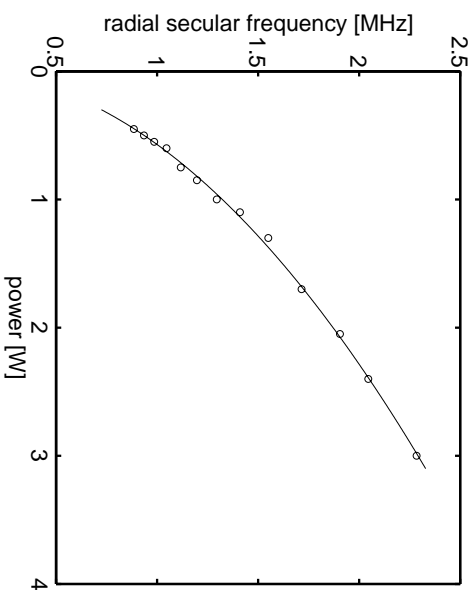


Figure 3.6: Radial secular frequency vs. input power at 18 MHz to helical resonator. The secular frequency was measured by resonantly exciting the ions' radial oscillation with an rf field (see Sect. 4.2). The continuous curve is a square root fit to the data (see Eq. 2.2).

Laser beams: As shown in Fig. 3.2 and Fig. 3.3 the Doppler cooling and repumping beams at 397 nm and 866 nm are superposed and enter the vacuum vessel in the $(x, y, z) = (0, 1, \Leftrightarrow 1)$ and $(x, y, z) = (\Leftrightarrow 1, 0, \Leftrightarrow 1)$ directions. This assures that the ions are laser-cooled in all 3 dimensions. The power in these beams is controlled by AOMs. The reset laser at 854 nm and the laser at 850 nm also enter from these directions, although typically only one direction is used. The lasers in the $(x, y, z) = \pm(1, 0, 1)$ directions are directed through the ring electrodes. The laser at 729 nm enters from the $(1, 0, 1)$ and the $(\Leftrightarrow 1, 0, 0)$ directions. The advantage of using the $(\Leftrightarrow 1, 0, 0)$ direction is given by the ability to focus the light to a spot with a waist of less than $5 \mu\text{m}$ by using the lens for fluorescence collection. For all current experiments where single ion addressing is not required (see chapter 5) we have used the $(1, 0, 1)$ direction. An additional beam at 397 nm enters from the $(1, 0, \Leftrightarrow 1)$ direction. This beam with wavevector parallel to the magnetic field \mathbf{B} is used for optical pumping into one of the Zeeman sublevels of the $S_{1/2}$ ground state. The polarisations of all beams can be controlled by means of zero order waveplates.

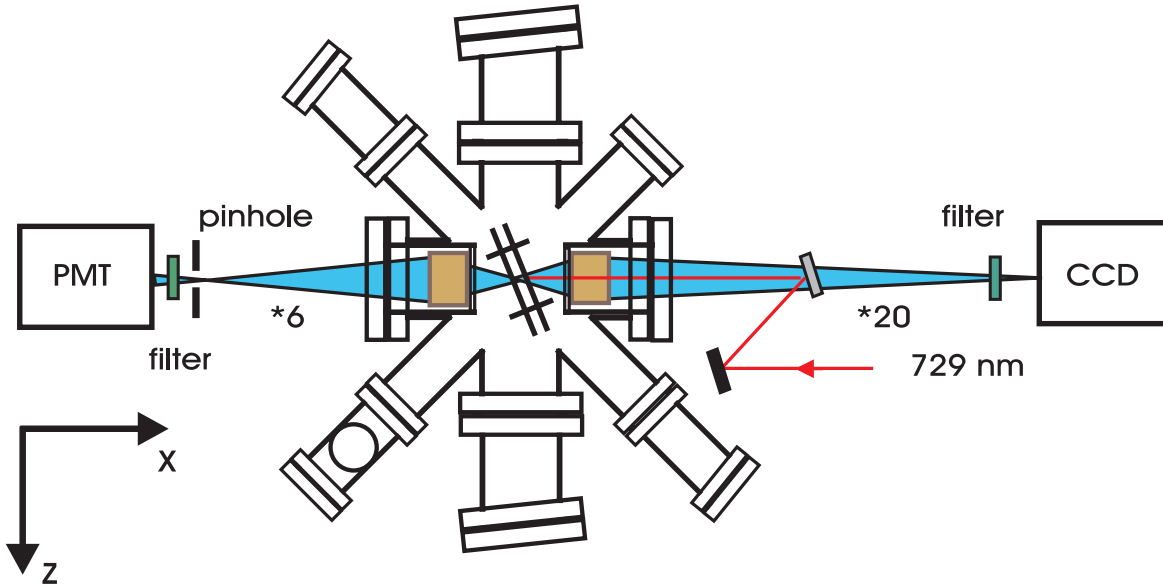


Figure 3.7: Detection setup at 397 nm. Both lenses for fluorescence collection are placed inside an inverted viewport. The magnification factors for PMT and CCD light paths are 6 and 20, respectively.

Fluorescence detection: We monitor the ions' fluorescence at 397 nm in the $(x, y, z) = (\Leftrightarrow 1, 0, 0)$ direction with a photomultiplier tube, PMT⁷. The quantum efficiency is specified to be 20%. The PMT has single photon counting capability. It has a dark count rate of 50 counts/s at room temperature. For the PMT the light is collected with a commercial microscope lens⁸ which is placed inside the inverted viewport. The light is focused with a slight

⁷H5773P-03, Hamamatsu.

⁸Nikon MNH-23150 ED Plan 1.5x, f-number $\simeq 1.5$.

enlargement factor of 6 onto a 1 mm pinhole to reduce stray light. The PMT together with a filter is right behind the pinhole, and both can be adjusted together in all 3 dimensions with a XYZ slide. The pulses from the PMT are amplified 25 times⁹ and sent to the discriminator inside a stand-alone photon counter¹⁰. Typical count rates are up to 12 kHz per ion. For low speed applications the photon counter is used for counting the pulses (the data is then read out via GPIB). This is the case for example when the ions' fluorescence is monitored continuously with a typical gate time of 100 ms. For high speed applications such as pulsed spectroscopy (see chapter 5) where many data sets need to be stored in a short time the discriminated pulses (NIM-level) are sent to a NIM-TTL converter and then to a counter on a PC card.

In the opposite $(x, y, z) = (1, 0, 0)$ direction an intensified CCD camera¹¹ is used (see Fig. 3.7). The quantum efficiency for the CCD is approx. 15%. The light for the CCD camera is also collected with a Nikon lens inside an inverted viewport. The enlargement factor is 20 in order to resolve the ions sufficiently on the CCD. We achieve a resolution of about 3 μm without the mirror which is used to couple in the light at 729 nm along the direction of observation (see Fig. 3.7), and a somewhat reduced resolution (5 μm) with this mirror. The inter-ion spacing is on the order of 10 to 20 μm , so the ions appear well resolved on the CCD whose pixel size is 21 $\mu\text{m} \cdot 21 \mu\text{m}$. The chosen enlargement factor is a compromise concerning the resolution of individual ions and the collection of sufficient light per pixel. Since the direction of observation and the axis of the trap have an angle of 67.5° we are able to view the ions' motion not only when the ions move laterally or vertically but also when they move back and forth. This can provide valuable information about the ions' change in position when compensating for micromotion (see below). On the other hand, for longer ion chains some of the ions are always a little bit out of focus (see e. g. Fig. 4.1 where the image of the center ions is focused but not for the outer ions.). This agrees with the calculated depth of focus of approximately 15 μm . The camera software provides background subtraction which allows us to subtract much of the stray light. Generally, we do not cool the camera when we use it just for monitoring purposes. Only if we need to integrate for a long time (to record, for example, the ions' modes of oscillation) we use the possibility to Peltier cool the CCD chip. Typical count rates on the CCD camera are 700000 counts per second and per ion, summed over all pixels where the ion is imaged onto. In principle, together with pixel binning, it is possible to implement integration times of 1 ms or less in order to use the CCD as a fast position dependent photomultiplier (even though the camera has not the ability for single photon counting).

Computer control: The entire experiment is controlled by two computers, one responsible for the configuration and readout of the CCD camera, the other responsible for laser detuning, PMT data collection, and timing of the experiment. For this, a data acquisition board¹² gives out scan voltages and counts TTL pulses from the PMT, a GPIB board¹³ allows for

⁹Preamplifier SR445, Stanford Research Systems.

¹⁰SR400, Stanford Research Systems.

¹¹ICCD, Princeton Instruments.

¹²AT-MIO-16XE-50, National Instruments.

¹³AT-GPIB/TNT, National Instruments.

communication with GPIB instruments (such as function generators, photon counter, lock-in amplifier), and a timing board¹⁴ is responsible for high precision experiment timing (such as absorption spectra on the $S_{1/2} - D_{5/2}$ quadrupole transition). All cards are programmed using LabView¹⁵.

3.2 Experimental setup: Lasers

Both Ti:Sapphire lasers and the diode lasers are frequency stabilized by the same technique, namely frequency modulation spectroscopy on an optical resonator. This technique, known as Pound-Drever-Hall stabilization [58] when applied to laser stabilization, allows one to narrow the laser linewidth to the kHz-level and below. In general, the requirements for lasers which are used for a dipole transition (typical natural width of a few MHz) are much less stringent than for those that are used to resolve a narrow quadrupole transition (typical natural width of mHz). For the dipole transitions it generally suffices to stabilize the lasers to the level that laser-cooling can be applied efficiently. If one wants to resolve narrow structures such as dark resonances more efforts are required. Definitely more efforts are required for the laser on the quadrupole transition. The coherence time on the $S_{1/2} - D_{5/2}$ transition will not be limited by the natural lifetime but by the laser coherence time (and possibly other time scales such as the decoherence time due to magnetic field fluctuations). In addition to short-term frequency stability the lasers in general need to be stabilized against drifts. This can be done by using a highly drift stable optical resonator or by locking the laser to an atomic resonance.

3.2.1 Frequency doubled Ti:Sapphire laser for 397 nm

The light from a commercial Ti:Sapphire laser¹⁶ at 794 nm (1.6 to 2.0 W) is split into one main beam which is directed towards the doubling resonator and three auxiliary beams as shown in Fig. 3.8. One of these beams passes on to a wavemeter, the second one is superposed with light at 729 nm and is directed towards a drift lock cavity (details see below), and the third one enters an electro-optical modulator (EOM)¹⁷ on the way to a stabilization cavity (finesse $F=100$). With the Pound-Drever-Hall locking technique the laser has a linewidth of approx. 200 kHz. This could be significantly improved with the help of a fast intra-cavity EOM. Presently, the servo loop uses solely the commercial tweeter piezo with a bandwidth of 18 kHz. The enhancement cavity with an LBO crystal for efficient frequency doubling is locked to the 794 nm laser by the Hänsch-Couillaud technique [59]. Up to 80 mW of power at 397 nm is generated, which then passes through a skewed lens for compensation of astigmatism and is coupled into a fiber via a telescope. An AOM in front of the fiber (1st order efficiency 80%) is used for fast ON-OFF switching with a high ON-OFF ratio (no measurable amount of light exits the fiber in the OFF state). The transmission through the fiber is 20% at maximum (the fiber is actually made for 493 nm). Typically we use about 8 to 10 mW behind the fiber. The laser is detuned by scanning the voltage on the piezo of the reference cavity. This allows for a scanning range up to 5 GHz. When the laser is locked to the cavity it still shows a

¹⁴PC-TIO-10, National Instruments.

¹⁵National Instruments.

¹⁶CR-899, Coherent.

¹⁷LM 0202 Phas, Gsänger.

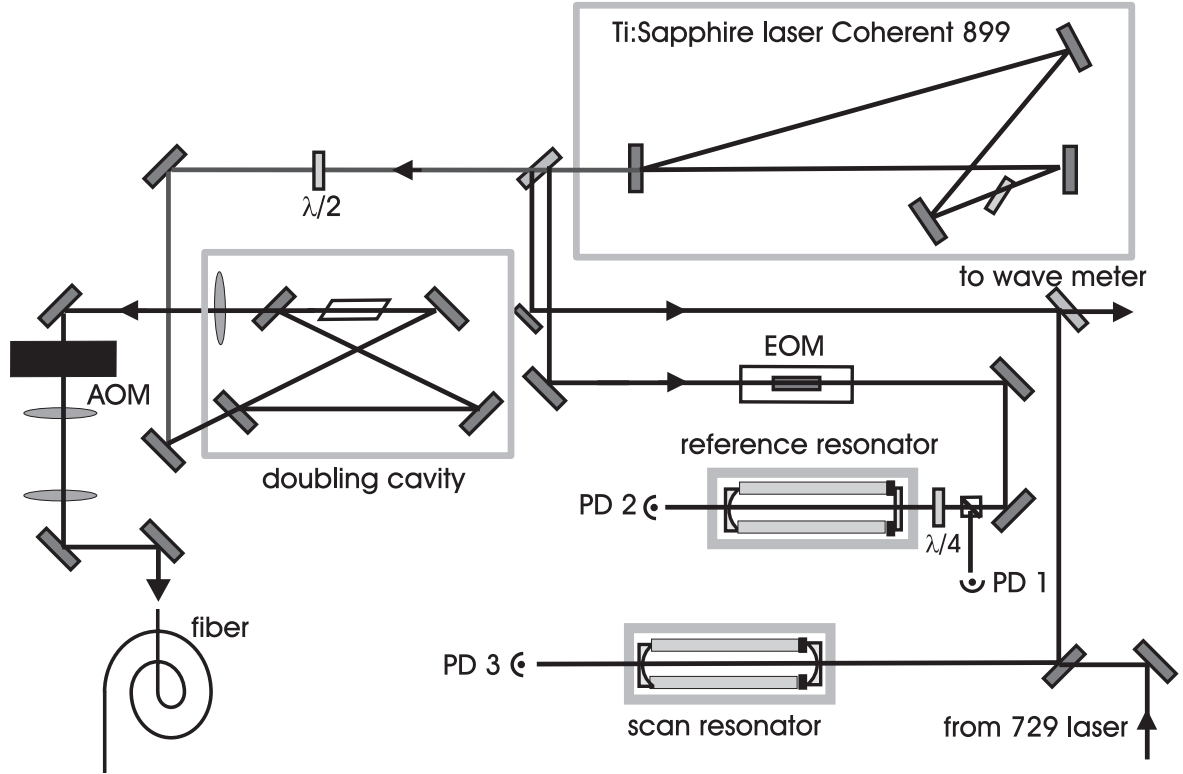


Figure 3.8: Setup for 397 nm laser. The Ti:Sapphire laser is only shown schematically. PD 2 is a monitoring photodiode, PD 3 is used to detect the transmission peaks for the drift lock, PD 1 is used for deriving the Pound-Drever-Hall error signal. The AOM is used for fast ON-OFF switching in front of the fiber.

drift with respect to the atomic resonance of up to 1 MHz/min. This drift, which can mostly be attributed to the piezo, is discussed further down in the context of diode lasers. In order to avoid this drift we lock the stabilization cavity to the highly stable laser at 729 nm. For this, the light which is superposed with the light at 729 nm is sent to a scanning cavity. This cavity is continuously scanned at a rate of 100 Hz. The idea is to keep the distance (in frequency units) between the 794 nm and 729 nm transmission peaks constant. An error signal is created by comparing the voltage on a charged capacitor to a reference voltage. The capacitor is charged during the time between two trigger points given by scanning first across one TEM_{00} transmission peak of one laser and then across a neighboring TEM_{00} transmission peak of the other laser. The amplified and integrated error signal is fed back to the piezo of the stabilization cavity. We measure the resulting drift stability to be better than 5 MHz/hour with respect to the atomic resonance. This has been done by comparing the rms error signal with the free spectral range of the cavity. The same result has been obtained by applying the same technique to a diode laser at 866 nm and then measuring the drift with the help of a beat measurement with another diode laser at 866 nm locked to a drift stable cavity.

3.2.2 Ultra stable Ti:Sapphire laser for 729 nm

The light from a commercial Ti:Sapphire laser¹⁸ at 729 nm (300 to 350 mW) is directed towards an AOM¹⁹ in double pass for detuning, power control, and fast ON-OFF switching. This is shown in Fig. 3.9. Since the AOM allows for only one polarization (parallel to the k-vector of the acoustic wave with 1st order efficiency 60%) it is not possible to use the standard technique for double pass where one uses a $\lambda/4$ waveplate and polarizing beam splitter. Instead, the

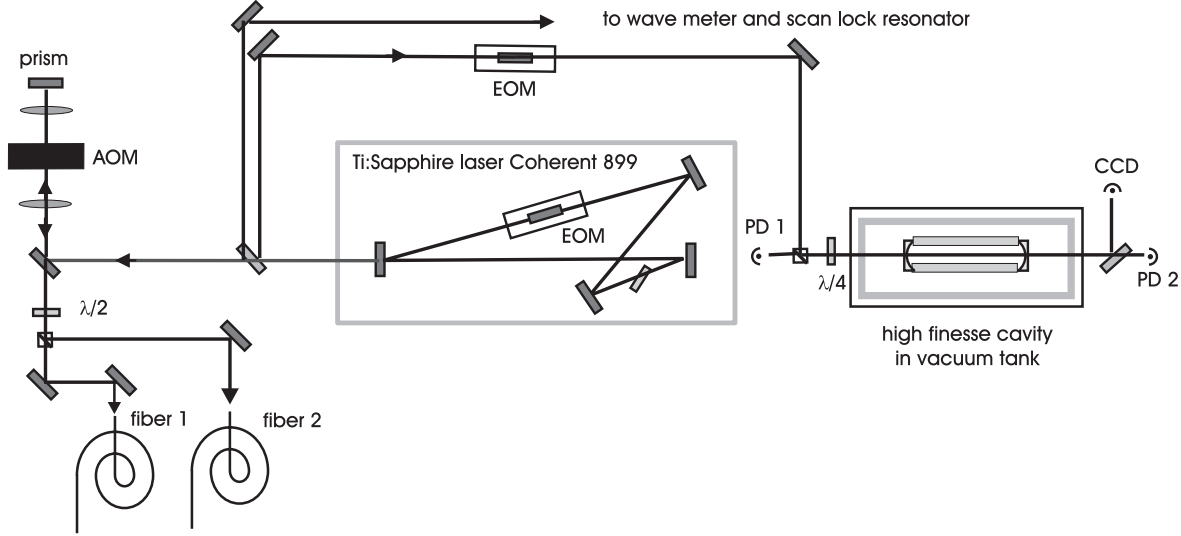


Figure 3.9: Setup for 729 nm laser. The EOM outside the Ti:Sapphire laser is the same as the one used for the laser at 794 nm. The AOM is used in double pass for fine detuning. In addition, it serves for power control and fast ON-OFF switching. The transmission through the high finesse cavity is monitored on a photodiode (PD 2) and on a CCD camera. PD 1 is used for deriving the Pound-Drever-Hall error signal.

beam is back reflected by a prism and re-enters the AOM with a slightly different angle in the other direction. Thus, the incoming and outgoing beams can be separated spatially. The outgoing beam is then sent to two different fibers. Typical transmission through these fibers is 50% to 60%. This results in up to 15 mW of power behind either of the fibers. For the purpose of frequency stabilization part of the light is coupled into a high finesse cavity (finesse $F=230000$). The demodulated signal from PD1 is sent to the tweeter piezo of the ring resonator (bandwidth 18 kHz), to the high-voltage side of an additional intracavity EOM²⁰ (bandwidth 100 kHz) and to the rf side of this EOM (bandwidth 1.5 MHz). The high finesse reference cavity is suspended in a temperature stabilized vacuum tank to isolate it from environmental perturbations which change the wavelength (vibrations, temperature). The vacuum tank is pumped to a pressure of less than 10^{-8} mbar by an ion getter pump. The spacer (length 200

¹⁸CR-899, Coherent.

¹⁹GPF-65-22.5, Brimrose.

²⁰PM 25, Gsänger.

mm) is made of an ultra low expansion material²¹ to further reduce the drift of the resonances. For stability reasons this cavity is not tunable. The highly reflecting mirrors²² are optically contacted to the spacer. The AOM used for detuning therefore has been chosen to have a high center frequency (650 MHz) with a bandwidth of 225 MHz. It is driven by a stable function generator²³. With the help of different TEM₀₀ modes spaced at FSR=750 MHz and by using the AOM in double pass in either the 1st or -1st order, the laser can be tuned to any frequency around 729 nm.

From the error signal of the closed servo loop we infer a frequency stability of better than 100 Hz with respect to the cavity. The frequency stability of the cavity is unknown. Similarly constructed cavities have shown a stability on the order of 100 Hz [60]. Spectroscopy on a single Ca⁺ ion shows that the laser stability is at least 1 kHz. Beat measurements with a comparable system have not been possible so far due to the lack thereof. The relative drift of the resonances with respect to the S_{1/2} - D_{5/2} quadrupole transition (see chapter 5) corresponds to the expected drift of the high finesse cavity due to aging (typically 15 Hz/s). One has to be careful though in attributing this drift solely to aging because presently it cannot be separated from a drift of the magnetic field which might be on the same order. There is an easy solution for separating the magnetic field drift from a drift of the reference cavity. For this, the center frequencies of two Zeeman components with different frequency offsets from the Bohr frequency (see Fig. 7.4) have to be determined by absorption spectroscopy. The Bohr frequency can then be determined with the help of the Lande factors. This measurement is then not sensitive to the magnetic field in first order.

3.2.3 Diode lasers at 850, 854, and 866 nm

There are several reasons for stabilizing the diode lasers beyond the level needed for repumping and resetting. For the laser at 866 nm it is desirable to achieve linewidths so that dark resonances are clearly resolved. With the help of these Raman resonances it is in principle possible to achieve sub-Doppler temperatures for laser-cooling. For this it is necessary to position the laser frequency at one of the steep slopes given by these resonances. This requires a linewidth of about 100 kHz or less in addition to high drift stability of the same order²⁴. A reduced linewidth for the lasers at 850 nm and at 854 nm is desirable in order to phaselock both lasers to drive a Raman transition between the D_{3/2} and the D_{5/2} levels. This possibility is briefly discussed in the appendix.

Since the diode laser systems are almost identical they will be described together. The diode laser setup is shown in Fig. 3.10. Additional details can be found in [61]. A laser diode²⁵ with maximum output power 50 mW is combined with a collimator and an external grating in Littrow configuration to create an extended tunable resonator [62, 63]. The resonator is tem-

²¹ULE, Corning.

²²PMS Electro-Optics, Boulder, USA.

²³Signal generator 2023, Marconi.

²⁴In this case drift stability mostly refers to the relative drift of the lasers at 866 nm and at 397 nm. Relative drift stability could be achieved by locking both lasers to the same cavity.

²⁵SDL 5401-G1 for laser at 866 nm.

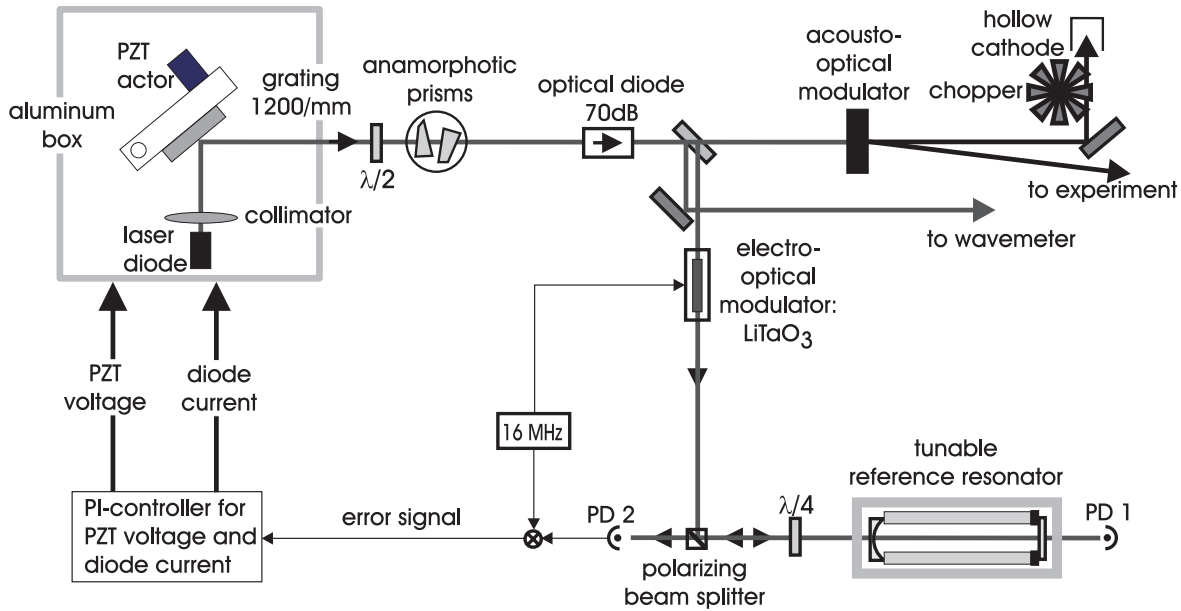


Figure 3.10: Diode laser setup. The beam from a laser diode in Littrow configuration is split into a main beam which passes an AOM and a stabilization beam which passes an EOM on the way to a reference cavity. The light which is not deflected by the AOM is used for opto-galvanic spectroscopy in a hollow cathode. The anamorphic prism pair for beam shaping is not used in all setups. Instead, a telescope is used to pass the beam through the optical diode.

perature stabilized to 5 mK (at about 5° C above room temperature) and put inside a sturdy aluminum box to isolate the setup from acoustical vibrations, temperature fluctuations, and rf stray fields. The resonator can be coarse tuned with a fine screw, and fine tuned with a piezo. This changes the angle of the grating with respect to the direction of light propagation from the diode. The feedback of the servo loop used for stabilizing the laser frequency is applied to this piezo for the slow fluctuations. Outside the aluminum box the laser beam is shone through a pair of anamorphic prisms for beam shaping and through an optical diode²⁶ (70 dB isolation) for avoiding optical feedback other than that from the grating. The diode laser is again frequency stabilized to an external reference cavity by the Pound-Drever-Hall method. One of its mirrors is mounted on a piezo so that its resonance frequency can be tuned. The linewidth of this cavity is about 750 kHz (finesse $F=1000$) to gain a steep error signal. Part of the light (after passing through the optical diode) is sent through an EOM (with a LiTaO_3 crystal) to generate sidebands at typically 16 MHz, and the reflected light from the cavity is mixed with the local oscillator at 16 MHz to produce the error signal. The fast components of the servo signal then modulate the diode current for stabilization. The current modulation is achieved with a FET circuitry inside the metal box close to the diode [61]. Also, part of the laser light is coupled into a wavemeter (Michelson interferometer type) which allows for

²⁶I-80-U4, Isowave.

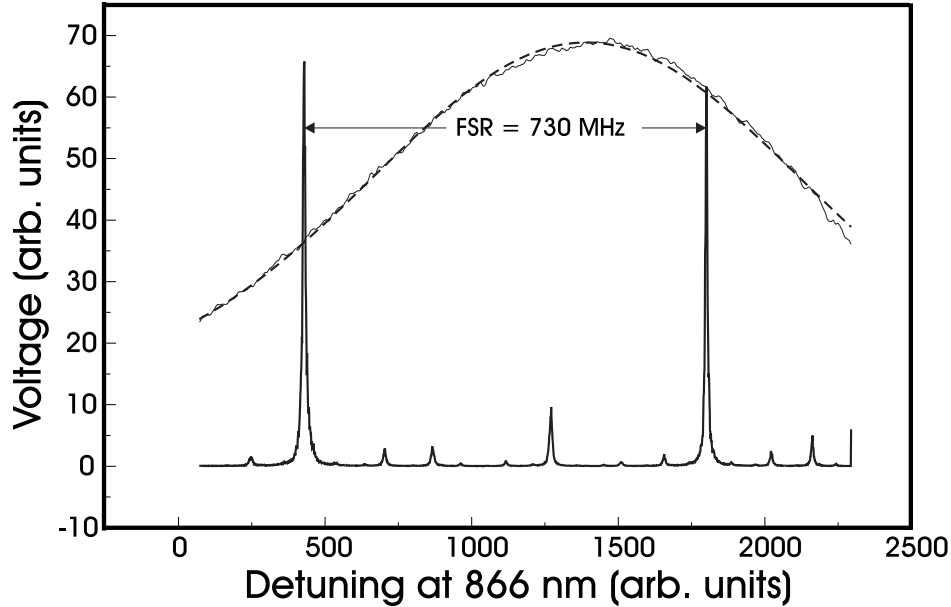


Figure 3.11: Hollow cathode spectroscopy. The Doppler broadened signal is fit with a Gaussian (FWHM = 775 MHz, corresponding to a temperature of $T=390$ K). The transmission peaks of a Fabry-Perot cavity are used as frequency markers (free spectral range FSR = 730 MHz).

monitoring the wavelength to a precision of 10^{-6} . More than 90% of the light though passes through an 80 MHz AOM for power control and fast ON-OFF switching of the laser beam. The 0^{th} order light beam enters a hollow cathode lamp for Doppler limited opto-galvanic spectroscopy in a hollow cathode [61]. A spectrum is shown in Fig. 3.11, where in addition to the Doppler broadened line the TEM₀₀ transmission peaks of a monitor cavity are plotted. These serve as frequency markers. The 1^{st} order light beam is sent towards the experiment. For the 850 nm and 854 nm diode lasers the AOM is used in double pass in order to reduce the stray light (mostly from the crystal), which is emitted in the direction of the laser beam to the experiment. Also, the AOM in double pass allows for fine tuning the laser frequency (± 20 MHz) without changing the beam direction. Typically, there are 2 to 5 mW of usable power after the beam passes the AOM which is then directed towards the experiment. The laser can be detuned with the help of the piezo mounted mirror on the cavity across a few spectral ranges (FSR = 730 MHz).

We determine the laser linewidth and its long term stability (drift) by means of beat measurements with a diode laser of the same setup. For the laser at 866 nm a second laser system was set up. For the laser at 854 nm the laser at 850 nm was tuned to this wavelength. In general, the measurements show a beat linewidth of less than 200 kHz [61]. Recent improvements on the electronics have resulted in beat linewidths of about 20 kHz. Locking the lasers to the same cavity yields beat widths of about 1 kHz. For the drift measurements we have either

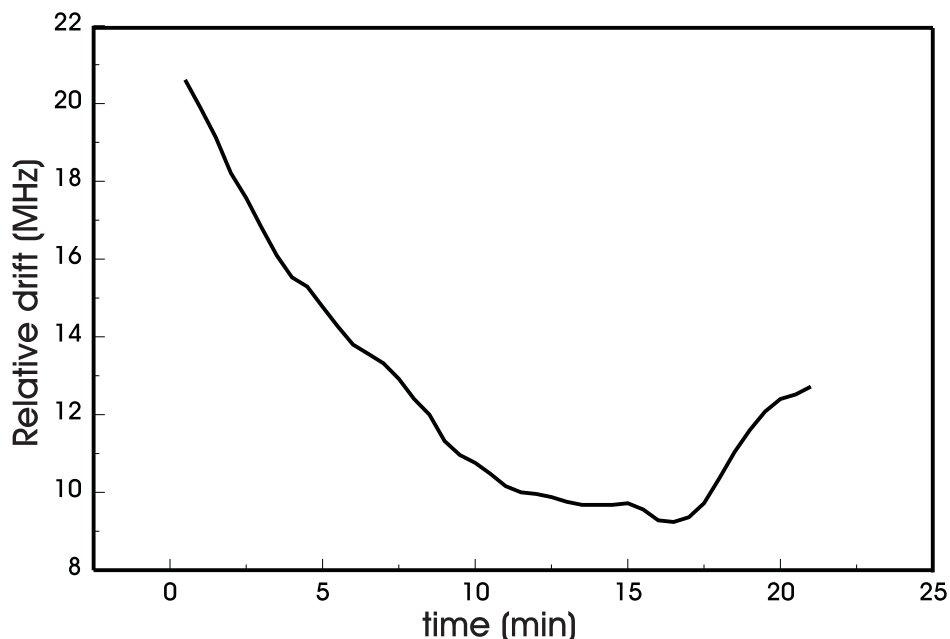


Figure 3.12: Relative drift of two identical and independent diode lasers at 866 nm. The center of a beat signal was recorded every 30 s for more than 20 min.

used two lasers locked to independent cavities (one cavity fixed without piezo and the other one detunable) or two lasers locked to the same cavity. In the first case, the drift is dominated by the relaxation of the piezo and can be as much as 20 MHz/30 min. This can be seen in Fig. 3.12, where the center of a beat signal near dc was tracked for about 20 min. This drift can be reduced if one does not apply changing high voltages to the piezo. Unfortunately, this is almost impossible during the loading of the trap when one tries to optimize laser parameters. We have observed comparable drift rates for the lasers at 794 nm and 729 nm when these are locked to similar cavities with piezo-mounted mirrors. In the second case, when two lasers are locked to the same cavity, the drift is comparatively small (less than 10 kHz/min) and can be attributed to changes of the lock point of the electronics.

The drift of all lasers currently poses a considerable problem. In particular for high resolution spectroscopy on the $S_{1/2} - D_{5/2}$ quadrupole transition the drift due to aging of the high finesse cavity spacer for the laser at 729 nm cannot be avoided. In this case it is necessary to know the current drift rate and to adjust the laser accordingly. The drift due to piezo relaxation on reference cavities of the dipole lasers can be reduced by either using a drift lock as described above or by refraining from the use of such piezos. For example, the tunable reference cavity for the laser at 866 nm is currently being replaced by a cavity without piezo. The laser will then be detuned by a broadband AOM similar to the setup used for the laser at 729 nm. Alternatively, one could use a transfer cavity which is locked to Cesium near 852 nm by saturation spectroscopy.

4 Ion Storage

This and the following chapter present the experimental results achieved with the linear trap so far. The first part of this chapter will discuss the trapping of a single or a few ions and our ability to control trap parameters. This control is a major prerequisite for our goal to achieve coherent dynamics in the trap, i. e. to entangle the internal and external (vibrational) degrees of freedom of a string of ions. After this it will be shown that compensation of micromotion is possible with the help of a correlation technique. Finally, the results on the radio-frequency excitation of center-of-mass and of the breathing mode will be presented. With the help of a gateable CCD camera we have recorded movies of oscillating ions in the trap. The next chapter then presents the results concerning spectroscopy on a single or a few ions. The aim of the spectroscopic experiments is to acquire the ability to determine the ions' quantum state (i. e. for the electronic and the vibrational degrees of freedom) and to use this information to manipulate and control the ions' coherent dynamics. Ultimately, as mentioned before, the goal will be to trap a string of ions, to prepare this string in a well defined quantum state, to address each ion individually with a laser beam for coherent dynamics, and to finally read out the (quantum mechanical) information from each ion separately.

4.1 Trap operation

4.1.1 Loading process

A typical experimental run starts with loading a relatively large cloud of ions (diameter of the cloud is larger than $200\ \mu\text{m}$, estimated number of ions 100-1000) with the help of the Ca oven and the electron gun. This is facilitated by turning off the vacuum pump so that background gas buffer cooling assists in trapping and cooling the cloud. We then adjust the lasers at 397 nm and 866 nm in such a way that they are directed onto the center of the trap. They are focused to a spot size of approx. $100\ \mu\text{m}$ in diameter from the directions $(x, y, z) = (0, 1, \Leftrightarrow 1)$ and $(x, y, z) = (\Leftrightarrow 1, 0, \Leftrightarrow 1)$ as shown in Fig. 3.3. The trap center does not change much on a day to day basis (less than $\pm 50\ \mu\text{m}$ in the axial direction and less than $\pm 5\ \mu\text{m}$ in the radial direction) and is known from previous CCD pictures of crystallized ions. If the trap center does not agree with previous measurements we usually change the dc voltages on the ring electrodes used for axial confinement to move the center back to its former position. The observed deviations correspond to the deviations which occur from load to load which we attribute to slightly changing stray fields. PMT and CCD need to be adjusted only once for maximum fluorescence intensities. The ion-cloud then allows us to choose the correct laser detunings. Then there are two possibilities to store single or few ions: Either we turn on the vacuum pump, empty the trap (by briefly turning off the rf drive field), and then try to

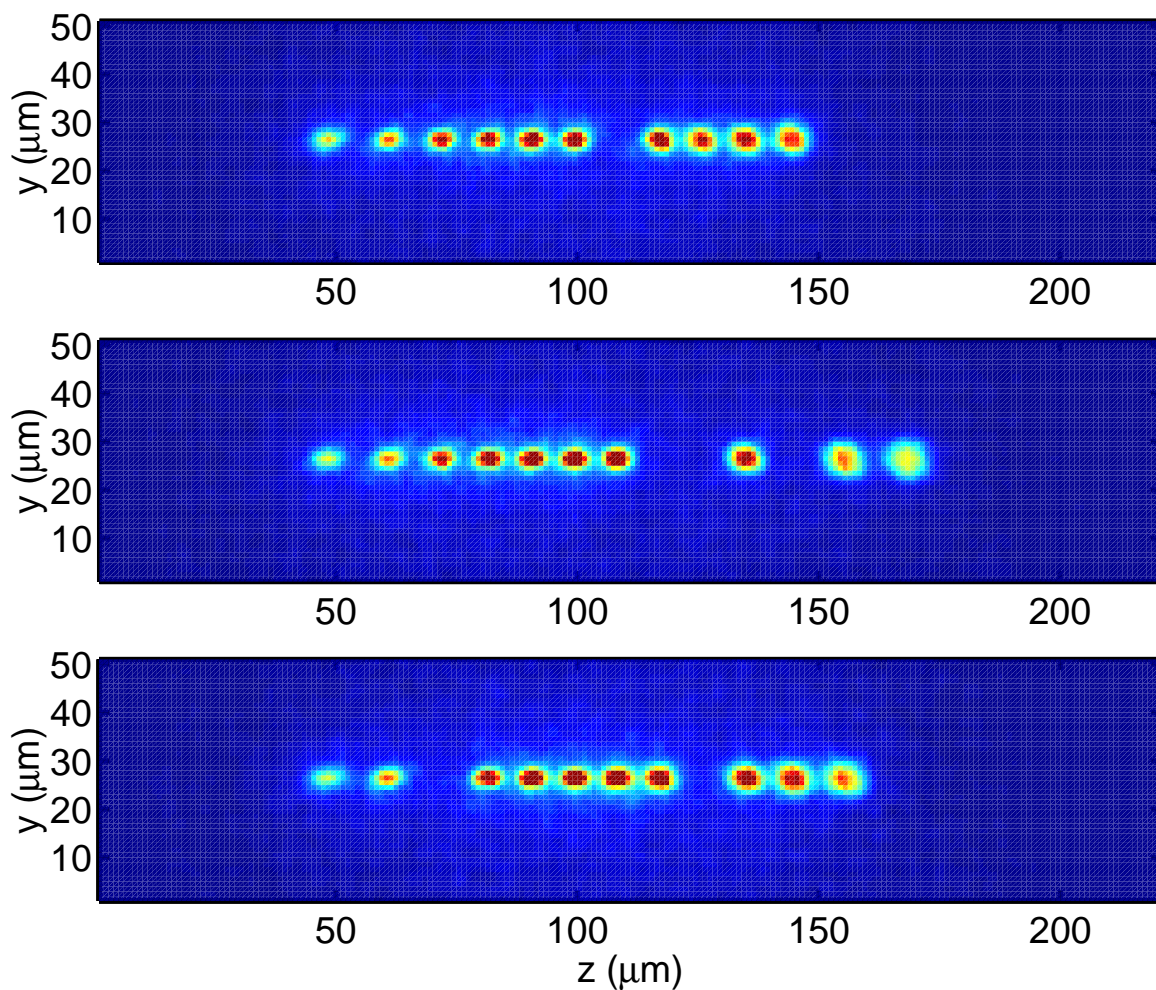


Figure 4.1: String of 10 ions plus 3 impurity ions as seen with the intensified CCD camera. In the top image one impurity ion is in the center, the other two are at the far right. The average inter-ion spacing is approx. $10\ \mu\text{m}$ for axial oscillation frequency $\nu_z = 108\ \text{kHz}$. The radial frequency is $\nu_r = 1.4\ \text{MHz}$. Exposure time is 1 s. The outer left ion shows less fluorescence because it is slightly out of focus. The ions on the far right are also slightly out of focus. The direction of observation is at an angle of 67.5° with respect to the trap axis.

load directly from the atomic beam by pulsing the electron gun. Or we turn off the oven and electron gun and then turn on the vacuum pump. In the latter case, we generally end up with a smaller cloud havin a reduced ion number. This ion number then needs to be further reduced until only a few ions are left which have a chance to crystallize. The most successful and also most simple way to reduce the number of ions in the cloud is to block the laser at 866 nm for times between a few seconds and half a minute. Turning off the lasers leads to

a loss of ions because of the lack of laser cooling. While making the cloud smaller the laser detunings need to be adjusted because a smaller cloud leads to narrower lines in the excitation spectrum. Also, the laser power can be reduced because of the improved spectral overlap for colder ions. We usually repeat the blocking and unblocking of the lasers a few times. At the end of this iteration we end up with a crystallized string of ions.

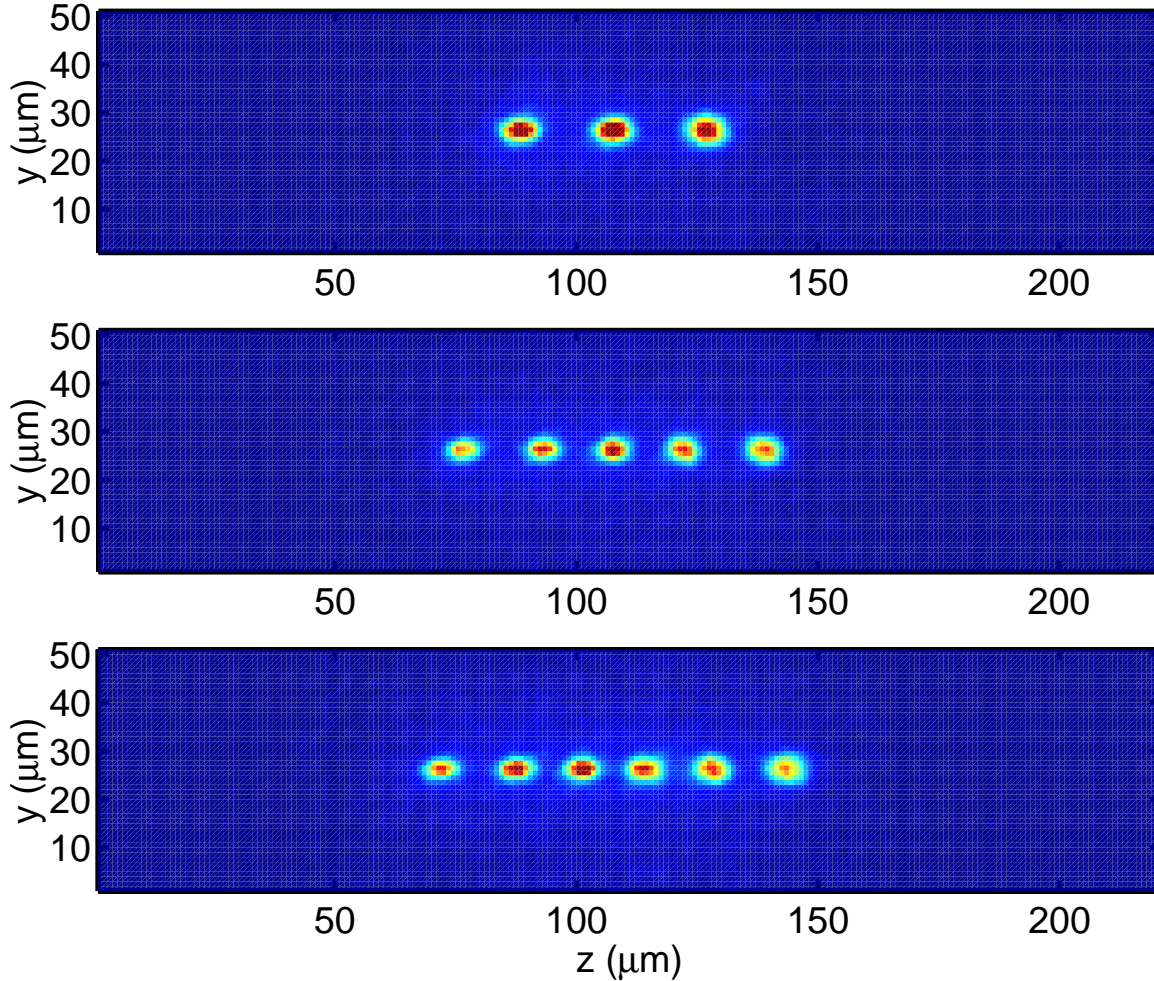


Figure 4.2: Examples of ion strings. Same parameters as in Fig. 4.1.

One problem with the current loading process is the fact that we trap a high percentage of impurity ions. These ions show up as non-fluorescing lattice sites in the crystal. This can be seen Fig. 4.1. Sometimes we trap about 15 ions, but only 3 of these are Ca^+ ions. The proportion of impurity ions in our sample has steadily increased over the last $1\frac{1}{2}$ years from about 5% to an average of about 50% today. We attribute this increase to a degradation of our Ca oven whose flux is noticeably reduced. On the other hand, we have developed a technique which is quite successful in purifying our sample. We usually block the laser at 866

nm while we detune the laser at 397 nm more than 2 GHz to the red side. After unblocking the laser at 866 nm we slowly sweep in the frequency of the 397 nm laser. We seem to have found the right balance of laser cooling for the 'good' ions and the 'bad' ions, which are only cooled sympathetically. There is one piece of information the impurity ions give us which cannot be acquired easily by other means. This is the rate at which the ions switch positions in the string. Typically, the ions switch positions on the time scale of 1 second. This rate though depends strongly on the percentage of impurity ions and on the parameters for laser cooling.

So far we do not know what kind of impurity ion we trap together with the Ca^+ ions. One possibility to find out is to trap two ions, one Ca^+ ion and one impurity ion, and to measure the axial or radial oscillation frequency for the center-of-mass mode. With the help of e. g. Eq. (2.2) this could then be compared with the frequency of a single Ca^+ ion to derive the mass of the unknown ion.

4.1.2 Linear, zigzag, and large ion crystals

We trap linear ion strings for any number between 1 and about 15, depending on the ratio between the radial and axial trap frequencies. Examples of this are shown in Fig. 4.2. With some patience it is possible to reduce a load of e. g. 10 ions one by one so that one is able to do experiments with a varying number of ions while all other parameters are kept constant (a new load would require a slight change in micromotion compensation parameters and thus slightly change in trap frequencies etc.). Fig. 4.3 shows the photon counts recorded by the PMT as a function of time for 4 ions. Weak light at 729 nm was used to induce quantum jumps. One can clearly discriminate between the different discrete levels of fluorescence. Fig. 4.4 shows the ions' position as a function of the number of trapped ions. A numerical calculation of the ion equilibrium positions by minimizing the potential in Eq. (2.6) agrees reasonably well with the measured positions. The largest error is given by the fact that different loads have been used for this comparison. The ring voltages differed from load to load by up to 5%. As mentioned before, such a measurement could be significantly improved if a single load could be used while the ion number is reduced one by one.

Fig. 4.5 shows the transition from linear crystals to zigzag crystals for a given axial frequency as a function of the radial frequency and of the number of ions in the trap. For this plot Eq. (2.7) was used. For high radial frequencies and low ion numbers the ions form linear strings, whereas either increasing the number of ions or decreasing the radial frequency leads to planar zigzag structures (see Fig. 4.6). Typically, we work in the upper left hand corner of the diagram (axial frequency 1.4 MHz, number of ions 1 to 10). Fig. 4.6 corresponds to a point in the upper right hand corner. Ions in zigzag configuration have the tendency to spontaneously switch to the mirror configuration (similar to the spontaneous switch in position for impurity ions). Both configurations seem to be local minima of similar energy for the potential at hand.

For even higher ion numbers the crystals become three-dimensional. As can be seen in Fig. 4.7 the ions in the center part arrange two by two with an angle of 90° between each pair. One limitation in trapping larger ion crystals than the one shown in Fig. 4.7 is the size of the waist

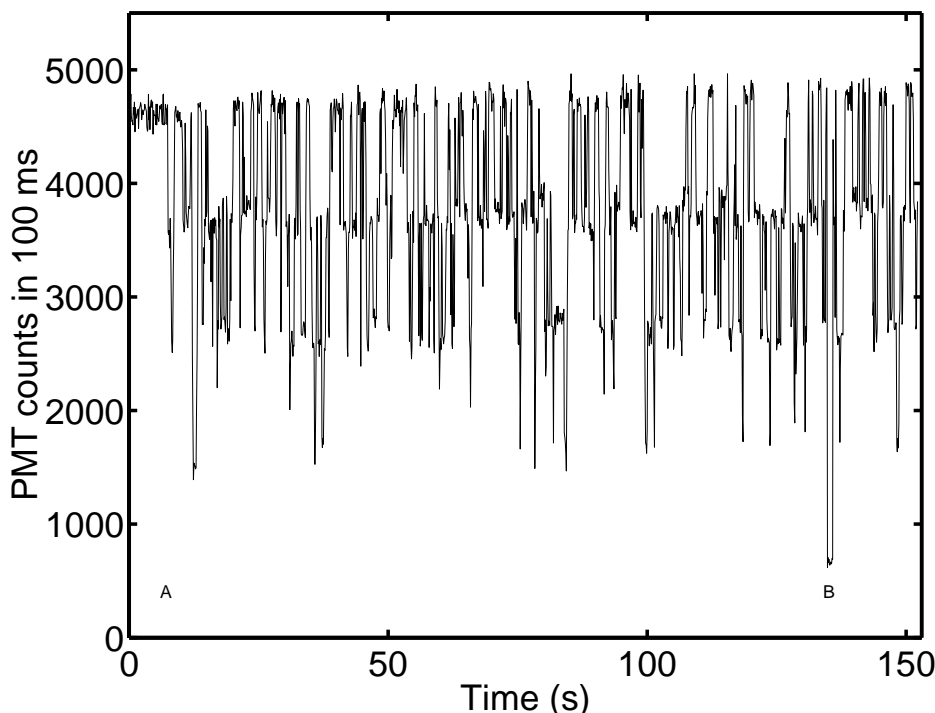


Figure 4.3: Quantum jumps with 4 ions. At time A, the laser at 729 nm was turned on with low power to induce the jumps. At time B, the repumper laser at 866 nm was briefly turned off to show the background level. During the time it took to record this trace it never happened that all 4 ions were off.

of the laser beams at the position of the ions used for cooling. Another limitation is the fact that we currently trap too many impurity ions which do not contribute to the laser cooling rate.

4.1.3 Compensation of micromotion

We think that a slight geometrical misalignment of the trap ring electrodes (their center is somewhat off axis) is mostly responsible for dc bias fields at the ions' position. These and other stray bias fields need to be compensated for with the help of two pairs of compensation electrodes parallel to the quadrupole electrodes. Otherwise, as shown in Eq. 2.4, these dc fields lead to extra micromotion. This extra micromotion results in higher ion temperature and cannot be reduced by laser-cooling because it is a driven motion. On a day to day basis the necessary fields for compensation do not vary much (less than 5%). Seemingly, there are no major time varying patch effects which might change after each loading. Micromotion compensation can be done crudely by observing the ions' position on the CCD camera while varying the dynamic trap potential, or in a more refined way by using a correlation measurement between the arrival of photons at the PMT and the phase of the rf field. The setup for

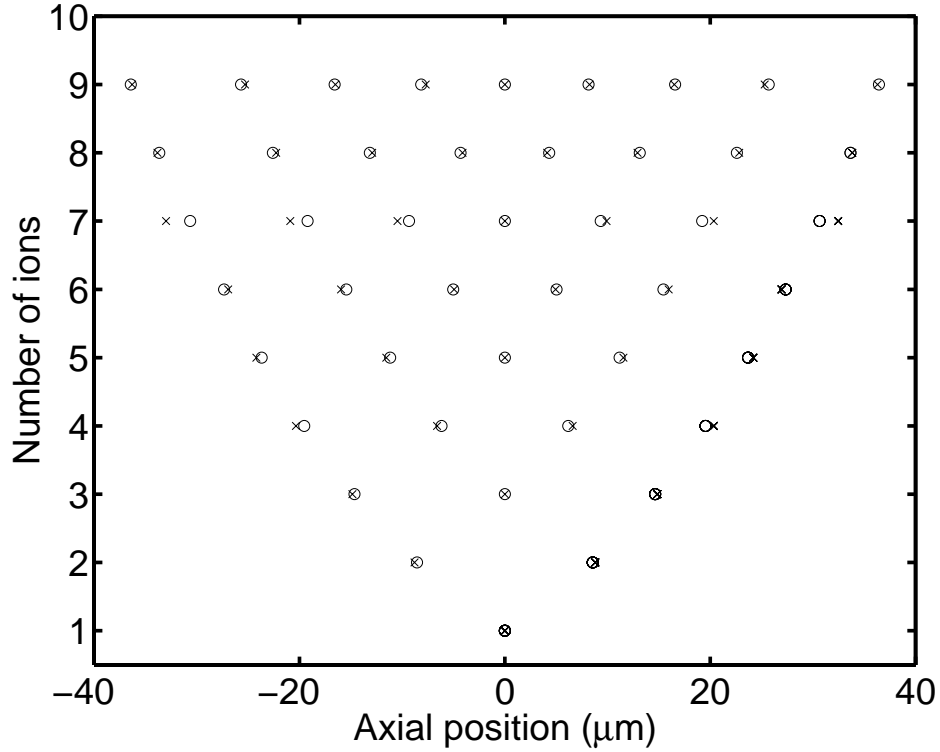


Figure 4.4: Ion position as a function of ion number. Experimental data is shown as 'x', the numerical calculation according to Equ. (2.6) is shown as 'o' for $\nu_z = 187$ kHz. Different loads have been used for this plot. This accounts for different axial trap frequencies and thus different ion spacing. In particular, for the data set with 7 ions the axial trap frequency was approx. 5% less than for the other data sets.

this correlation measurement is shown in Fig. 4.8. In the first case one monitors the direction of the shift in position while increasing or decreasing the steepness of the radial potential. For an increase of the radial potential the direction of the shift points towards the center of the rf pseudo potential. Consequently, the ions can be shifted with the help of the dc bias field to achieve a better overlap of ions' position with this center. Certainly, this method is limited by the resolution of the imaging optics (3 to 5 μm depending on whether the mirror for coupling in the light at 729 nm along the direction of the CCD camera is used). In our trap where the angles of the trap directions with the direction of CCD observation are different from 90° , we can use this technique for rough compensation in all 3 dimensions. This we have done once. From experimental run to experimental run we now use the correlation measurement. This measurement relies on the Doppler effect due to the driven motion of the ions at 18 MHz [29]. Ions oscillating at this frequency scatter light at preferably one phase of the oscillation period, given by the detuning of the laser. The arrival time of scattered photons is thus sensitive to the oscillatory motion. For this reason a photon count triggers a multichannel

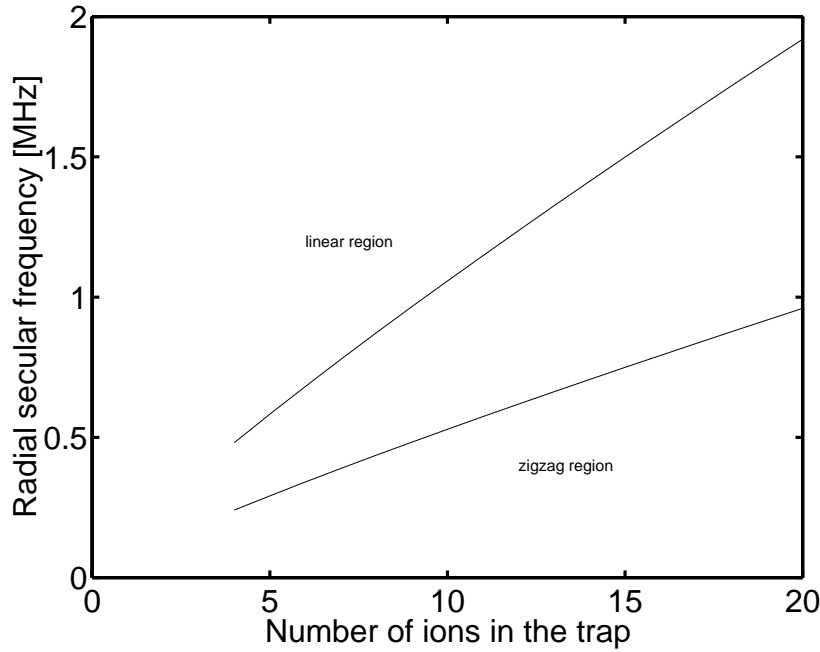


Figure 4.5: Change from linear to zigzag ion crystals for fixed axial oscillation frequency according to Equ. (2.7). Upper curve: $\nu_z = 200$ kHz. Lower curve: $\nu_z = 100$ kHz. Above the curves the ions form linear strings, below the curves they form zigzag structures.

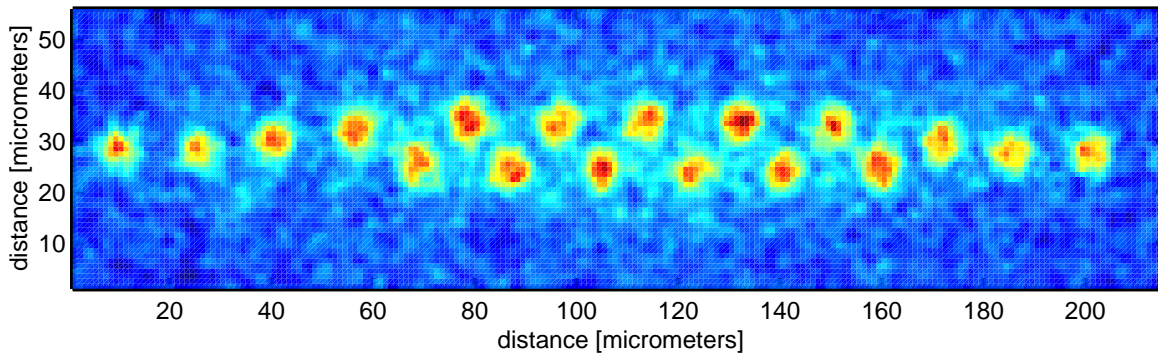


Figure 4.6: 19 ions in zigzag configuration. One impurity ion does not fluoresce (located at approx. $50 \mu\text{m}$ in the horizontal direction). The radial oscillation frequency is $\nu_r = 1.4$ MHz, the axial oscillation frequency is $\nu_z = 200$ kHz.

scaler (MCS)¹ whose input is given by pulses synchronized to the ac drive frequency. For optimum results the ions are illuminated at 397 nm in only one direction. The other direction

¹SR400, Stanford Research Systems.

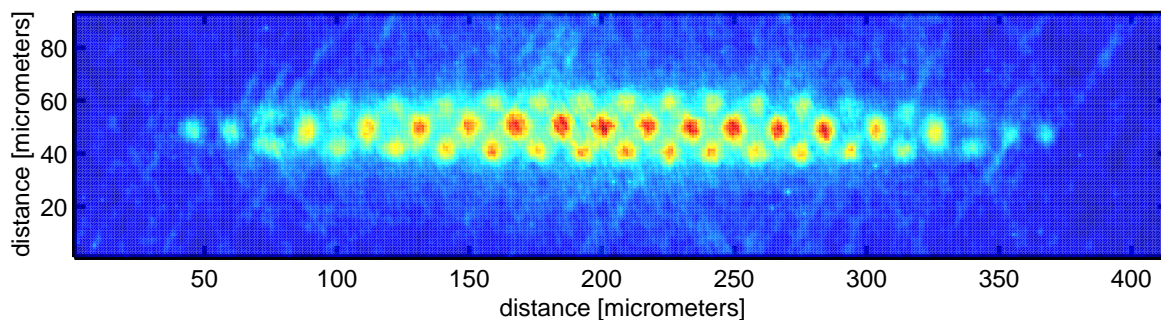


Figure 4.7: A cigar shaped crystal with 62 ions.

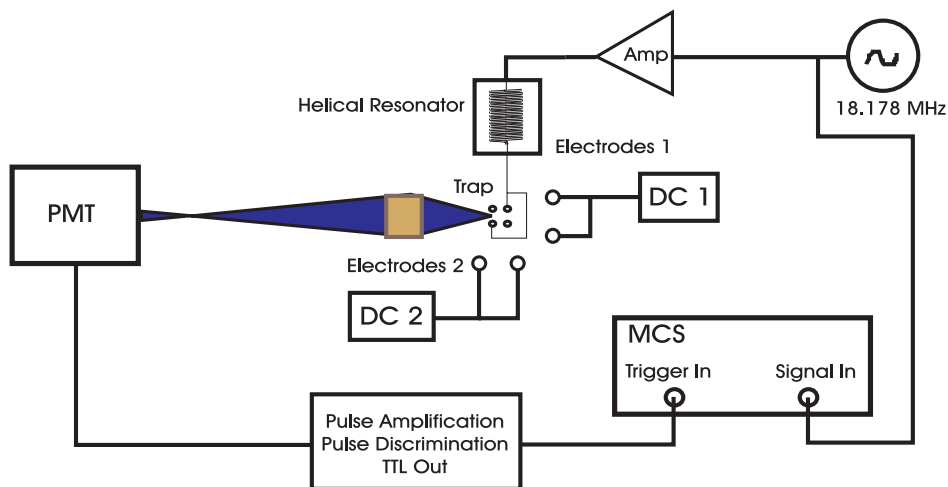


Figure 4.8: Setup for compensation of micromotion. A photon count provides the trigger for multichannel scaler (MCS), the rf drive field at 18 MHz provides the signal to be recorded. The compensation electrodes 1 and 2 are parallel to the trap quadrupole electrodes. Voltages at dc are applied to these electrodes to shift the ions to the trap center.

is blocked because the signal from two directions can be composed of two components with a 180° phase shift which then cancel in the correlation signal. Also, the laser detuning is set to the point of the steepest gradient of the fluorescence curve. At this point laser-cooling should be at its optimum and the correlation signal at its maximum. Fig. 4.9 shows typical experimental scans of the MCS for the $(\leftrightarrow 1, 0, \leftrightarrow 1)$ direction in the trap. A scan consists of 20000 records each given by a single photon count. It usually takes a few seconds to build up a scan. For the top left scan the compensation voltages have been detuned to show an increased correlation signal. On the right the power spectrum is shown which exhibits prominent peaks at the drive frequency and its second harmonic. In the middle the correlation signal is shown after compensation. As can be seen on the right the power at the drive frequency has been

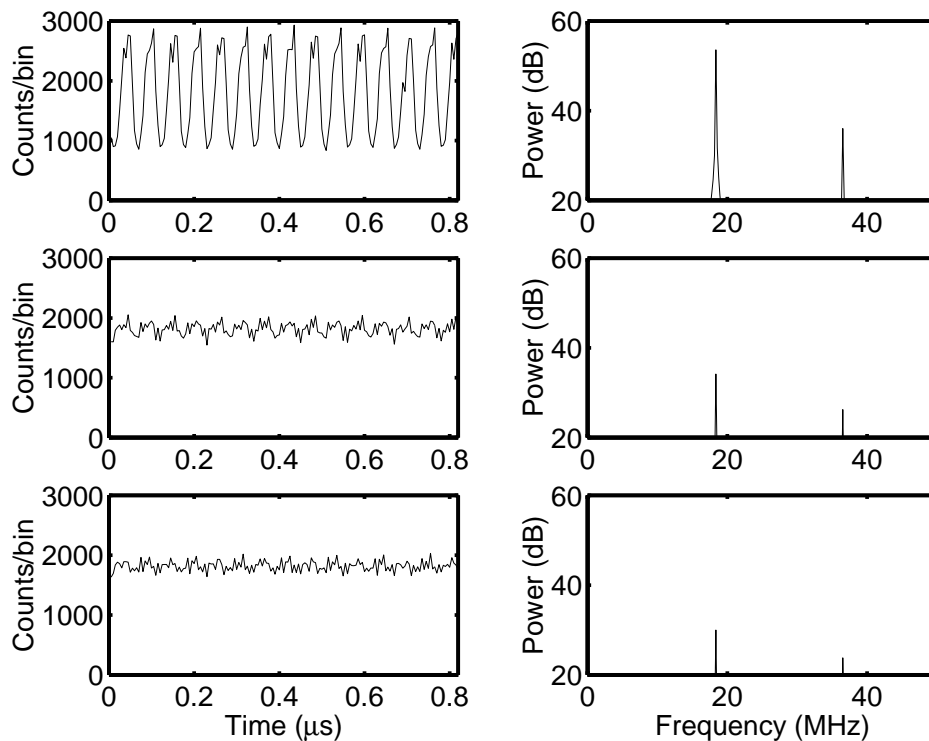


Figure 4.9: Compensation of micromotion for 3 ions. On the left the experimental fluorescence correlation signal is shown, on the right its power spectrum. Top: Partial compensation. Middle: Final compensation. The power at 18 MHz is suppressed by 20 dB. Bottom: Correlation signal without ions. Trigger photons are given by stray light.

reduced by approx. 20 dB with respect to the upper plot. The bottom plots show that some residual correlation signal is present even without ions. The trigger photons are given by stray light photons. This residual correlation is caused by cross-talk in the MCS which we have so far not been able to reduce². Typically, we compensate in one direction, then in the other direction, and so on until after a few steps of iteration the correlation is reduced to about the level shown in the middle plot of Fig. 4.9. Presently, the residual correlation does not seem to limit high resolution spectroscopy on the $S_{1/2}$ to $D_{5/2}$ quadrupole transition. Ultimately, the success of the correlation technique can be measured with the help of sideband spectroscopy on this transition. Here, the amount of residual micromotion can be measured by recording the height of micromotion sidebands. Sideband spectra could then be used to further reduce micromotion.

²Note that the bottom scan takes about 5 times longer to record than the upper scans because the photon count rate for stray light is 5 times lower than for fluorescence photons. Assuming that the cross-talk is proportional to the time for recording, the amount of cross-talk in the upper plots is thus reduced accordingly.

We currently need to apply voltages of more than 700 V to the compensation electrodes. Increasing the voltages on the ring electrodes requires higher compensation voltages. Therefore, as mentioned before, we attribute most of the necessary compensation to an imperfect geometrical alignment of the ring electrodes with respect to the trap axis. Since higher compensation voltages are not possible with the current setup we are limited to ring voltages of about 160 V. The corresponding axial trap frequency is $\nu_z \simeq 140$ kHz. Higher axial frequencies are only possible at the expense of imperfect micromotion compensation. In the near future we will therefore replace the current electrode configuration by a new one whose geometry is better defined. A description of the new configuration is given in the appendix.

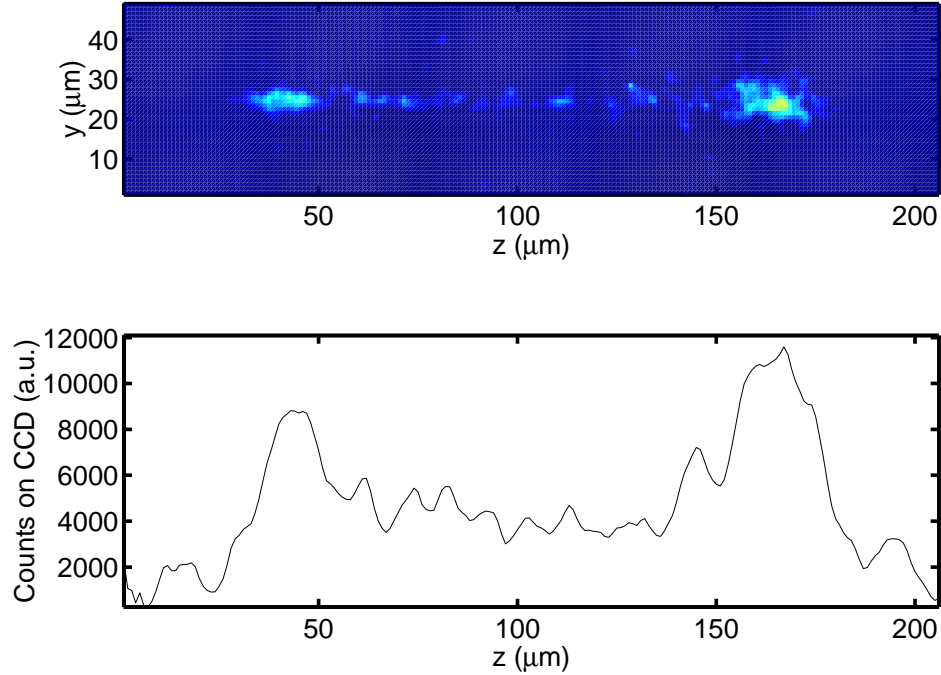


Figure 4.10: Top: Axial orbit of a single ion. Bottom: Counts on CCD integrated along the vertical direction. One can see the classical turning points of the ion's motion. The image is not uniform because trap axis and direction of observation are at an angle of 67.5° . At the turning points the ion is already out of focus (compare with Fig. 4.1).

4.2 Normal mode oscillation

In the following section the motion of the ions as it can be observed with the CCD camera will be discussed. First, examples of the motion when laser beam geometry and/or laser detuning result in extended ion motion in the trap will be shown. Then, the results will be presented when we deliberately excited the ions' motion by applying radio-frequency fields to some of the electrodes near to the ions at frequencies close to the secular oscillation frequencies. In

particular, I will discuss the results for the motion along the axial direction in the trap since the oscillatory motion in this direction is essential for the use of stored ions for quantum computation.

4.2.1 Ion orbits

When either the laser at 397 nm or the repumping laser at 866 nm is tuned to the blue side of the transition, the ions heat up and produce pictures smeared out on the CCD camera. Because of the shape of the trapping potential a higher temperature leads to a preferred motion along the trap longitudinal axis. This can be seen in Fig. 4.10 where the orbit of a single ion measures more than 120 μm . These orbits can be stable for many minutes, but they sensitively depend on the laser parameters which determine the laser cooling rate. When we block the 397 nm beam in the $(x, y, z) = (0, 1, \Leftrightarrow 1)$ direction there is no component

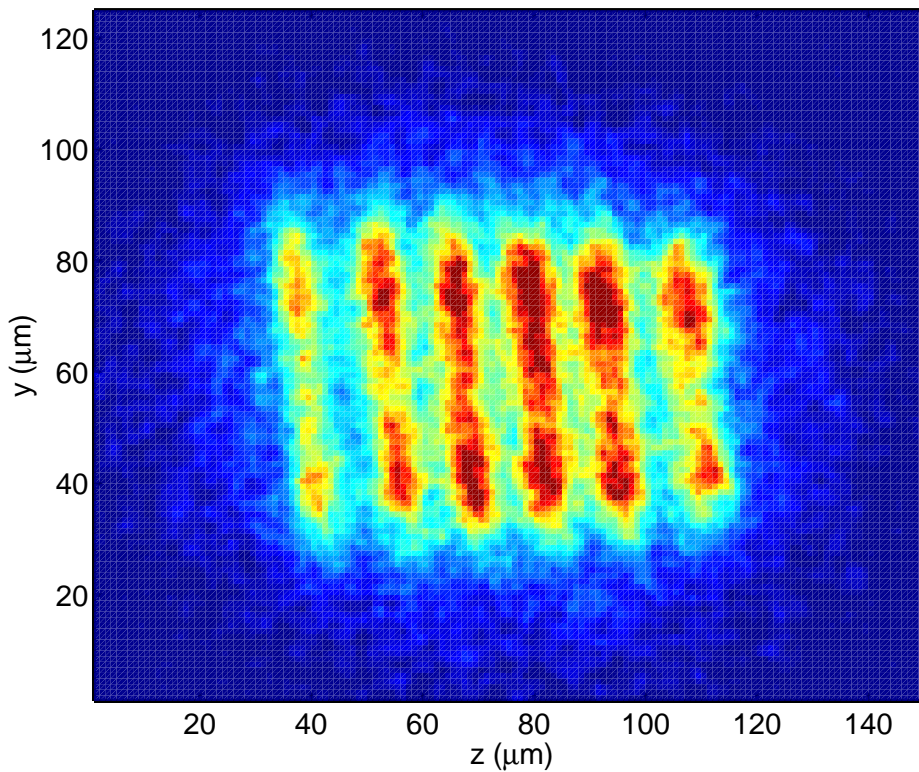


Figure 4.11: Transversal orbit of 6 ions. The 397 nm laser in the $(x, y, z,) = (0, 1, \Leftrightarrow 1)$ direction is blocked to prevent laser-cooling in the y direction. The ions are irradiated only along $(x, y, z,) = (\Leftrightarrow 1, 0, \Leftrightarrow 1)$.

of the 397 nm laser along the y-axis. The lack of laser cooling in this direction allows the ions to move transversally (as can be seen in Fig. 4.11), while the other directions are still laser cooled. Seemingly, there is only a weak coupling between the different directions in the trap because it is possible that the ions are very hot in one direction but still crystallized

in the other directions. In general, it is important to know whether it is possible cool the ions to low temperatures in the axial direction while they are still relatively hot in the radial directions. For this, we need to measure the coupling between the different directions. Further quantitative analysis here is only possible if one is able to measure the ions' temperature in all directions. This can be done by recording sideband spectra.

4.2.2 Normal mode excitation

We can excite the normal modes of the ions' motion in the trap by applying additional ac voltages at the expected oscillation frequencies to either the ring or the compensation electrodes, or to the aperture of the Ca oven. For what follows, we have used either the

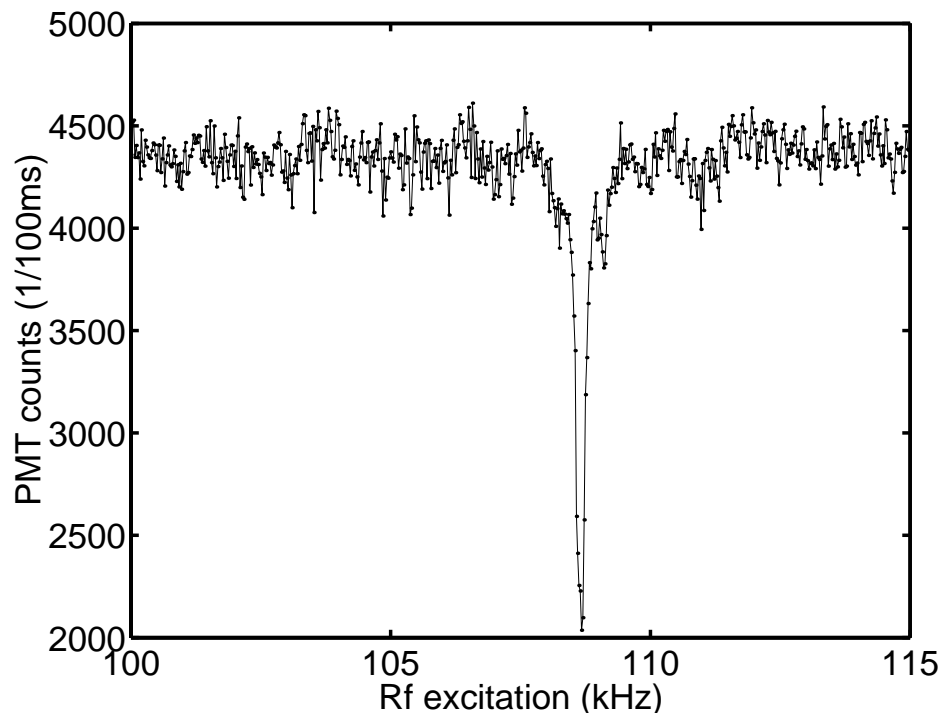


Figure 4.12: PMT counts for radio-frequency excitation of the axial CM mode for 5 ions. Center: 108.66 kHz. Width: 240 Hz. The slow variations of the PMT counts are mostly due to laser intensity fluctuations at 397 nm.

compensation electrodes or the oven aperture. This aperture has proven to be very valuable because it does not possess any radio-frequency filters which are meant to block the rf from leaving the trap chamber, but which also make it more difficult to apply any rf to those electrodes. It is important to note that with the relatively high laser power which we have used (typically much above saturation) the normal mode excitation can be seen on the CCD camera long before there is a dip in the fluorescence collected by the PMT. This agrees with the observation that the counts (integrated over the whole picture) on the CCD camera stay constant for small excitation. For the breathing mode we have not been able to see a reduction

of the fluorescence counts on the PMT. We attribute this to the fact that our dipole lasers were not sensitive enough to the ions' motion because of power broadening. Fig. 4.12 shows a radio-frequency excitation spectrum of the center-of-mass (CM) mode along the axial trap direction for 5 ions at 108.66 kHz. The fluorescence was recorded with the PMT. On resonance with the trap frequency ν_z the ions heat up along the trap axis and are thus Doppler shifted away from their optical resonance. Fig. 4.13 shows a CCD images of 3 and 5 ions when

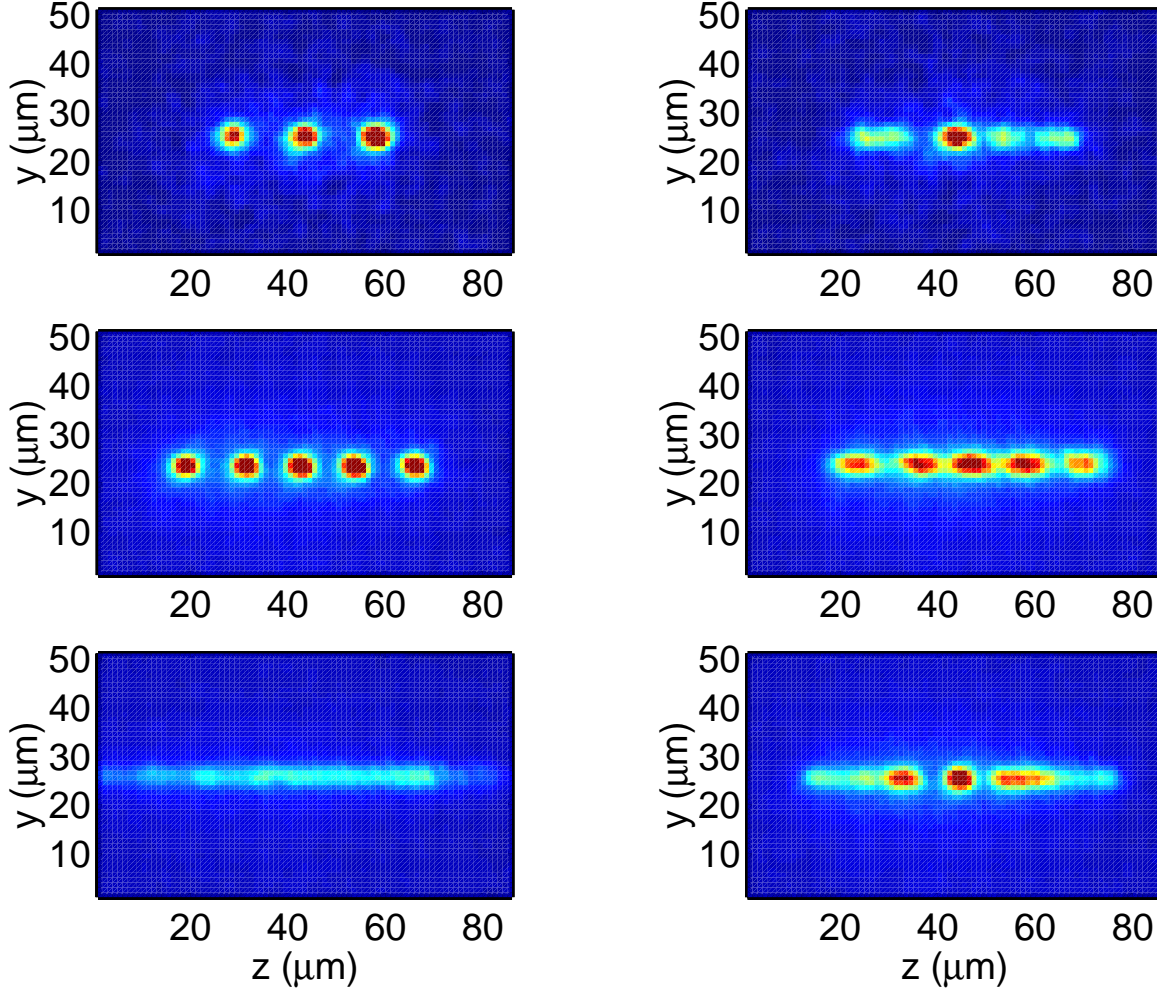


Figure 4.13: Top left: 3 ions, no excitation. Top right: 3 ions excited on the breathing mode (278.4 kHz). Middle left: 5 ions, no excitation. Middle right: 5 ions weakly excited on the CM mode (158.5 kHz). Bottom left: 5 ions strongly excited on the CM mode. Bottom right: 5 ions excited on the breathing mode (276 kHz). The exposure time for all images is 1 second.

these are excited on the CM mode or the the breathing mode in the axial direction. In order to excite the breathing mode we need to apply voltages which are typically about 300 times

higher than the ones needed for excitation of the CM mode. This can be attributed to the fact that the radio-frequency field is nearly spatially constant across the ions so that the higher modes which need field gradients across the ions are not very well excited³. When exciting the breathing mode the necessary voltages are so high that the CM mode is also excited. To some extent this can be seen in the top right and bottom right images of Fig. 4.13. The ions

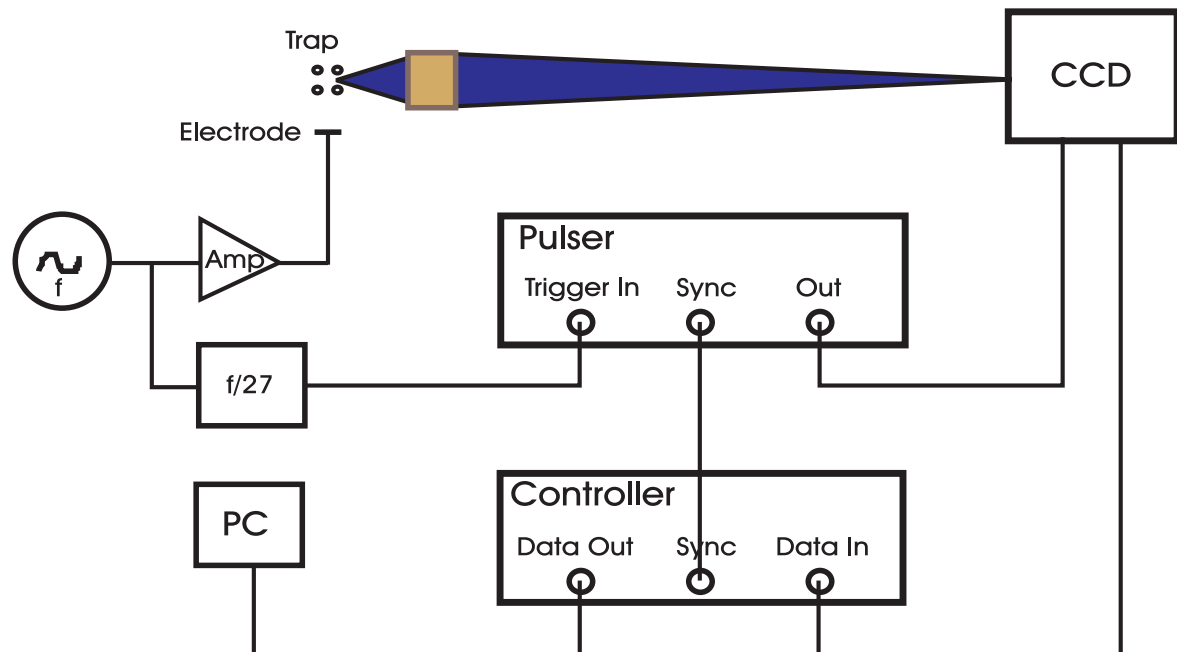


Figure 4.14: Setup for recording a movie of the normal mode oscillation. The ions' motion is excited by applying a sinusoidal voltage to one of the electrodes nearby. The CCD camera is gated for 250 ns in phase with this excitation with the help of a high voltage pulser applied to the multichannel plate. At a fixed phase 420000 exposures are integrated to yield one frame of the movie. The total integration time is given by the controller which also reads out the CCD camera and transfers the data to a PC.

on the right of the center, in addition to their motion according to the breathing mode, move in phase with the CM motion, and the ions on the left of the center are 180° out of phase. Thus the orbit of the ions on the right appears to be larger than the orbit of the ions on the left. This superposition of both modes can be seen more clearly in Fig. 4.15, which shows the individual frames of a movie of oscillating ions. The recording of a movie will be discussed below. When trying to excite modes higher than the breathing mode, the residual CM mode excitation becomes so dominant that higher modes could not be discriminated. Instead of exciting higher modes the CM mode and its harmonics are excited. We have found that the amplitude of the excitation depends sensitively on the laser detunings (i. e. at 397 nm and

³The heating rate for the breathing mode might thus be significantly reduced with respect to the CM mode. This mode might therefore be more suitable for the use as a quantum bus as discussed in Sect. 2.4.

866 nm) which determine the laser cooling rate. Also, as we tune across the normal mode resonance we have seen prominent hysteresis effects. This we also attribute to the damping mechanism due to laser cooling which in turn depends on the motion of the ions.

The setup used for recording a movie of the oscillating ions is shown in Fig. 4.14. For this, the multichannel plate of the CCD camera is gated in phase with the rf excitation. Unfortunately, the pulser needed for applying a well defined high voltage to the multichannel plate only allows a pulse repetition rate of up to 8 kHz. Therefore, some subharmonic of the excitation frequency below and near to 8 kHz is used to trigger the pulser. Typically, a movie spanning one period of oscillation consists of about 10 to 20 frames. For each of these frames the CCD camera is gated 420000 times for 250 ns corresponding to an overall exposure time of 105 ms. The time between two frames is 500 ns. In order to avoid too much thermal noise on the CCD camera while collecting data the CCD chip is cooled by a Peltier element. Fig. 4.15 shows the individual frames of a movie taken of the CM and the breathing mode for 7 ions. As mentioned before, for the breathing mode residual excitation of the CM mode can be observed. Movies of 3, 4, and 7 ions oscillating in the CM mode or in the breathing mode can be seen in [64] and on the web page [66].

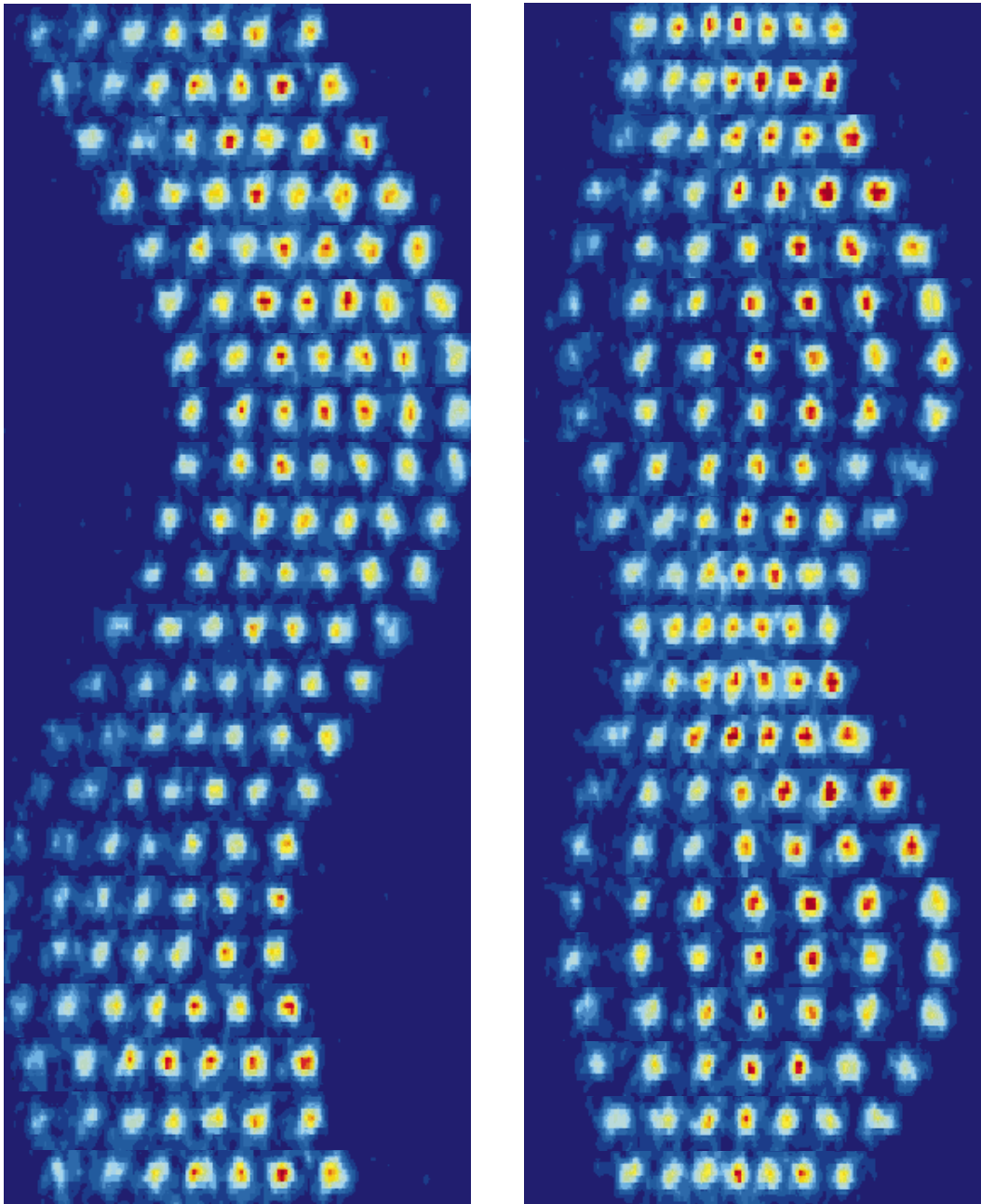


Figure 4.15: Left: CM mode for 7 ions. Excitation frequency $\nu = 106$ kHz. Right: Breathing mode for 7 ions. Excitation frequency $\nu = 184$ kHz. Note that the center ion is not stationary. To some extent the CM mode is also excited.

5 Spectroscopy

This chapter presents the results of the spectroscopic measurements on a single or a few trapped ions. First I will discuss excitation spectra on the 397 nm and 866 nm dipole transitions (see Fig. 7.2). These are all continuous wave spectra, i. e. excitation and fluorescence detection are done at the same time while slowly sweeping one of the laser detunings across resonance. The most intriguing feature of these spectra are dark resonances which appear when the lasers at 397 and 866 nm are tuned to a Raman resonance of the Λ system coupling the $S_{1/2}$ to the $D_{3/2}$ level via the $P_{1/2}$ level. Excitation spectra on a two-level system provide a resolution which is limited by the natural linewidth. This is different for excitation spectra on a Λ system as mentioned above. The dark resonances, below saturation, have a width which is basically given by the laser linewidth. Fitting a solution of the optical Bloch equations to these dark resonances thus provides valuable information about the performance of the lasers which drive the Raman resonance. Also, from the overall width of the resonances an upper limit of the ions' temperature can be inferred.

In the second part I will present absorption spectra on the narrow $S_{1/2}$ - $D_{5/2}$ transition. These spectra use the technique of quantum jumps where a strong (dipole) transition is coupled to a weak (quadrupole) transition in V-configuration. This allows us to measure the occupation probabilities of a suitably prepared two-level system given by a Zeeman component of the $S_{1/2}$ ground state and a Zeeman component of the $D_{5/2}$ excited state. In principle, these spectra allow for high resolution spectroscopy of the ions' motion in the trap. By recording the sidebands due to the ions' motion in the trap they provide us with a tool to measure the ions' temperature, and in general, a method to determine the motional quantum state in the harmonic oscillator potential of the trap.

Typically, these absorption spectra are measured using a pulsed scheme. This means that during the excitation of the quadrupole transition at 729 nm all other light fields are off to avoid line broadening and shifting due to the ac Stark effect. Each excitation corresponds to a single experiment where the transition is first probed by the 729 nm light field and then the state is measured by applying the lasers at 397 nm and 866 nm. Typically, we repeat this experiment 100 times for sufficient statistics. Averaging over these 100 experiments yields the occupation probabilities for the ground and excited states in our two-level system.

There are several factors which limit resolution for such spectra. The ultimate limit is given by the natural lifetime $\tau \simeq 1$ s of the $D_{5/2}$ level: The frequency uncertainty is $\Delta\nu = 1/(2\pi\tau) \simeq 0.16$ Hz (neglecting the specific Clebsch-Gordan coefficients). Before encountering this limit there are other line broadening mechanisms. The two most dominant mechanisms are laser

linewidth fluctuations and ac magnetic field fluctuations. Presently, we estimate the laser linewidth at 729 nm to be less than 100 Hz. This estimate is inferred from the size of the error signal provided by the lock to the high finesse cavity. Still, this estimate does not guarantee us that the laser at the place of the ions is not much broader, particularly if one takes into account the broadening due to the fiber which guides the light from the laser table to the optical table of the experiment. Our current resolution of about 1 kHz might just be given by such a broadening mechanism. The second broadening mechanism, ac magnetic field fluctuations at line frequency at the ions' position, is severe but can in principle be avoided. Without avoiding it the resolution is limited to about 15 kHz, corresponding to magnetic field amplitudes on the order of 5 mG. This agrees quite well with measured field amplitudes near the trap chamber. Our preliminary solution to avoid these fluctuations is to line trigger each experiment, i. e. to do the interrogation of the quadrupole transition at a fixed phase with respect to the line phase. The interrogation pulses are then chosen to be shorter than the time scale at which the ac magnetic fluctuations occur¹. Changing the phase with respect to the line trigger in fact shifts the center of the resonances on the order of a few kHz in agreement with the change in amplitude of the magnetic field at different line phases.

As we shall see, the absorption spectra recorded so far do not yield excitation probabilities significantly above $P_{ex} = 0.5$. There are two possible reasons: First, we simply may not drive the transition coherently enough. This is the case when the driving pulse length is on the order of the coherence time of our two-level system. Presently, we expect the coherence time to be about 200 μ s, estimated from the width of the resonances. Typical pulse lengths that we have used up to now for recording sideband spectra are in the range of 500 to 1000 μ s. Still, for pulse lengths shorter than the coherence time and for sufficient power one would expect that the excitation probability rises above the value of 0.5. Here the ion's temperature comes into play. As we shall see, for the present trap parameters the average occupation probability of the oscillatory levels is so high even at the Doppler limit temperature the different Rabi frequencies $\Omega_{n',n}$ associated with the oscillatory levels cause a rapid collapse of the excitation probability.

5.1 Excitation spectra

We have recorded two kinds of excitation spectra. We either kept the laser at 397 nm fixed and scanned the laser at 866 nm across resonance, or we reversed the roles of the lasers, keeping the one at 866 nm fixed and scanning the one at 397 nm. As mentioned before, the reason for taking excitation spectra is that they provide us with information about the behavior of the ions in the trap and about laser performance (i. e. drift, linewidth, and intensity). In most cases we used the first kind of excitation spectrum because here the heating effect of the laser once it has traversed the resonance is not so prominent and the risk of loosing ions due to laser heating is significantly reduced (due to the branching ratio 16:1 of the $P_{1/2}$ level). In fact, scanning the laser at 397 nm to the blue side of the spectrum inevitably leads to a loss of ions. This is therefore one possibility to reduce the number of ions in the trap, although in practice it seems difficult to control the heating rate and thus to reduce the ion number in a

¹Even though the line frequency is only 50 Hz, the ac magnetic fluctuations show components up to 1 kHz.

controlled way.

One major drawback in recording the spectra so far has been the use of piezo ceramics to detune the reference cavity to which the laser is locked. First, because of nonlinearities of these piezos we are not able to assign a precise frequency axis to the scans. We estimate the error to be on the order of 10%. Hence, to all fitted parameters in this section an error of this magnitude has to be assigned. Second, the piezos show hysteresis effects, i. e. scanning back and forth or repeated scanning produces different results. Third, and most annoyingly, the piezos are responsible for large drifts of up to 1 MHz per minute. A major improvement can thus be expected when we lock the laser to a fixed reference cavity and switch to scans which are carried out by radio-frequency means, e. g. by either inserting an AOM (in double pass) in the beam to the experiment or by placing an EOM in the beam from the laser to the cavity and to take a tunable sideband to lock the laser to the cavity.

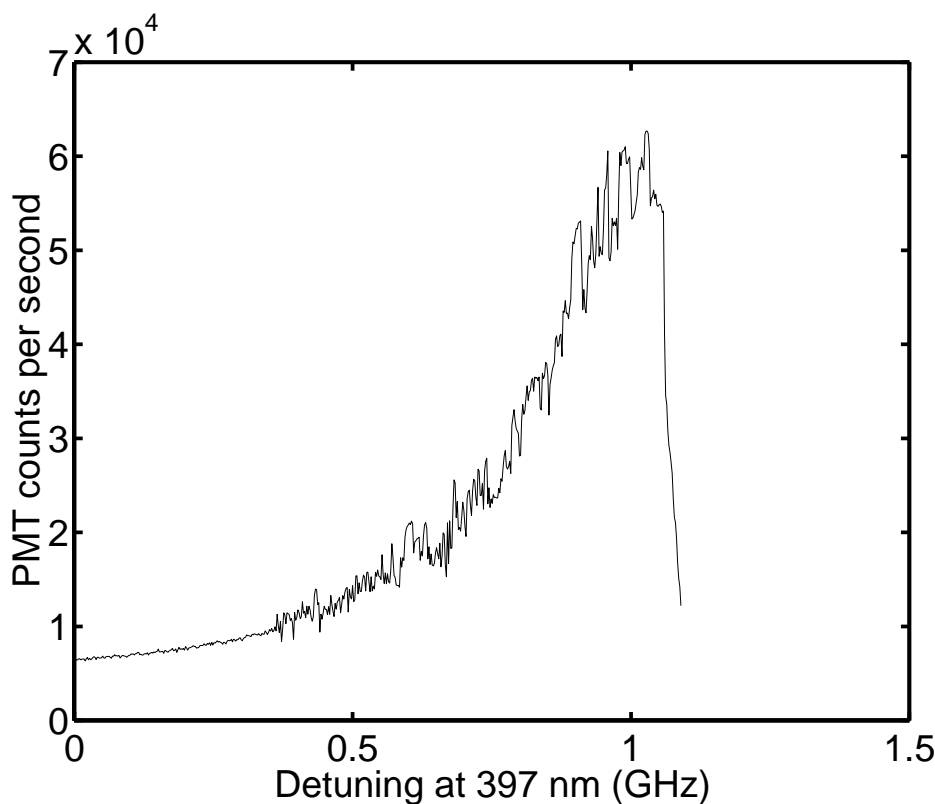


Figure 5.1: Excitation spectrum at 397 nm. 6 ions together with 3 impurity ions. These impurity ions are responsible for the fluctuations in the count rate. The beginning of the fluctuations at the detuning of about 0.3 GHz corresponds to the crystallization of the string. Line broadening can be attributed to power broadening, see text.

Presently, after loading some ions we do not routinely record excitation spectra for the simple

reason that we want to avoid to change the voltages on the piezos as much as possible. The drift rate, which we mostly attribute to the piezos as mentioned above, stabilizes after 30 minutes to acceptable values much below 1 MHz per minute.

5.1.1 Scans at 397 nm

Fig. 5.1 shows a 397 nm excitation spectrum with 6 Ca^+ and 3 impurity ions. The scan was interrupted on the blue side after the abrupt drop in fluorescence to prevent ion loss. The counts are very irregular which agrees with the fact that the ions switch position as monitored on the CCD camera. Seemingly, the ions briefly leave their crystallized state and thus interact with the laser light at a higher temperature. This leads to a reduced scattering rate. For comparison, Fig. 5.2 shows the same scan without the 3 impurity ions. It was taken 1 hour later after successfully dumping the impurity ions by repeatedly blocking laser at 866 nm for short times. All other parameters were kept constant. These and all the following scans have been taken with the laser frequency swept from the low frequency side to the high frequency side of the resonance.

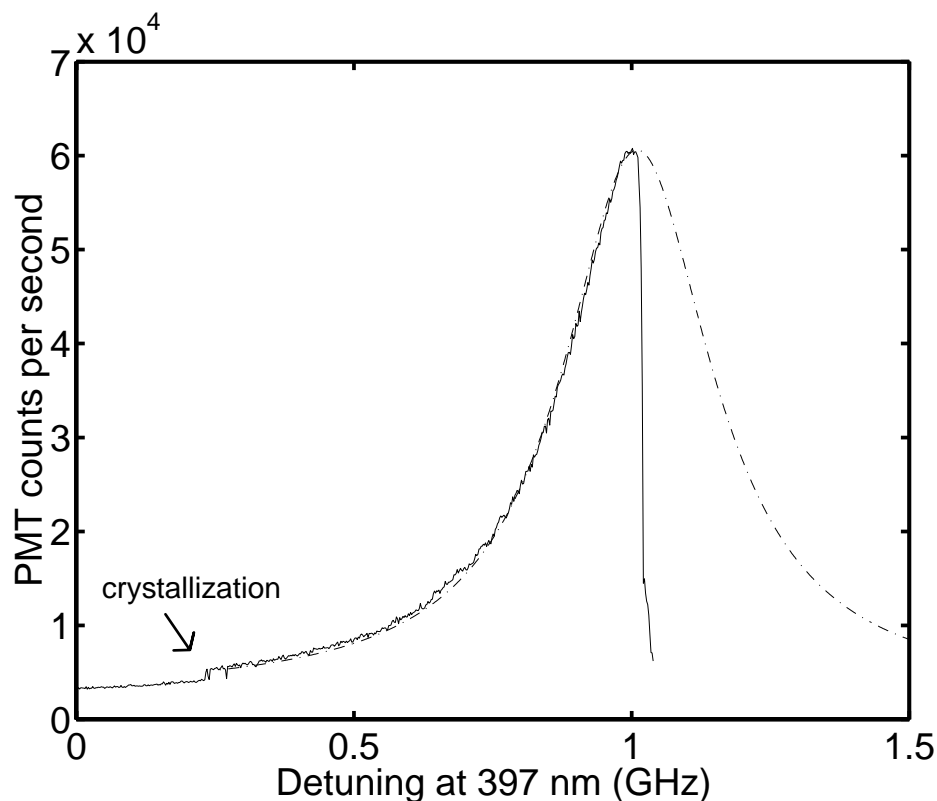


Figure 5.2: (solid) Excitation spectrum at 397 nm. The same 6 ions as in Fig. 5.1, the 3 impurity ions have been lost. (dashed-dotted) Lorentzian fit with width $\Gamma_s = \Gamma\sqrt{1+S}$, where $S = 206$ is the saturation parameter. The point of crystallization is given by the step on the left.

Both scans do not show dark resonances. We attribute this to power broadening which washes out the dark resonances. Assuming that power broadening is the major cause for line broadening, the saturation parameter for these scans can be derived from a Lorentzian fit to the resonance and is of the order $S \simeq 200$.

5.1.2 Scans at 866 nm

Fig. 5.3 shows three successive scans of the laser at 866 nm for different settings of the laser

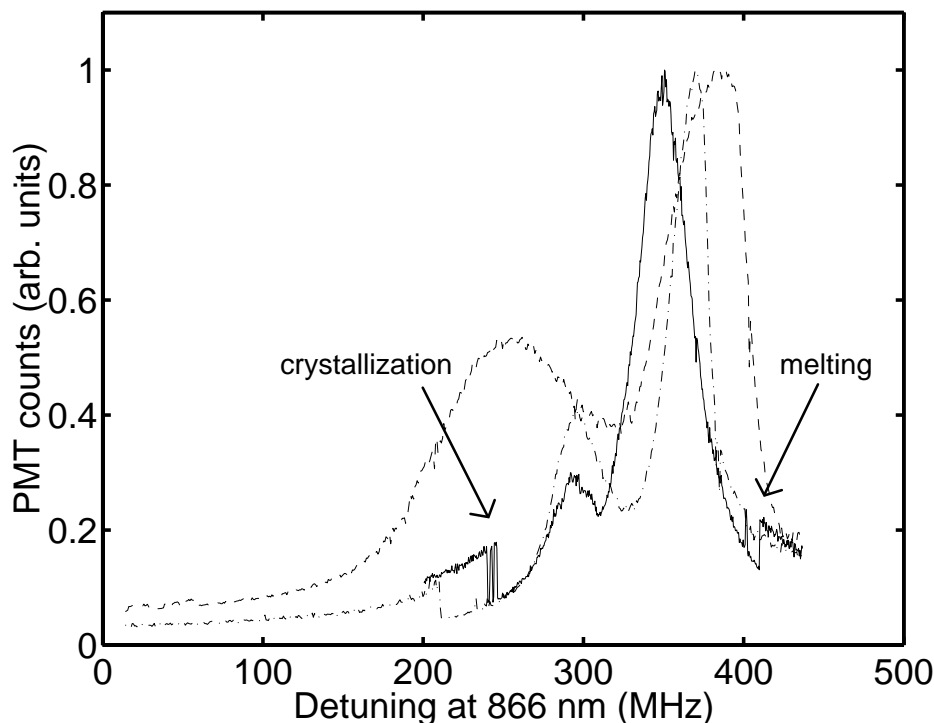


Figure 5.3: Three successive excitation spectra at 866 nm for different settings of the power level (6 ions). For comparison, the PMT counts have been normalized to 1. The shift of the line center from right to left can be attributed to a drift of the laser at 866 nm between successive scans. The solid plot shows a pronounced drop in fluorescence at the point of crystallization. By closer inspection, the ions briefly melt afterwards.

power. In general, reducing the power results in narrower lines and more pronounced features such as phase transitions of the crystal and dark resonances. For these scans individual dark resonances are not resolved due to high laser power. All dark resonances together (4 are expected, see discussion below) melt into a single broad resonance. On the other hand, the phase transition from an ion cloud to an ion crystal produces a sharp drop in fluorescence. The point at which the transition occurs depends crucially on the relative laser detuning and on laser power. Also, scanning back and forth near the transition point reveals hysteresis.

This is obvious, because ions which are already crystallized require less cooling power to stay crystallized.

5.1.3 Dark resonances

When we further reduce the power of the lasers at 397 and 866 nm so that the maximum possible count rate starts to fall, we observe resolved dark resonances in 866 nm scans when the 397 laser is tuned about 20 to 60 MHz to the red of the line center. Fig. 5.4 shows an excitation

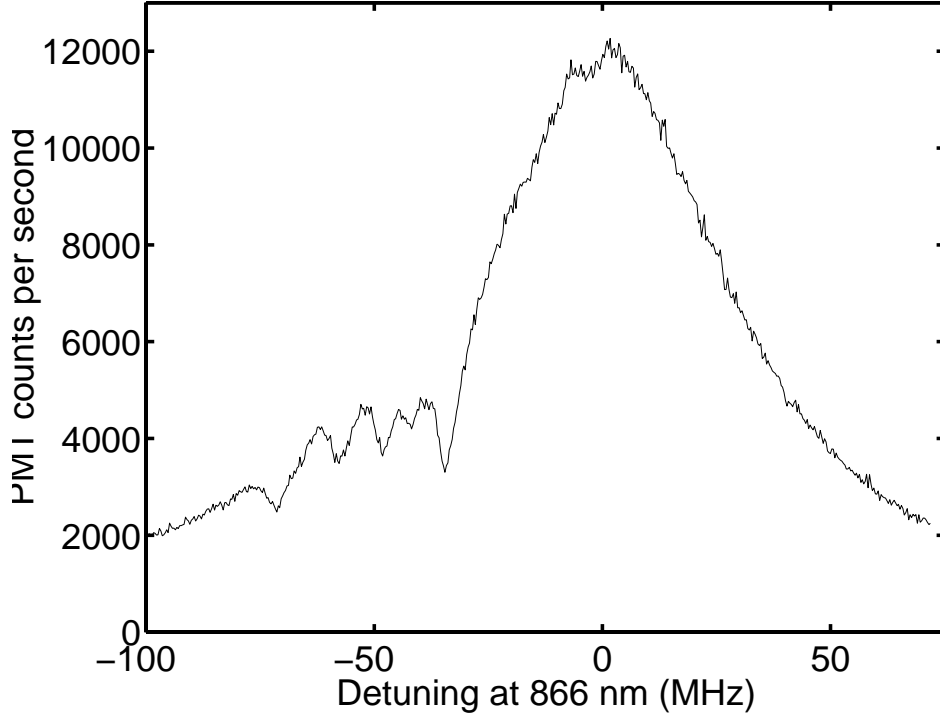


Figure 5.4: Excitation spectrum at 866 nm with dark resonances (6 ions). For the configuration $\mathbf{E}_{866} \parallel \mathbf{E}_{397} \perp \mathbf{B}$ one expects 4 dark resonances. The small dip (fourth dip from the left) results from a slight geometrical misalignment.

spectrum for 6 ions. Here, the laser power has already been lowered so much that the count rate on resonance is reduced to about 20% of the maximum possible value for optimum laser power. For this and the next scan the polarization of both dipole lasers was perpendicular to the magnetic field: $\mathbf{E}_{866} \parallel \mathbf{E}_{397} \perp \mathbf{B}$. This configuration results in 4 dark resonances, which is the minimum number of possible dark resonances [33]. For other configurations up to 8 dark resonances are possible. For the chosen configuration, given the direction of the magnetic field ($\Leftrightarrow 1, 0, 1$), it is necessary to illuminate the ions in the ($\Leftrightarrow 1, 0, \Leftrightarrow 1$) direction (see Fig. 3.3)². The laser beams therefore have no component in the (0, 1, 0) direction, hence laser cooling of this

²Certainly it is possible to change the magnetic field direction so that the (0, 1, -1) beam could be used. On the other hand, this is the magnetic field direction we use for spectroscopy at 729 nm.

direction is not possible or at least very inefficient. The ions thus tend to heat up transversally as discussed in section (4.2). For Fig. 5.6 an additional very weak $(0, 1, \leftrightarrow 1)$ beam was used to avoid this. Fig. 5.5 shows a similar scan for 2 ions. The count rate on resonance is about 30% of the maximum possible value. This scan shows brief melting periods in the transversal direction. This can be observed on the CCD camera. For example, the small peaks on the left result from transversal heating. In this case the ions then heat up also in the longitudinal direction because of the relatively low scattering and hence cooling rate on the far left of the resonance. This increased temperature corresponds to a Doppler profile, which, at the given detuning, leads to higher fluorescence rates (for comparison, see the solid trace in Fig. 5.3. Here, at the point of crystallization the fluorescence jumps from the Doppler profile to the Lorentz profile.).

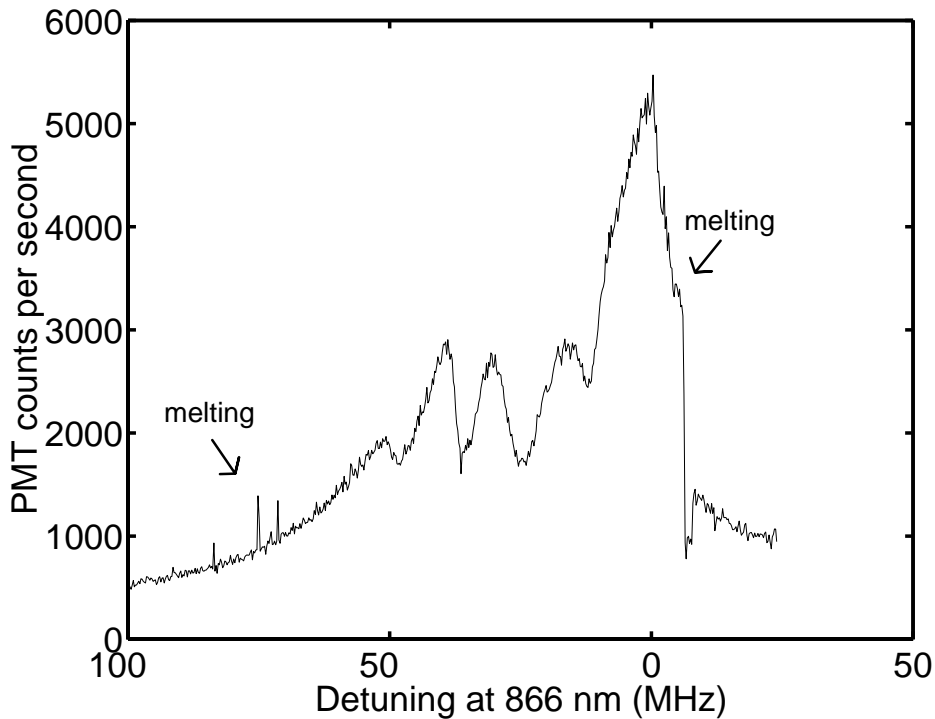


Figure 5.5: Excitation spectrum at 866 nm with dark resonances (2 ions). Same configuration as in Fig. 5.4: $\mathbf{E}_{866} \parallel \mathbf{E}_{397} \perp \mathbf{B}$. The small peaks on the left side of the scan correspond to short melting of the two-ion crystal in the transversal direction to the laser beam as observed on the CCD camera. The abrupt drop on the right of the resonance is due to total melting of the two-ion crystal.

In Fig. 5.6 the 8-level Bloch equations were numerically solved to produce a fit to the data for a single ion [33]. The important free parameters for this fit are the detuning Δ_{397} of the laser at 397 nm relative to the center of the resonance, the saturation parameters S_{866} and S_{397} for both lasers, the combined laser linewidth δ , the magnetic field in units of u , and the angle $\alpha(\mathbf{E}, \mathbf{B})$ between the magnetic field and the polarization directions, which are assumed to be

parallel. For details, the reader is referred to [33], where a detailed study on dark resonances on a single Barium ion is presented.³ For us, the important parameters are δ and u . The value $\delta = 388(16)$ kHz provides a measure of the laser linewidth at 397 nm because the diode laser at 866 nm has a much smaller width on the order of 20 kHz as mentioned before in section (3.2.3). The value of u is needed to calculate the Zeeman splitting on the 729 nm transition.

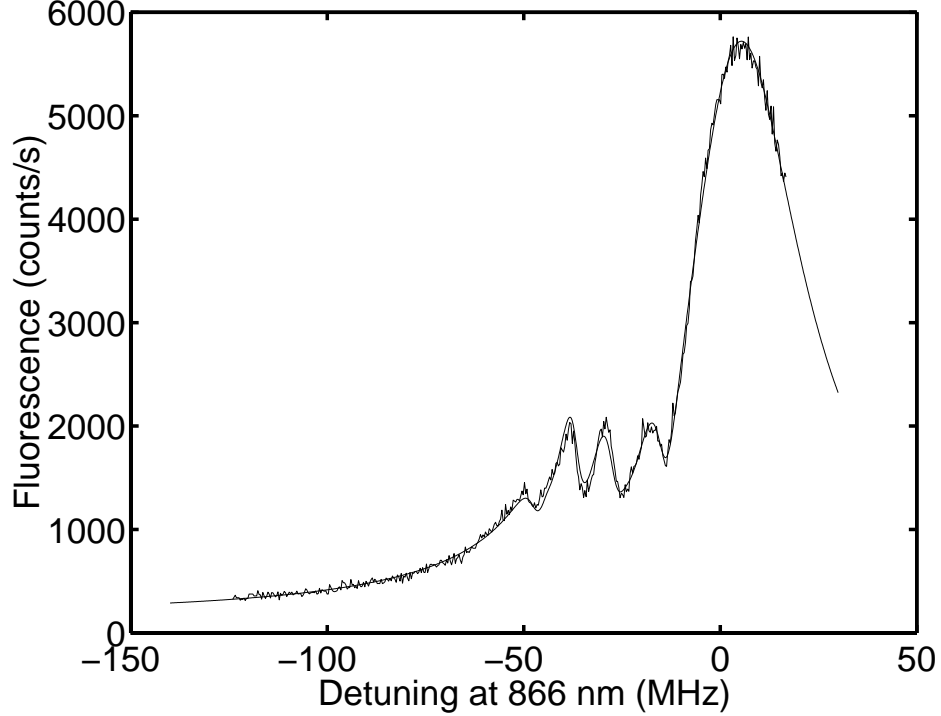


Figure 5.6: Excitation spectrum at 866 nm with 1 ion. Same configuration as in the earlier plots, except that a very weak 397 nm beam from (0, 1, 0) direction was additionally used to provide cooling in this direction. The solid line is a fit using the 8-level Bloch equations. Parameters: Detuning at 397 nm $\Delta_{397} = \leftrightarrow 30.4(1)$ MHz, saturation parameters $S_{866} = 3.19(1)$, $S_{397} = 1.14(1)$, combined laser linewidth $\delta = 388(16)$ kHz, magnetic field $u = 7.41(5)$ MHz, $\alpha(\mathbf{E}, \mathbf{B}) = 97.6(3)^\circ$.

Up to now, the excitation spectra and their dark resonances do not show any pronounced different behavior if one or a few ions are in the trap. In addition, they do not differ significantly from spectra recorded in conventional miniaturized Paul traps where, in general, there is no shallow potential in one direction and the ions are cooled to the Lamb-Dicke regime by conventional laser Doppler cooling. However, for our trap we expect to see oscillation sidebands to the dark resonances similar to the oscillation sidebands on the quadrupole transition (see next section). To resolve these sidebands it is necessary that the laser linewidth at 397 nm is improved to a level below the sideband spacing at currently 100 to 200 kHz.

³The $^{138}\text{Ba}^+$ ion has the same level scheme as the $^{40}\text{Ca}^+$ ion so that (with different wavelengths and decay constants) the same effects are observed.

5.2 Absorption spectra on the quadrupole transition

So far we have measured absorption spectra on the $S_{1/2} - D_{5/2}$ quadrupole transition mostly for the case of a single ion. The reason for this is given by the multitude of sidebands which appear even in the case of a single ion at temperatures near the Doppler limit. As we will see later, a single ion above the Doppler limit can produce so many sidebands that it gets difficult to resolve these resonances and to identify the carrier. Thus, for the present trap parameters, spectroscopy on more than 1 ion is only reasonable if temperatures can be reduced to or below the Doppler limit. Therefore, in the following always a single ion will be considered.

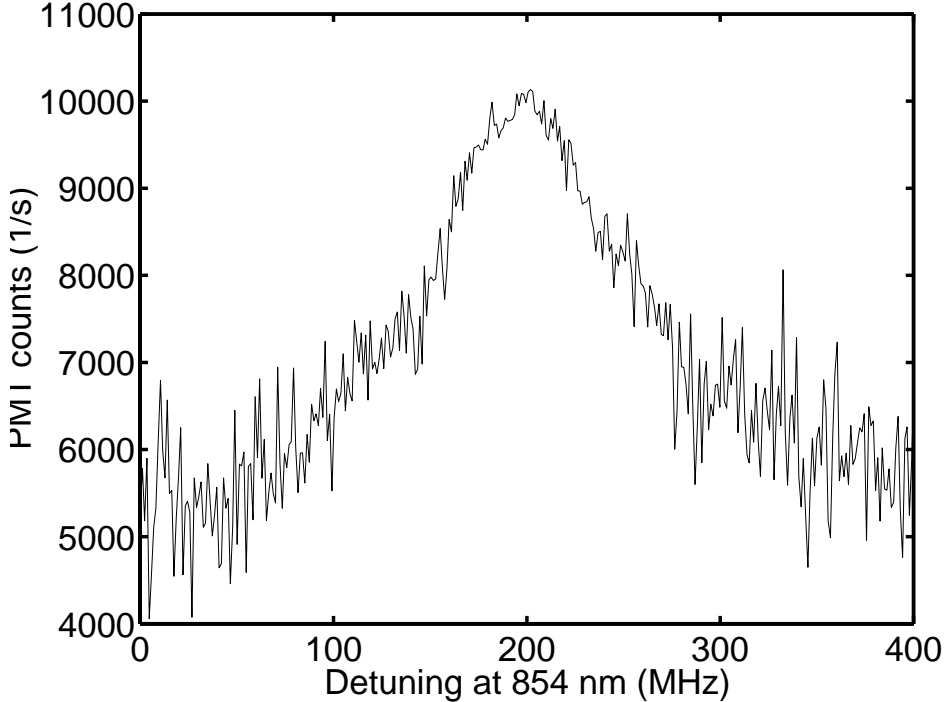


Figure 5.7: Depopulation spectrum at 854 nm (1 ion) while all other lasers are on, in particular the one at 729 nm. The laser power has been reduced by 21 dB from the value used for pulsed spectroscopy.

5.2.1 Laser optimization

The procedure for optimizing the lasers at 854 nm and 729 nm to record pulsed spectra on the quadrupole line is as follows. After preparation of an ion in the trap the lasers at 854 and 729 nm are tuned on resonance. For the 854 nm laser this generally means that its frequency is determined on a wavemeter ($\frac{\Delta\nu}{\nu} = 10^{-6}$) or, in addition, for a more precise value by hollow cathode spectroscopy. For full power (typically 1 mW in front of the trap) this suffices to clear out the $D_{5/2}$ level even if the laser is still detuned from exact resonance by a few hundred MHz. We choose its polarization in such a way so that all Zeeman sublevels are

depopulated. At the same time, the laser at 729 nm is set to the right wavelength again with the help of a wavemeter. While the laser at 854 nm is off we look for quantum jumps induced by this laser. On resonance this laser drives the ion in saturation, so the fluorescence count rate drops to approximately 1/2. As known from previous measurements the broadband AOM which detunes this laser is set to such a value that on resonance the laser can be locked to the high finesse cavity (Free spectral range FSR = 750 MHz). After this is done the 854 nm laser is turned on and its beam direction is adjusted to assure optimum depopulation of the $D_{5/2}$ level.

Fig. 5.7 shows a spectrum at 854 nm for low power (less than 1μ W) while all other lasers are on resonance. For this, the reference cavity to which the laser at 854 nm is locked is tuned with the help of a piezo. One can see that off resonance, the fluorescence from the ion is reduced to approximately 1/2 because the laser at 729 nm saturates the $S_{1/2} - D_{5/2}$ transition. The fluctuations are given by a rapid sequence of quantum jumps where the ion switches between the ON and OFF state. At resonance though, the laser at 854 nm recycles the ion quickly so that the laser at 729 nm is ineffective in shelving the ion. For optimizing the overlap of the laser focus with the ion, the power on resonance is reduced so much that the fluorescence level drops. Then, by spatially adjusting the beam one tries to maximize the fluorescence again. Finally, the power of the 854 nm laser is set to maximum value to assure efficient clear out of the population in all Zeeman components of the $D_{5/2}$ level even for short pulse times. A different procedure is used when optimizing the overlap of the laser focus of the 729 nm laser with the ion. In this case one tries to increase the rate of quantum jumps at reduced laser power while the laser at 854 nm is off. In general, the frequency of this laser does not need to be adjusted because its reference cavity is stable to within 1 MHz with respect to the atomic transition (this includes a slightly varying magnetic field which shifts the Zeeman components). The variations of the line center on a day to day basis are expected to be well below this shift due to the magnetic field. A coarse scan with the AOM across the Zeeman resonances thus reproduces the lines to within a MHz.

5.2.2 Pulsed spectroscopy

Fig. 5.8 shows a typical sequence for the laser pulses used to interrogate the quadrupole transition in the case when the experiment is not synchronized to the line frequency. During the first part of the sequence (2 ms) the ion is Doppler cooled and then prepared in the $S_{1/2}(m_J = 1/2)$ Zeeman sublevel by the circularly polarized beam denoted 397 s. Also, the laser at 854 nm is used to depopulate in the $D_{5/2}$ level if this has been excited by light at 729 nm. Then the ion is driven on the 729 nm line (up to 1 ms). During this time, all other lasers are off.⁴ Afterwards, the ion is interrogated (2 ms) while counting fluorescence with the PMT. Typically, we count 12 to 15 photons per ion during that time in addition to an average of 2 photons of dark counts and stray light. This allows us to discriminate between ON and OFF, i. e. to decide whether the ion has been in the $S_{1/2}$ or in the $D_{5/2}$ state. For more than one ion we set additional

⁴Certainly, the laser at 866 nm does not need to be off because it does not couple to the quadrupole transition. A crude estimate shows that exciting the transition at 854 nm with light at 866 nm should be suppressed by a factor of 10^{10} . In any case, we have checked that it does not make a difference if one leaves this laser on within the current resolution.

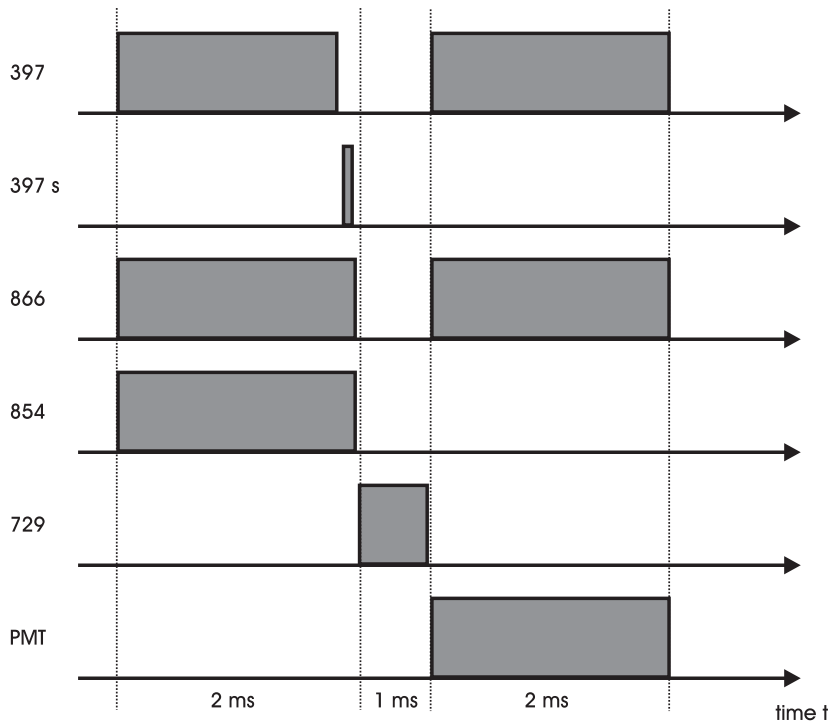


Figure 5.8: Typical pulse sequence for excitation at 729 nm on the $S_{1/2} - D_{5/2}$ transition in the case of no line synchronization. Each experiment takes 5 ms. This sequence is repeated 100 times, then one of the parameters (detuning, pulse duration, or power at 729 nm) is stepped to the next value.

thresholds to account for the fact that a varying number of ions is ON or OFF. In order to get sufficient signal to noise ratio the pulse sequence is repeated at least 100 times. Then one of the parameters is set to the next value, e. g. for an absorption spectrum the AOM frequency for the laser at 729 nm is stepped. Instead of increasing the number of experiments at one step we sometimes repeat the entire scan a few times if we need a better signal to noise ratio. This procedure has the disadvantage that drifts of the laser frequencies with respect to the transition lead to shifts of the resonances from scan to scan. The magnitude of the shift depends on the time it takes to record one scan. It is usually on the order of 1 kHz for the laser at 729 nm.

Synchronizing the experiment to the line frequency at 50 Hz certainly allows for much more time for laser cooling and for collecting fluorescence. This makes it easier to set a threshold which discriminates between ON and OFF. On the other hand, a major drawback is given by the extra time it takes to carry out each experiment. With line triggering, each experiment takes 20 ms. Without line triggering, we have been able to reduce the time per experiment to 2 ms for optimum laser parameters.

It is important to note that switching the lasers off (i. e. the ones at 854 nm and 397 nm) is

not as trivial as it might seem. The crystal in the AOM used for switching generally produces stray light into the direction of the first order laser beam directed at the ions. This light is certainly also present when the AOM is off. For the laser at 854 nm we thus use a carefully aligned AOM in double pass so that the stray light is at a frequency which is shifted by twice the AOM center frequency and thus is not in resonance with the ions. For the light at 397 nm we use two AOMs. One AOM is in front of the fiber is used for guiding the light from the laser table to the experiment table. When this AOM is off, no light can be detected behind the fiber.

5.2.3 Zeeman components

In order to resolve the Zeeman components of the quadrupole transition we typically apply a

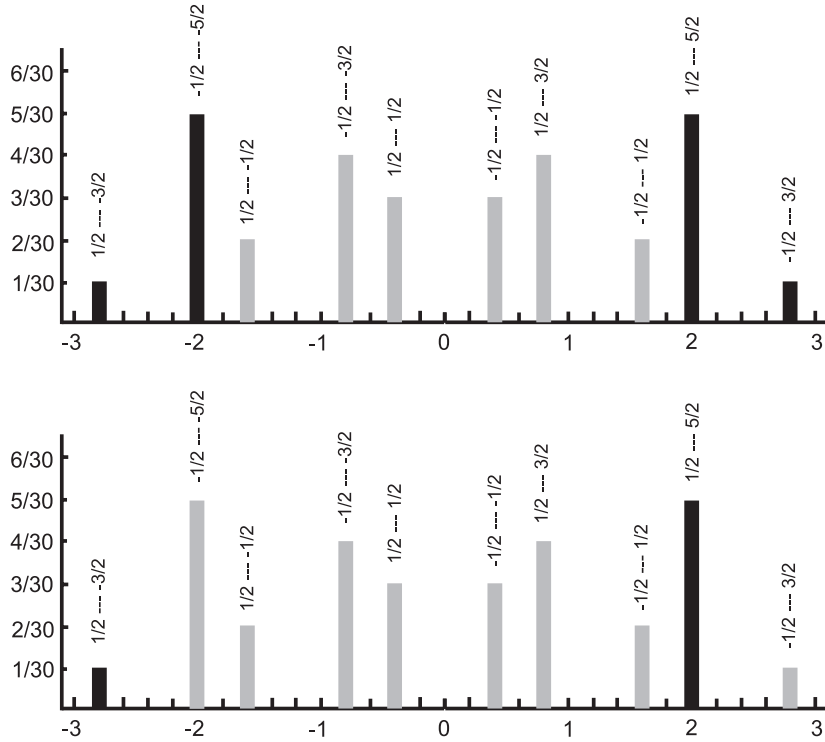


Figure 5.9: Expected Zeeman spectra for the configuration $\mathbf{B} \perp \mathbf{k}_{729}$ and $\mathbf{B} \perp \mathbf{E}_{729}$. Above: Equal occupation of the $S_{1/2}$ Zeeman sublevels $m_J = \pm 1/2$ and $m_J = +1/2$. Below: With optical pumping into the $m_J = +1/2$ level. The frequency axis is in units of Bohr's magneton ($\simeq 1.4$ MHz/G). The height of the lines represents the relative line strengths.

magnetic field of about 0.3 to 0.6 mT (see appendix for the Zeeman splitting). This results in a spread of the entire Zeeman spectrum across 20 to 50 MHz and assures that the motional sidebands of neighboring Zeeman lines do not overlap significantly (for 0.5 mT the smallest distance between two lines is 2.8 MHz, so that 28 sidebands with 100 kHz spacing would fit

between two adjacent Zeeman components). The top part of Fig. 5.9 shows the expected Zeeman spectrum for an appropriately chosen magnetic field direction and polarization ($\mathbf{B} \perp \mathbf{k}_{729}$ and $\mathbf{B} \perp \mathbf{E}_{729}$). The expected lines are in black, all other lines which are not excited are in grey. The bottom part shows the expected spectrum when only the $m_J = 1/2$ Zeeman sublevel of the $S_{1/2}$ ground state is prepared by applying a circularly polarized beam at 397 nm parallel to the magnetic field direction. Fig. 5.10 shows two experimental Zeeman spectra for the configuration $\mathbf{B} \perp \mathbf{k}_{729}$ and $\mathbf{B} \perp \mathbf{E}_{729}$, one with optical pumping beam at 397 nm and

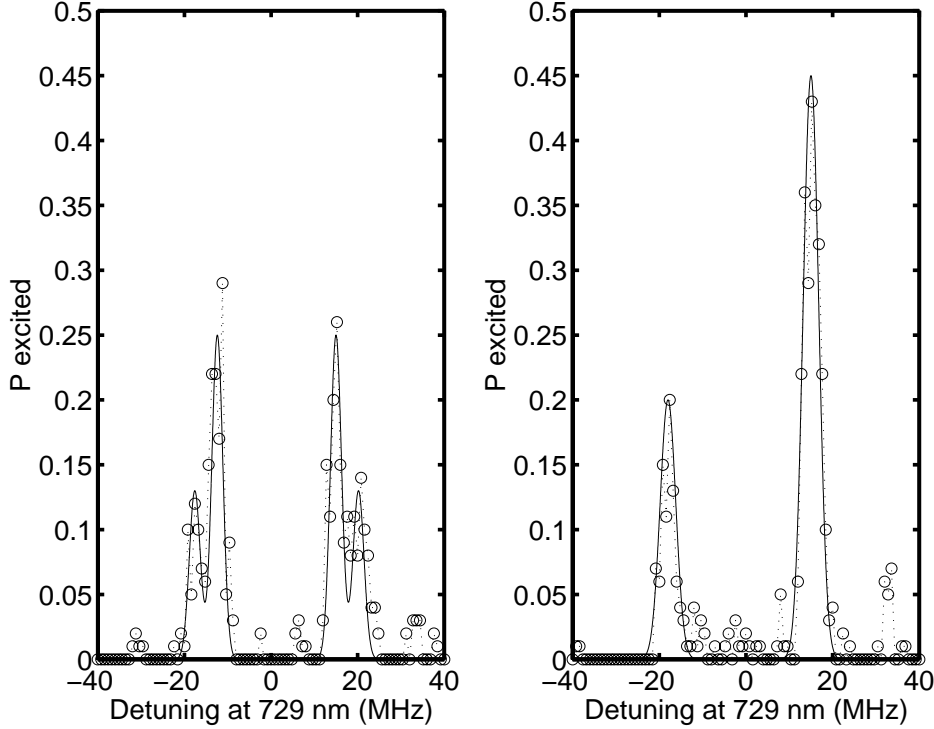


Figure 5.10: Zeeman components for 1 ion. On the right, the σ^+ beam at 397 nm was used to prepare the $m_J = +1/2$ level. On the left, this beam was not used to show all 4 possible transitions for the configuration $\mathbf{B} \perp \mathbf{k}_{729}$ and $\mathbf{B} \perp \mathbf{E}_{729}$.

the other one without optical pumping beam. For these spectra we have adjusted the power of the 729 nm laser so that the strong lines are barely saturated. Therefore, the weaker lines are lower. The left plot shows that without optical pumping the Zeeman levels of the ground state are approximately equally populated. The scan is too coarse to resolve the motional sidebands (step width 800 kHz). It is not easy to record these spectra because, as we shall see shortly, each Zeeman line consists of many narrow resonances which are the axial oscillation sidebands. Thus, a low resolution scan (i. e. with a coarse step width) with a narrow bandwidth laser can result in strange spectra because of insufficient sampling. Therefore, if one does not want to increase the resolution it is necessary to broaden the resonances so that they together appear as a single broad line. For the scans in Fig. 5.10 the main broadening mechanism was given by ac magnetic field fluctuations as discussed before when no triggering to the line frequency

is used.

5.2.4 Sideband spectrum

Before showing high resolution scans of one of the Zeeman components I want to discuss first what kind of spectrum one expects. Fig. 5.11 shows the expected sideband spectrum of one of the Zeeman components of the $S_{1/2} - D_{5/2}$ line. It is assumed that the ion is cooled to the Doppler limit of the dipole $S_{1/2} - P_{1/2}$ transition ($T \simeq 0.5$ mK, corresponding to $\bar{n}_r = 7$ and $\bar{n}_z = 76$ in our trap). Below saturation, the envelope of the axial sidebands is given by the usual Gaussian which one gets for Doppler broadening (cf. equation (46) in [18]). The total number S of axial sidebands spanning the FWHM width is given by $S = 4\sqrt{\log(2)}\sqrt{\bar{n}_z}\eta_z \simeq 7$. The radial sidebands have additional sidebands at the axial oscillation frequency.

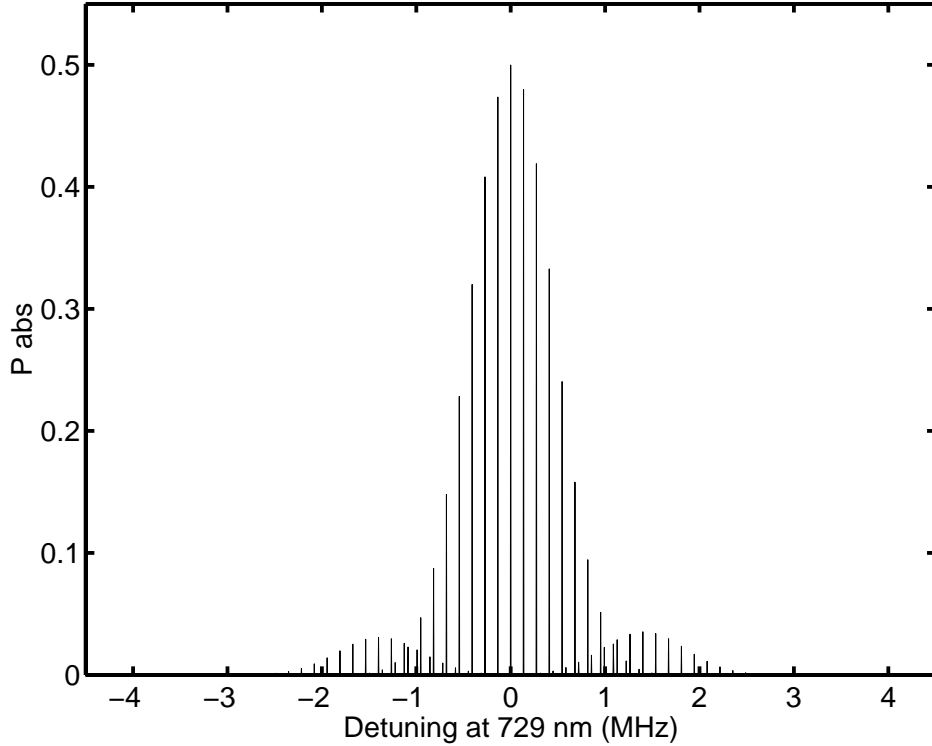


Figure 5.11: Expected sideband spectrum of the $S_{1/2}(m_J = 1/2) - D_{5/2}(m_J = 5/2)$ Zeeman line for 1 ion below saturation at the Doppler limit. Temperature $T = 0.5$ mK, oscillation frequencies $\nu_z = 136$ kHz, $\nu_r = 1.39$ MHz, magnetic field $B = 5.36$ G. The scaling on the vertical axis is arbitrary. The radial sidebands are exaggerated by a factor of 10 compared to the carrier.

Temperatures at the Doppler limit of the $S_{1/2} - P_{1/2}$ transition can only be achieved if the Doppler cooling lasers (at 397 nm and 866 nm) do not saturate the ion and if they are tuned properly. In the first case, power broadening increases the minimum attainable temperature.

On the other hand, we generally make use of power broadening because the absorption spectra are very sensitive to drifts of these lasers without some linewidth broadening mechanism. Also, possible heating mechanisms might increase the temperature. Therefore, in a typical experiment the ion's temperature is expected to be slightly above the Doppler limit if no additional cooling mechanism is applied. The bottom plot of Fig. 5.12 shows the expected sideband spectrum at $T = 4$ mK of the $S_{1/2}(m_J = 1/2) - D_{5/2}(m_J = 5/2)$ Zeeman line for

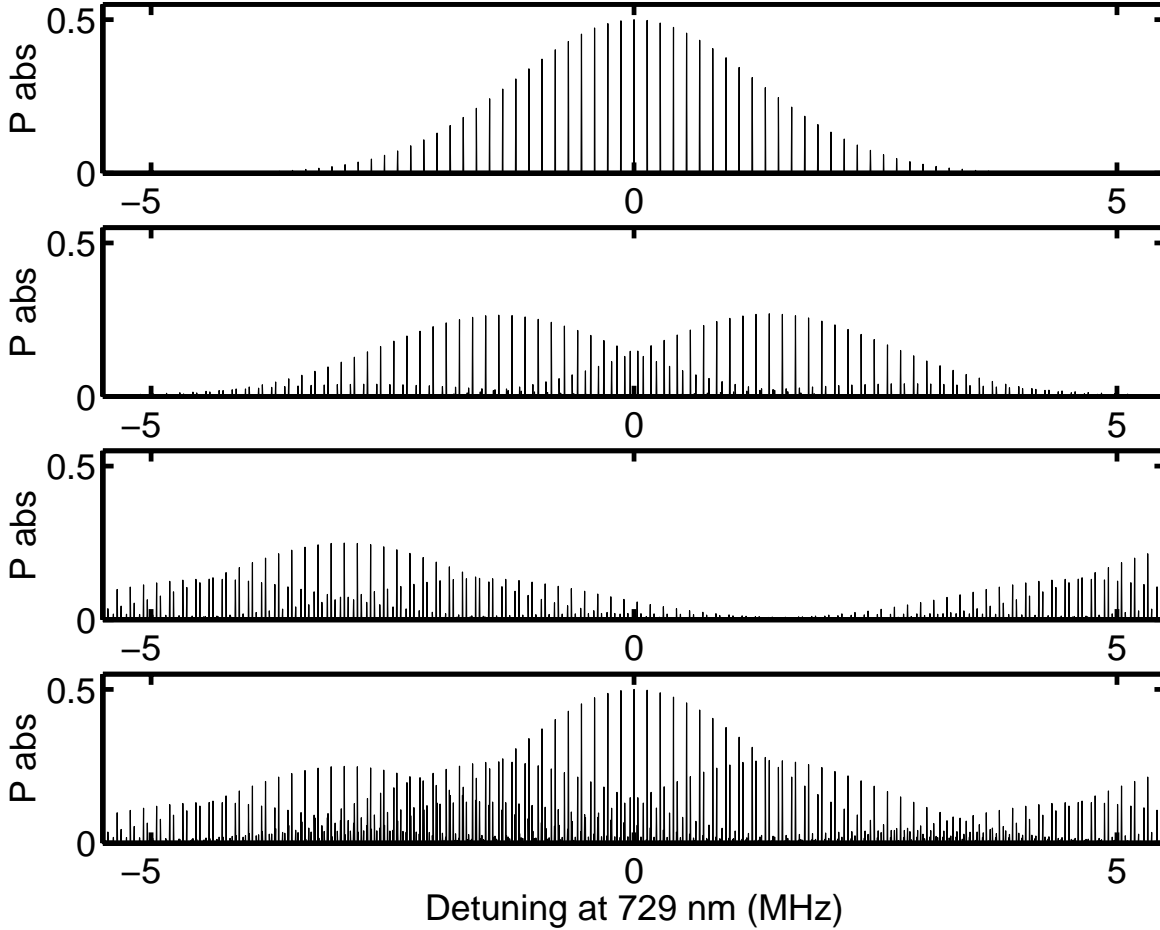


Figure 5.12: Assembling the sideband spectrum at $T = 4$ mK (below saturation). Other parameters are the same as in Fig. 5.11. Top: Zeeman line with axial oscillation sidebands. Second from top: Only radial sidebands with axial subcomponents. Second from bottom: Neighboring Zeeman components with axial and radial sidebands. The height of these components is exaggerated, see text. Bottom: All of the three top plots together.

an axial frequency of $\nu_z = 136$ kHz and a radial frequency of $\nu_r = 1.39$ MHz. One expects approximately 20 axial sidebands (FWHM) to the carrier. The radial sidebands (together with their axial sidebands) can clearly be seen. They are responsible for extra resonances

near the carrier (see Fig. 5.13). The neighboring Zeeman components have also been included

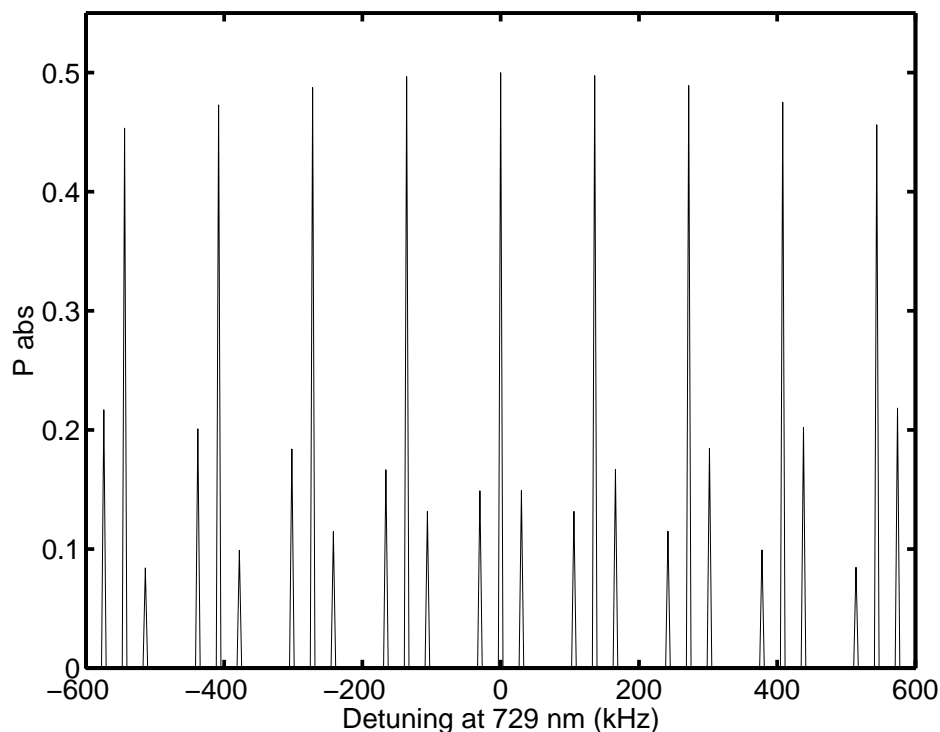


Figure 5.13: Center part of the bottom plot in Fig. 5.12. The carrier is at 0 detuning. It possesses sidebands at the axial oscillation frequency $\nu_z = 136$ kHz. The carrier together with its axial sidebands is the 'main comb'. Next to the tall sidebands there are additional resonances which are higher order axial sidebands to the first upper and first lower radial sideband. These are the 'side combs'. The order of the sidebands can easily be determined. For example, given a radial frequency of $\nu_r = 1.39$ MHz, the first small resonance to the right of the carrier is the 10th red axial sideband of the first blue radial sideband: $\nu = \nu_r \Leftrightarrow 10\nu_z$.

(see Fig. 5.9), although their height is put at an arbitrary value with respect to the main line. In a real scan, their appearance depends on imperfections in laser polarization and optical pumping, and also on saturation. The entire spectrum thus looks like the overlap of several combs. Each comb is given by a center line with sidebands at the axial oscillation frequency. The width of each comb is given by the Doppler width (below saturation), and the spacing between the combs is given by the radial oscillation frequency and the Zeeman splitting.

Fig. 5.14 shows an experimental scan of the $S_{1/2}(m_J = 1/2) - D_{5/2}(m_J = 5/2)$ Zeeman line. More than 30 axial oscillation sidebands can be seen. The sidebands reach out even further than shown in this plot. In order to clearly resolve all sidebands the experiment was line triggered. In total 4400 data points at a step width of 1 kHz were taken, corresponding to an overall acquisition time of nearly 3 hours for 100 experiments per frequency step. This step

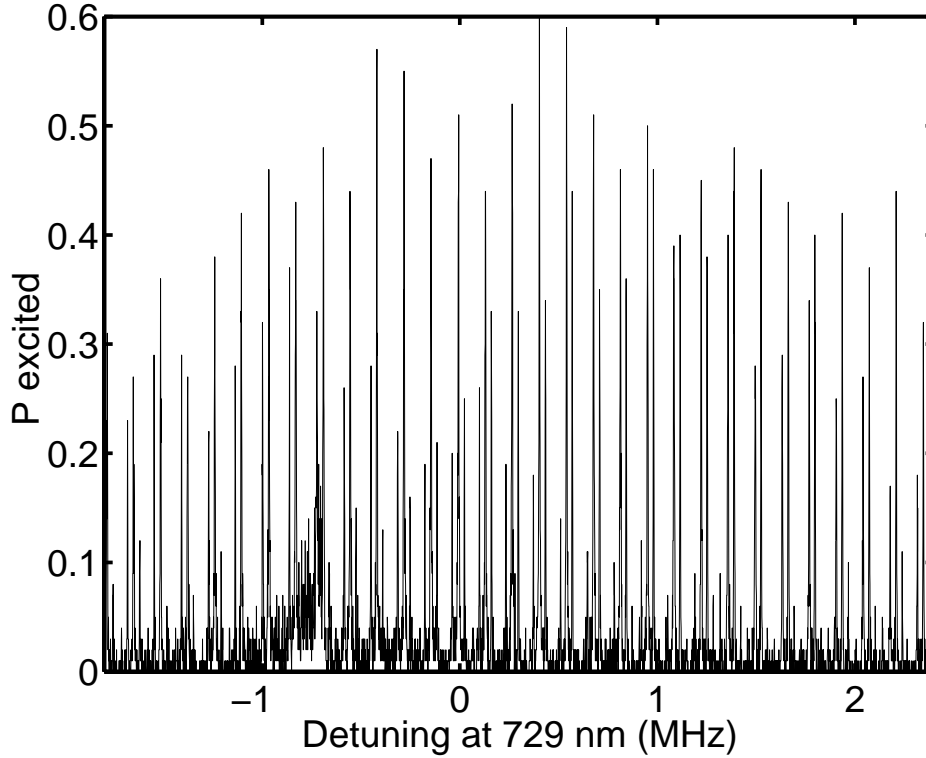


Figure 5.14: Complete sideband spectrum of the $S_{1/2}(m_J = 1/2) - D_{5/2}(m_J = 5/2)$ Zeeman line for 1 ion. $\nu_z = 138.0(1)$ kHz. The step width is 1 kHz. The data points at a detuning near ± 0.8 MHz show enhanced noise because the repumping laser at 866 nm drifted off resonance. See text.

width is still too large given the width of each individual resonance ($\Delta\nu \simeq 3$ kHz). The height of the resonances thus acquires an additional error of approximately 0.1. Another source of error affecting the height of the resonances is given by projection noise [5]. At the peak of the main resonances where the excitation probability is $P_{ex} \simeq 0.5$, the error (for $N = 100$ experiments) is given by $\sigma = \sqrt{P_{ex}(1 - P_{ex})}/\sqrt{N} \simeq 0.05$. Note that many peaks reach up to 0.5 or even above 0.5. Obviously, we are not in the low power regime. Saturation effects therefore have to be taken into account, in particular when one tries to deduce a temperature from the height of the peaks (see discussion below).

A major problem with recording such a long scan is the drift of all lasers during this time. This can be seen in Fig. 5.14 at data points with a detuning near ± 0.8 MHz. Here, the repumping laser at 866 nm drifted so much off resonance that the fluorescence count rate dropped to a level where the preset threshold could not discriminate between the ground state and the excited state anymore. In this particular case the laser was re-adjusted to resonance while not interrupting the scan.

The center part of this spectrum is shown in Fig. 5.15. This is the region where the carrier

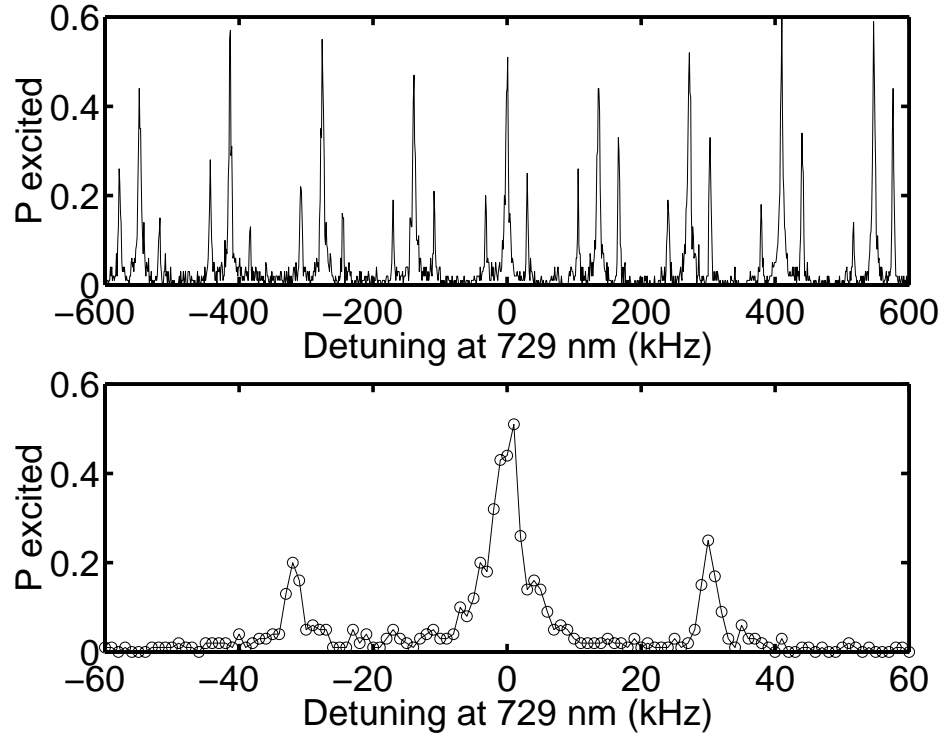


Figure 5.15: Central part of Fig. 5.14 where the carrier of the $S_{1/2}(m_J = 1/2) - D_{5/2}(m_J = 5/2)$ Zeeman line is expected. Top: Main comb with the first upper and lower side combs. The upper side comb gradually increases from left to right in agreement with the fact that its maximum should be at $\Delta\nu = 1.39$ MHz from the carrier. The same applies to the lower side comb with $\Delta\nu = \pm 1.39$ MHz. Bottom: Center of top plot with presumed carrier.

of the transition is expected, although in this particular case we did not try to identify the carrier (see next subsection). In the top plot one can clearly see that there are main resonances spaced at the axial oscillation frequency $\nu_z = 136$ kHz (the 'main comb') flanked by smaller resonances. These smaller resonances are axial sidebands to the first upper and lower radial sideband (the upper and lower 'side combs'). This plot is to be compared with Fig. 5.13. From the frequency spacing between the different combs and from the knowledge that the radial oscillation frequency must be near 1.4 MHz we can deduce $\nu_r = 1.390(2)$ MHz. From the width of the envelope of the main comb we can deduce an upper limit for the ion's temperature. This is $T = 9(3)$ mK. Because of saturation we expect the actual temperature to be smaller by at least a factor of two.

Obviously, it is not very practical to determine the ion's temperature from a full spectrum such as the one shown in Fig. 5.14. For determining the envelope of the main comb it suffices to record only selected resonances which belong to this comb and to leave out all the points

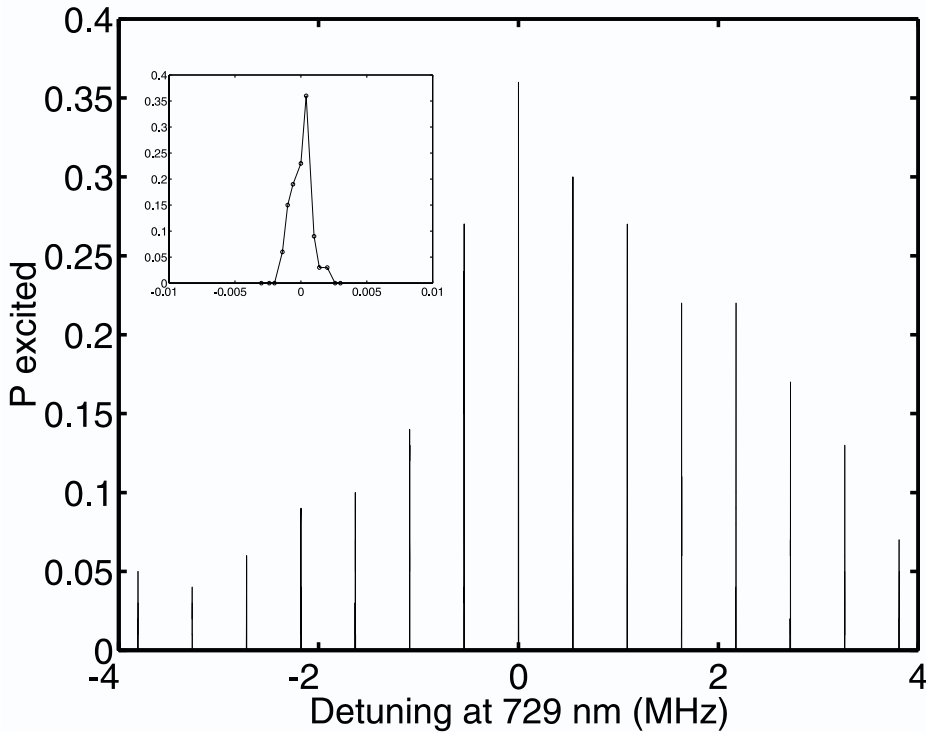


Figure 5.16: Experimental sideband spectrum where every 4th sideband is recorded. The sidebands appear as δ -peaks, but, as shown in the inset for the central peak, each sideband consists of approx. 4 data points (FWHM). The height for most peaks is given by only a single data point, so that the ion temperature can only be inferred with a large error. The step width is 500 Hz.

in between. This is shown in the spectrum of Fig. 5.16, where every 4th sideband is recorded. This spectrum is preliminary because each sideband still consists of too few points, so that for each sideband a height can only be given with large error. The advantage of this spectrum is given by the significantly reduced time needed for recording. On the other hand, to select the particular sidebands a precise knowledge of the sideband spacing from previous measurements is required. Assuming no power broadening, the temperature deduced from this spectrum is $T = 5.5(6)$ mK.

Fig. 5.17 shows the typical resolution which can be achieved with line triggering. The width of the resonance is below 2 kHz, corresponding to a resolution of better than $\Delta\nu/\nu = 4.9 \cdot 10^{-12}$. For this scan an arbitrary sideband was selected. The phase of the line trigger was adjusted to produce a narrow resonance. Other phases can result in resonances which are at least a factor 2 broader because of higher magnetic field fluctuations at these particular phases. At this resolution it becomes important to consider effects such as the drift of the laser with respect to the resonance during data acquisition. Also, at pulse lengths of $t = 1$ ms the broadening given by a sinc-function of approximate width $1/t = 1$ kHz due to the finite interaction of the

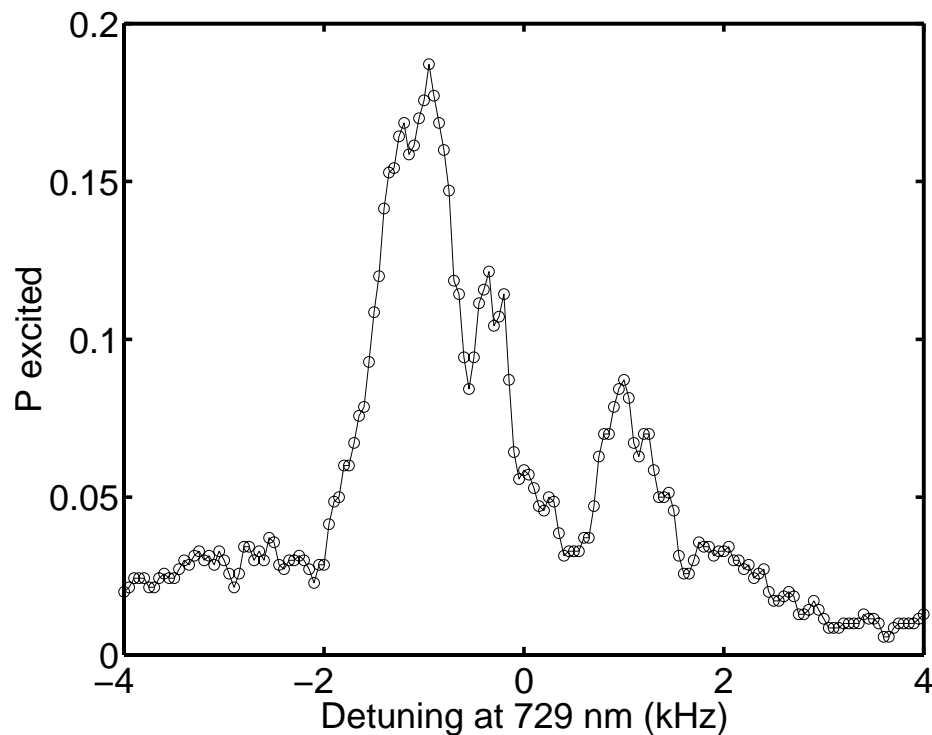


Figure 5.17: Some sideband of the $S_{1/2}(m_J = 1/2) - D_{5/2}(m_J = 5/2)$ transition recorded with line triggering (1 ion). The laser power at 729 nm was reduced to avoid power broadening. The pulse length at 729 nm is 1 ms. Each point corresponds to 700 experiments. The small resonance on the right side of the main peak seems to belong to another comb. So does the larger resonance further to the right. The width of the line including the small side resonance is below 2 kHz, corresponding to a fractional resolution of $\Delta\nu/\nu = 4.9 \cdot 10^{-12}$.

laser with the transition needs to be taken into account.

For comparison Fig. 5.18 shows two scans of the $S_{1/2}(m_J = 1/2) - D_{5/2}(m_J = 5/2)$ Zeeman transition when line triggering is not used. In general, resolution is limited to about 15 kHz. For the two upper plots, by choosing an appropriate rf-voltage on the quadrupole electrodes the radial frequency was tuned to such a value that both side combs overlapped significantly. This produces the small and broader resonances midway between the main resonances. For the two lower plots the radial frequency was chosen so that upper, lower, and main comb overlap.

Spectroscopy without line triggering is quite useful when a quick overview of the entire spectrum is needed. The duration of the pulse length can be reduced by a factor of 10 compared to line triggered data acquisition. In addition, because of broader resonances, less data points need to be taken. Together this results in data acquisition which is about 50 times faster.

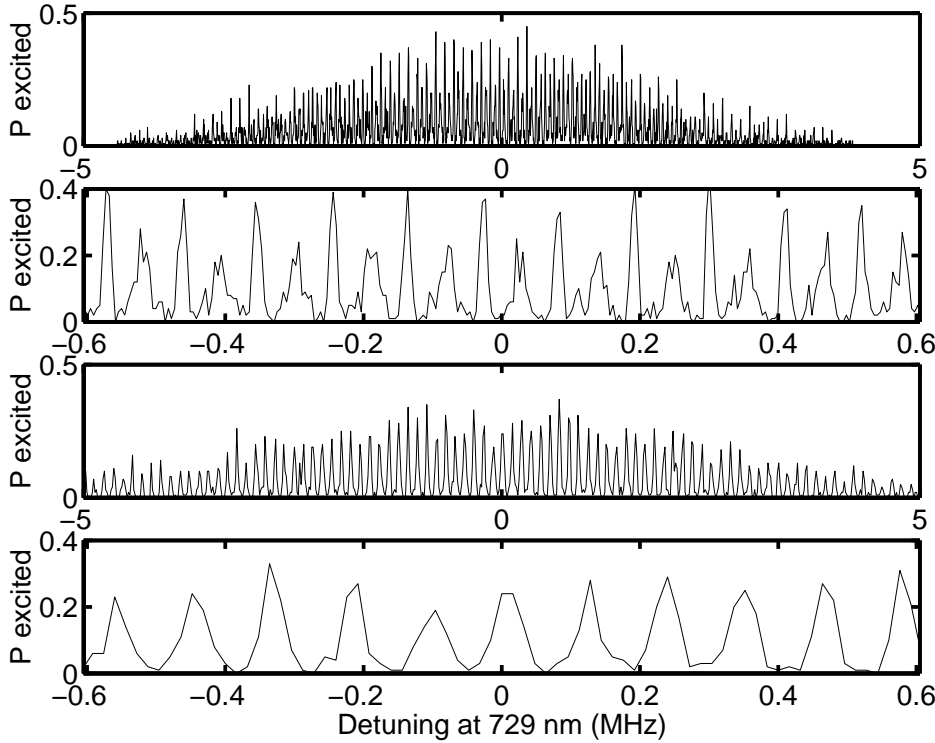


Figure 5.18: Spectroscopy without line triggering. The resolution is limited to about 15 kHz. Top and second (detail) from top: The upper and lower side combs overlap to produce peaks midway between the resonances of the main comb. Third and fourth (detail) from top: Upper, lower, and main comb overlap significantly to produce broad resonances.

5.2.5 Carrier of the sideband spectrum

With so many sidebands present it is not possible to clearly identify the carrier of the transition by inspection of the spectrum. A relatively easy way to determine the carrier is to vary the axial oscillation frequency ν_z by changing the voltage on the ring electrodes of the trap by about 10%. This gives a comparable change in axial oscillation frequency. The carrier is not affected by this change and therefore does not move between two successive scans (except for the drift caused by varying magnetic fields and drifting reference cavity). On the other hand, as can be seen from Fig. 5.19, all sidebands move with respect to the carrier. For this plot line triggering was not used to allow for fast data acquisition as mentioned before. In order to avoid the additional resonances given by the side combs the radial oscillation frequency was also tuned to provide comb overlap similar to the bottom plot in Fig. 5.18.

Fig. 5.20 presents a spectrum when for the first time we have been able to zoom in on the

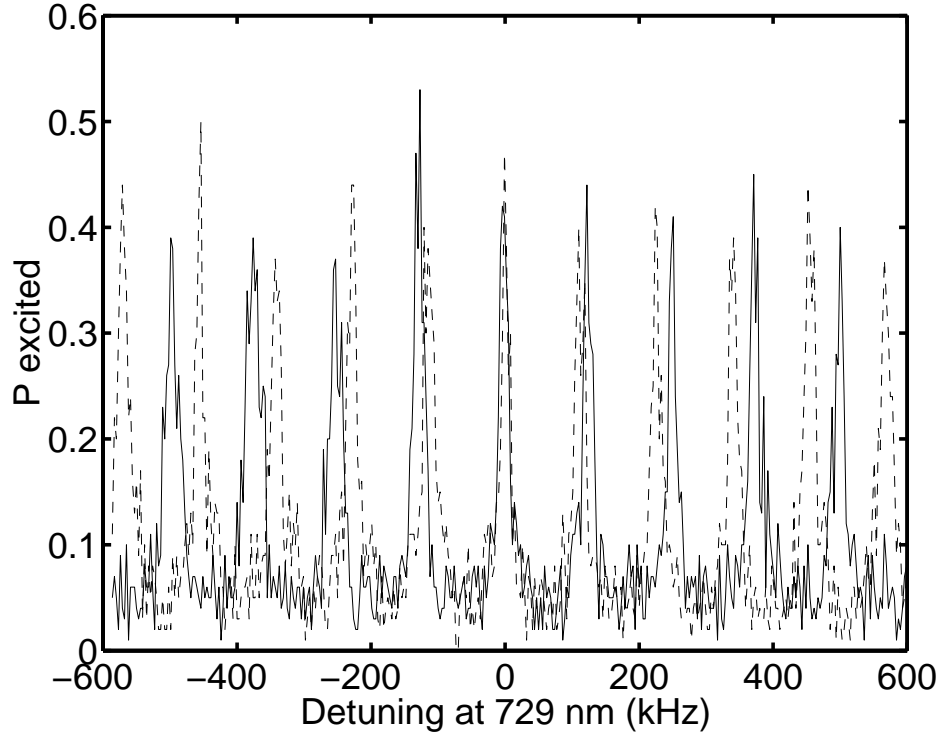


Figure 5.19: Shift of sidebands around carrier (1 ion). For the solid plot the ring voltages have been increased by about 10 V, resulting in an increase from 113.8 kHz to 124.1 kHz for the axial oscillation frequency ν_z . No line trigger was used.

carrier of the $S_{1/2}(m_J = 1/2) - D_{5/2}(m_J = 5/2)$ Zeeman line. No line triggering has been used. The step width is 500 Hz, 10 scans with 100 experiments per step have been accumulated. The price one pays when trying to increase the number of experiments is that the line center drifts with respect to the AOM frequency axis during data accumulation. During this scan the drift appeared to be at least 6 kHz (the overall accumulation time was 15 min), but we have also seen drifts of up to 30 kHz during the same time span. A Gaussian fit to the line gives a linewidth of 16.8 kHz. We attribute the line broadening mostly to ac stray magnetic fields as discussed before.

5.2.6 Line broadening

As discussed in section (2.3), laser cooling on the quadrupole transition requires some mechanism which reduces the lifetime of the $D_{5/2}$ level so that reasonable cooling rates can be achieved. A preliminary attempt to broaden the transition at 729 nm is shown in Fig. 5.21. For this spectrum the pulse sequence of Fig. 5.8 is modified to allow the laser at 854 nm to irradiate the ion during the same period as the laser at 729 nm. The laser at 854 nm is slightly detuned from resonance on the order of 100 to 200 MHz so that a change of its detuning Δ_{DP} due to drifts has a reduced effect on the effective linewidth Γ'_{SD} given in Equ. 2.8. The precise

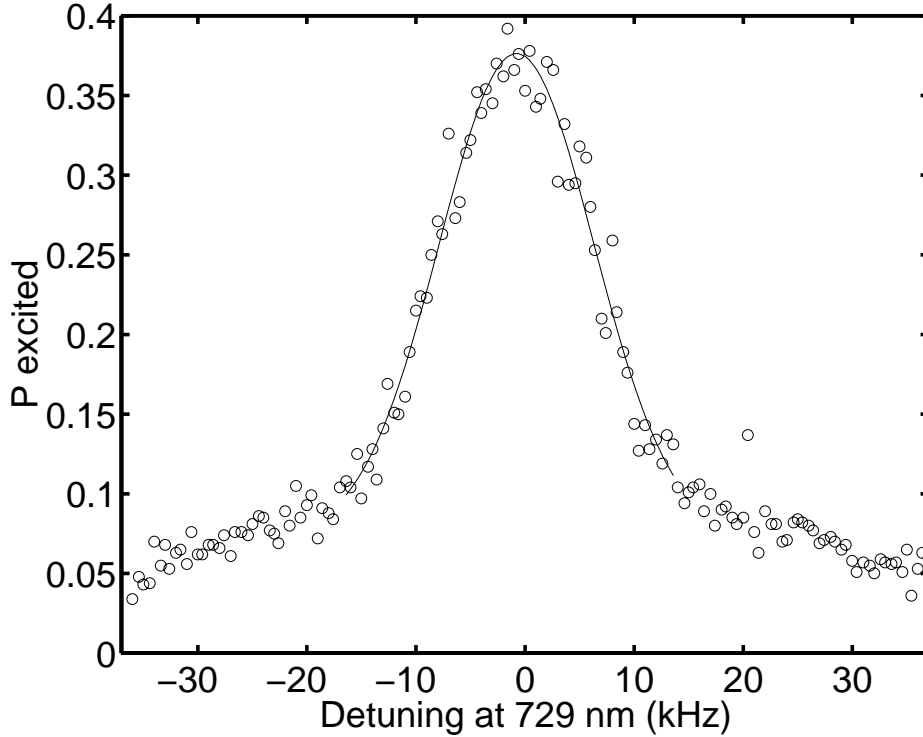


Figure 5.20: Carrier of $S_{1/2}(m_J = 1/2) - D_{5/2}(m_J = 5/2)$ Zeeman line (1 ion) recorded without line triggering. Each data point corresponds to 1000 experiments. The linewidth is 16.8 kHz for a Gaussian fit. The drift of the line center during data acquisition is about 6 kHz.

value of the detuning is not known. Then the power at 854 nm is adjusted to broaden the transition at 729 nm. As can be seen in Fig. 5.21 the main comb and the side combs merge into a single broad line with a width of approx. 50 kHz. Increasing the power at 854 nm leads to even broader lines, but on the other hand the excitation probability is reduced. This can be balanced by increasing the power at 729 nm. For the shown spectrum the power at 729 nm is at its maximum even though the maximum excitation probability is much less than 0.5. It is thus desirable to increase further the power at 729 nm so that for sideband cooling at 729 nm Rabi frequencies of at least 50 kHz are possible.

5.2.7 Coherent dynamics

As mentioned in chapter 2 a major requirement for quantum computation with cold ions is the ability to apply laser pulses of certain duration to the ions. In particular, for an implementation of the CNOT gate we need the ability to (coherently) drive $\pi/2$ -pulses on the carrier and π and 2π -pulses on the red sideband of the qubit transition. These pulses are applied to the ions when they are either in the ground state or in the first excited state of their trapping potential. Fig. 5.22 shows what happens if the ions are not at these low

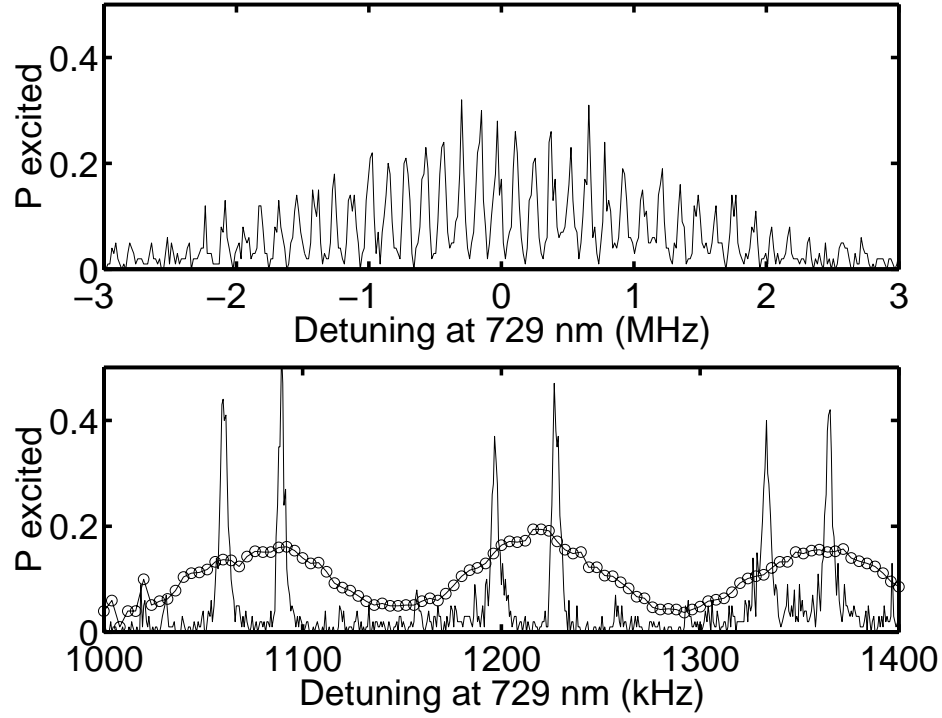


Figure 5.21: $S_{1/2}(m_J = 1/2) - D_{5/2}(m_J = 5/2)$ Zeeman line broadened by laser light at 854 nm. Top: Upper, lower, and main comb merge into one broadened comb. Bottom: Detail of the upper plot at a detuning near $\Delta\nu = 1.2$ MHz. For comparison, the unbroader spectrum is shown. At this detuning, the lower side comb is completely suppressed.

temperatures but instead at temperatures near or above the Doppler limit of our trap. For an evaluation of the excited state probability P_{\uparrow} , we have to refer to Eq. (2.24) with typically $\bar{n} \gg 1$. The Lamb-Dicke parameter η was chosen to be 0.25. For the given direction of the laser beam this corresponds to an axial trap frequency of 130 kHz. For an ion in the ground state $|0\rangle$ of the trapping potential one gets the usual Rabi floppings given by the bare Rabi frequency $\Omega = \Omega_{0,0}$. In this plot the value of $2\pi \cdot 50$ kHz was chosen for Ω which seems to be reasonable in our current experiment⁵ (see below). At higher temperatures the contributions from transitions with $n = n' > 1$ become significant. Because the Rabi frequencies involved are all different the excitation probability collapses quickly to a value near 0.5. In particular, the initial slope of the curve is not as steep because the Rabi frequencies $\Omega_{n,n}$ for $n > 1$ are all smaller than $\Omega_{0,0}$. This is shown in Fig. 5.23 which plots the Rabi frequencies $\Omega_{n,n}$ for excitation on the carrier as a function of n for $\eta = 0.25$ and $\eta = 0.1$. The lower plot of Fig. 5.22 shows the role of decoherence for an ion at the Doppler limit. For the decoherence time $\tau = 1/\gamma$ values have been chosen which are much below, close to, and much above the

⁵As one can see in Fig. 5.22 for the dashed-dotted plot, the angular frequency of oscillation is slightly smaller than $2\pi \cdot 50$ kHz. Evaluation of Eq. 2.20 shows that this is because η is larger than zero.

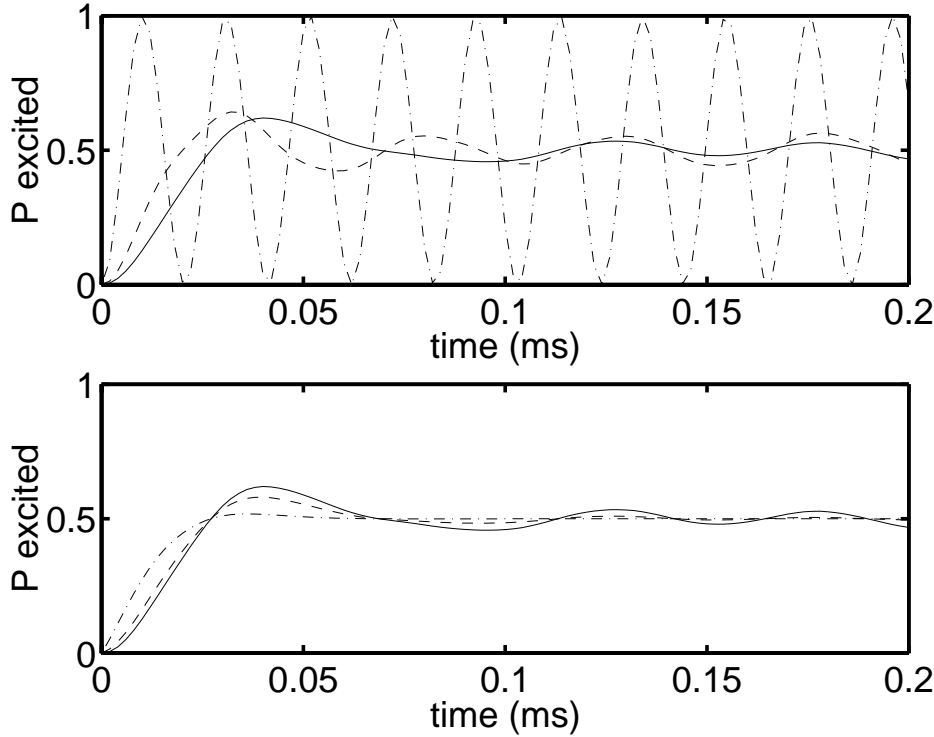


Figure 5.22: Occupation probability P_{\uparrow} of excited state as a function of pulse length for excitation of the carrier ($\eta = 0.25$, $\Omega = 2\pi \cdot 50$ kHz). See Eq. (2.24). Top ($\gamma = 0$): (dashed-dotted) Ion in the ground state $|0\rangle$, (dashed) ion at the Doppler limit ($\bar{n} = 70$), (solid) ion at 5 times the Doppler limit ($\bar{n} = 350$). Bottom: P_{\uparrow} for $\bar{n} = 350$ with $1/\gamma = \tau = 10 \mu\text{s}$ (dashed-dotted), $1/\gamma = \tau = 100 \mu\text{s}$ (dashed), $\gamma = 0$ (solid).

values we currently expect. In comparison to the collapse due to the different Rabi frequencies the effect of a decoherence time $\tau = 100 \mu\text{s}$ does not seem to be very significant⁶.

Fig. 5.24 shows a first scan of the pulse duration on the carrier of the qubit transition. For this scan the laser frequency at 729 nm was set to the center of the carrier. Then pulsed spectroscopy was used while increasing the pulse length at 729 nm from $1 \mu\text{s}$ to $150 \mu\text{s}$. The curve is to be compared with the solid curve in the plots of Fig. 5.22. The excitation probability peaks after approximately $50 \mu\text{s}$ and then levels off at a value of 0.42. This value, which does not agree with the expected value of 0.5, may be the result of imperfect state preparation in the $S_{1/2}(m_J = 1/2)$ ground state. At this point, we do not know for sure that is the dominant effect that causes the excitation probability to collapse within approximately $100 \mu\text{s}$. Assuming that the collapse is due to the different Rabi frequencies we can estimate

⁶The magnitude of the coherence time is estimated from the width of the resonances in the absorption spectrum as before.

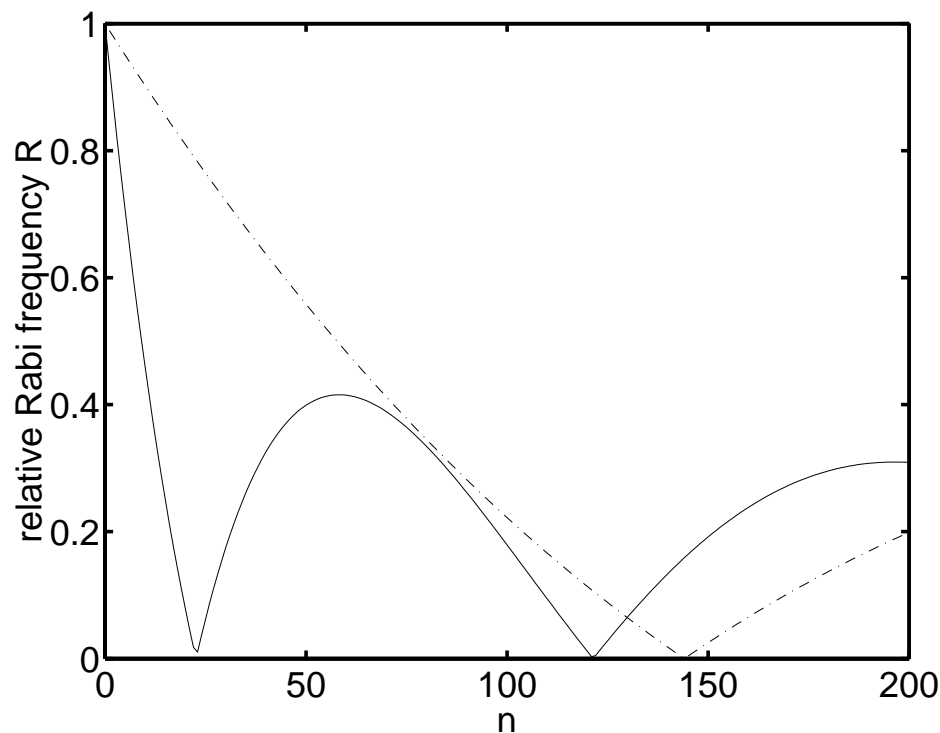


Figure 5.23: Relative Rabi frequency $R(n) = \Omega_{n,n}/\Omega_{0,0}$ on the carrier as a function of n for $\eta = 0.25$ (solid) and $\eta = 0.10$ (dashed-dotted). Given the direction of the laser beam at 729 nm this corresponds to trap frequencies of $\nu_z = 130$ kHz and $\nu_z = 600$ kHz, respectively. It can be seen that for low n and $\eta = 0.25$ the Rabi frequency decreases rapidly to zero. For increasing n it then shows an oscillating behavior.

that the bare Rabi frequency is of the order of $\Omega = 2\pi \cdot 50$ kHz.

5.2.8 Discussion

In this chapter it was shown how high resolution spectroscopy is used to measure the sideband spectrum of a single ion in the linear trap. From this sideband spectrum a temperature can be inferred which is about 10 times above the Doppler limit. We expect that this temperature can be reduced to the Doppler limit temperature by optimizing laser parameters for the lasers at 397 and 866 nm. This temperature is much too high for the application of trapped ions to quantum computation. The next steps are thus to further reduce the temperature by more refined cooling techniques. In addition the axial trap frequency ν_z can be increased. This effectively reduces \bar{n} for a given temperature. In particular, increasing ν_z will simplify the absorption spectrum. A simplification is needed because different combs overlap and thus make it technically difficult to assign a chosen sideband to one of the combs. Temperature measurements which rely on measuring the width of an entire comb can then be carried

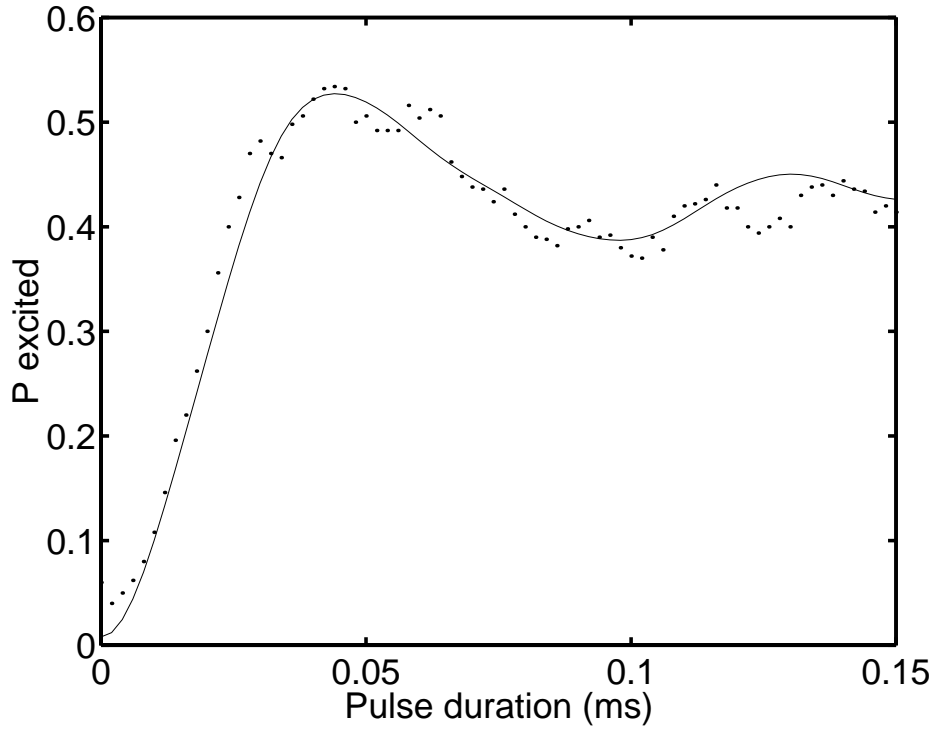


Figure 5.24: Scan of pulse duration on carrier. The excitation probability collapses due to the different Rabi frequencies $\Omega_{n,n}$. Each point corresponds to 500 experiments. Line triggering was used. For comparison, the solid line is a plot of Eq. (2.24) with $\gamma = 0$, $\eta = 0.25$, $\Omega = 2\pi \cdot 50$ kHz and $\bar{n} = 500$.

out faster. In particular, sideband cooling should be much easier if only a few sidebands are present. On the other hand, increasing ν_z should be weighted against a reduced ion-ion spacing. Here, a compromise needs to be found so that addressing of individual ions with a focused laser beam is still possible. ν_z should therefore not be increased much above 500 or 600 kHz.

6 Summary and Outlook

This work has presented the setup of a linear ion trap optimized for trapping a small number of Ca^+ ions and performing quantum gate operations between them. This thesis is the first snapshot of ongoing work which will most likely yield further interesting results in the near future. So far, we have succeeded in trapping and controlling a string of ions. We have shown that compensation of micromotion for such a string is possible. We have studied the motion of a string of ions and we have recorded a movie of how individual atoms move in a trap. We have recorded excitation spectra which show dark resonances for more than one ion. Finally, we have done high resolution spectroscopy with a resolution of better than $\frac{\Delta\nu}{\nu} = 5 \cdot 10^{-12}$ on the quadrupole $S_{1/2}(m_J = 1/2) - D_{5/2}(m_J = 5/2)$ transition which will serve as our first qubit transition candidate. First spectra have been taken which show the broadening of the quadrupole transition in the presence of a quenching laser at 854 nm. Scans of the pulse length at 729 nm reveal a rapid collapse of the excitation probability due to incommensurate Rabi frequencies. With the help of sideband spectroscopy we will be able to test various cooling schemes needed to prepare the ground state of the ions' motion in the trap.

The goals for the immediate future are:

- **Increasing the axial trap frequency by a factor of approx. 3 to 4.** A higher axial frequency ν_z will lead to a lower occupation number \bar{n} and reduce the number of sidebands in the absorption spectra.
- **Linewidth reduction.** With the reduction of the observed linewidth and a reduced \bar{n} it will be possible to see Rabi floppings and to do Ramsey spectroscopy on the quadrupole transition.
- **Test of second laser cooling stage.** The ability to record a sideband spectrum allows us to test various further cooling schemes such as Doppler and sideband cooling on the quadrupole transition. Also, we might test other cooling schemes such a polarization-gradient cooling to reach sub-Doppler temperatures.
- **Addressing individual ions.** One of the prerequisites for quantum computation with cold ions is the ability to address the ions individually. In our trap, with large ion-ion spacing (10 to 20 μm), this can be achieved by focused laser beams directed by an acousto-optical modulator. This should even be possible with an increased trap frequency ν_z .

Currently, to achieve these goals, major improvements concerning alignment, stability, and resolution are under way:

- **Installation of new trap electrodes.** Presently, we are limited with the axial trap frequency to below 200 kHz. The reason is given by slight misalignments of the trap electrodes which put a limit to the ability to compensate for micromotion. Therefore, we have designed a geometrically more precise and more rigid electrode configuration which will replace the old one.
- **Drift stabilization for the repumping lasers at 866 and 854 nm.** So far, these lasers are not locked to a stable reference and hence their wavelength needs to be adjusted every 30 to 60 min. In particular, the drift of the laser at 866 nm has a large influence on the effectiveness of Doppler cooling and on the rate of fluorescence at 397 nm. Hence, the diode lasers will be locked to either a highly drift stable reference resonator or to a Cesium saturation dip by means of a transfer cavity.
- **Intensity stabilization for the fluorescence laser at 397 nm and for the qubit laser at 729 nm.** The fluctuations caused by the laser at 397 nm directly translate to varying PMT counts. Especially for more than one ion and for short exposure times it becomes increasingly difficult to discriminate the count rates. For the laser at 729 nm it is important that we are able to drive $\pi/2$, π and so forth pulses. Instead of stabilizing the intensity one could measure the pulse area and switch off the laser at just the right time when the desired pulse area is reached.
- **Ac-magnetic field compensation.** So far, the resolution on the qubit transition is limited by fluctuating magnetic fields at the mG level. An immediate solution to this problem is to line trigger the entire experiment as we have done up to now. The next steps will be to install μ -metal shielding around the trap for passive ac-magnetic field suppression and to use highly sensitive magnetic field sensors and compensation Helmholtz coils for active compensation.
- **Power optimization for the laser at 729 nm.** Power on this transition is crucial for laser-cooling. Therefore, it is desirable to effectively transfer the power from the laser to the experiment. Currently, much power is lost because we are using an AOM at 600 MHz in double pass which results in low efficiency (80% of power loss). This AOM has so far been necessary in order to be able to tune to the right frequency with respect to the stable reference cavity. Knowing the frequency we can now replace this AOM with a more efficient one at a lower center frequency.

In the near future, we plan to do the following:

- **Drive Raman transitions between the $D_{3/2}$ and $D_{5/2}$ levels.** Because coherence times on the quadrupole transition are basically limited by the coherence time of the laser, we do not expect to be able to realize more than a few gates. This problem will be remedied when we switch to a Raman transition driven by two phaselocked lasers at 850 and 854 nm, so that phase noise cancels out and much longer coherence times become possible.

7 Appendix

7.1 Ca^+ energy levels

For this work we have chosen $^{40}\text{Ca}^+$ which does not possess a nuclear spin and therefore has no hyperfine structure. Ionized Calcium has the electrode configuration of Argon with an additional electron. Hence, the resulting configuration for the outer electron is similar to Hydrogen. The major difference is the fact that the 3D-levels lie between the ground state $4^2\text{S}_{1/2}$ and the $4^2\text{P}_{1/2}$ level. Fig. 7.1 shows all seven relevant transitions. Five of these are

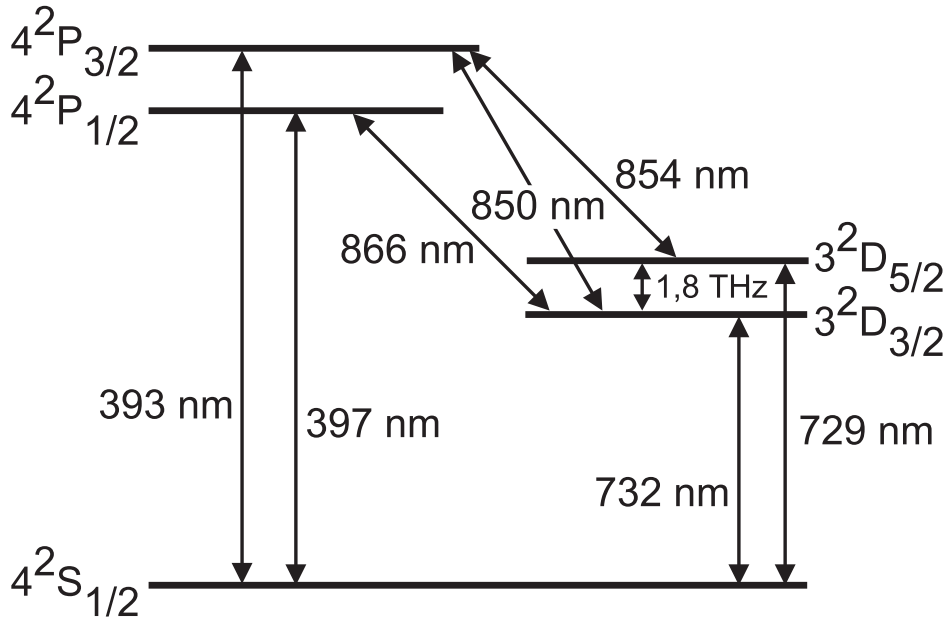


Figure 7.1: Relevant $^{40}\text{Ca}^+$ levels and transition wavelengths.

dipole transitions, the other two (at 729 and 732 nm from the ground state to the D levels) are electric quadrupole transitions. The following tables list the natural lifetimes and the wavelengths [31].

		$\text{S}_{1/2} \leftrightarrow \text{P}_{1/2}$	$\text{S}_{1/2} \leftrightarrow \text{P}_{3/2}$	$\text{P}_{1/2} \leftrightarrow \text{D}_{3/2}$	$\text{P}_{3/2} \leftrightarrow \text{D}_{3/2}$	$\text{P}_{3/2} \leftrightarrow \text{D}_{5/2}$
τ_{nat}	ns	7.7(2)	7.4(3)	94.3	901	101
λ_{air}	nm	396.847	393.366	866.214	849.802	854.209

		$S_{1/2} \leftrightarrow D_{5/2}$	$S_{1/2} \leftrightarrow D_{3/2}$
τ_{nat}	s	1.045	1.080
λ_{air}	nm	729.147	732.389

The transition at 397 nm is used for Doppler laser-cooling and for fluorescence collection. Some of the decay from the $P_{1/2}$ level goes to the $D_{3/2}$ level. This level does not decay to the $D_{1/2}$ ground state via a dipole transition because of the angular momentum selection rules for dipole transitions. Only higher order transitions such as an electric quadrupole transition (at 732 nm) are possible. The lifetime of about 1 s results from the much lower transition probability than for dipole transitions. Hence, for all practical purposes the spontaneous decay from the $D_{3/2}$ level to the ground state can be neglected, and a repumping laser at 866 nm is needed to prevent optical pumping into this level. Ca^+ , neglecting the Zeeman sub-structure (see below), offers therefore, to a good approximation, a so-called Λ -system in which two lower lying stable levels are coupled to a common upper level ($P_{1/2}$) via dipole transitions.

Ca^+ offers another quadrupole transition. This is the one at 729 nm coupling the $S_{1/2}$ ground state to the $D_{5/2}$ level. The lifetime of this level is also about 1 s. In contrast to the $D_{3/2}$ state the $D_{5/2}$ level is not coupled to the $P_{1/2}$ level. Fluorescence on the 397 nm transition can therefore be used to discriminate between the $S_{1/2}$ ground state and the $D_{5/2}$ level. Zeeman sublevels of these two levels can be used to form a two-level system which can be used as a qubit.

Both D-levels are coupled to the $P_{3/2}$ level via dipole transitions around 850 nm. Lasers on these transitions can thus be used to pump out the D-levels via the $P_{3/2}$ level.

7.2 Zeeman structure

The energy splitting depending on magnetic field strength B is given by the well known formula

$$\Delta E = g_J \mu_B B m_J \quad (7.1)$$

with

$$g_J = 1 + \frac{J(J+1) + S(S+1) - L(L+1)}{2J(J+1)} \quad (7.2)$$

Here, μ_B is Bohr's magneton and g_J is called the Lande factor.

	$S_{1/2}$	$P_{1/2}$	$P_{3/2}$	$D_{3/2}$	$D_{5/2}$
g_J	2	2/3	4/3	4/5	6/5

7.2.1 Dipole transitions $S_{1/2} - P_{1/2}$ and $P_{1/2} - D_{3/2}$

The Zeeman splitting gives rise to the following level scheme:

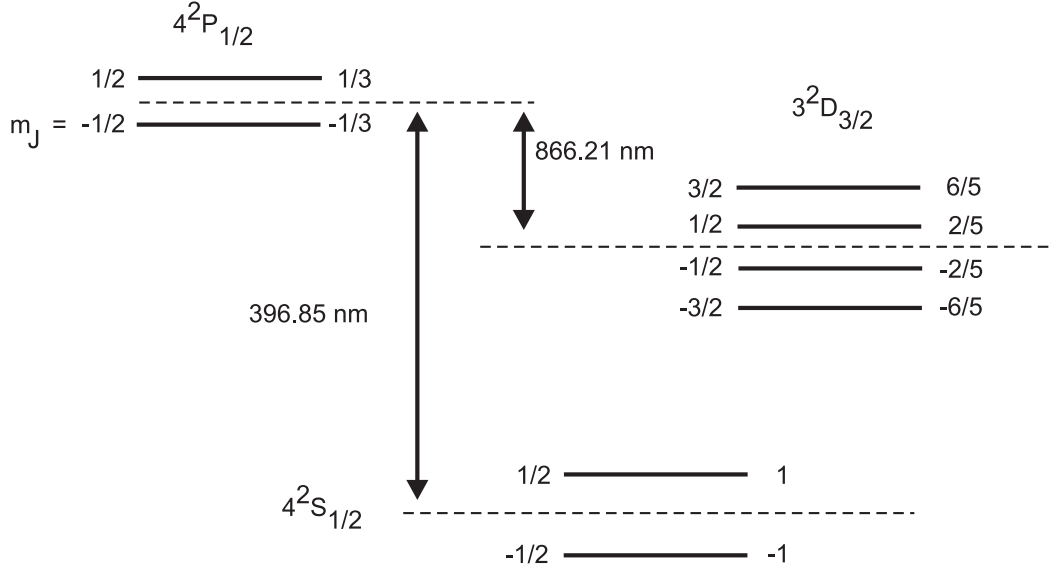


Figure 7.2: Zeeman splitting for the $S_{1/2} - P_{1/2}$ and $P_{1/2} - D_{3/2}$ transitions in $^{40}\text{Ca}^+$. On the right the numbers denote the product $m_J g_J$.

7.2.2 Quadrupole transition $S_{1/2} - D_{5/2}$

The quadrupole transition $S_{1/2} - D_{5/2}$ splits into 10 Zeeman components in the presence of a weak magnetic field \mathbf{B} (see Fig. 7.3 and Fig. 7.4). The following table shows which of the components can be excited by a laser depending on the direction of the wavevector \mathbf{k} and the choice of polarisation \mathbf{E} . Linearly polarized light is denoted by π , circularly polarized light by σ^\pm .

$\mathbf{k} \parallel \mathbf{B}$	$\mathbf{k} \parallel \mathbf{B}$	$\mathbf{k} \perp \mathbf{B}$	$\mathbf{k} \perp \mathbf{B}$	$\mathbf{k} \perp \mathbf{B}$
$\pi(\mathbf{E} \perp \mathbf{B})$	σ^\pm	$\pi(\mathbf{E} \parallel \mathbf{B})$	$\pi(\mathbf{E} \perp \mathbf{B})$	σ^\pm
$\Delta m = \pm 1$	$\Delta m = \pm 1$	$\Delta m = \pm 1$	$\Delta m = \pm 2$	$\Delta m = \pm 1, \pm 2$

The relative line strengths of the Zeeman resonances and the detuning from the Bohr frequency are shown in Fig. 7.4.

7.3 Possible qubit candidates

In the following I will discuss the advantages and disadvantages of several transitions of $^{40}\text{Ca}^+$ which can be used as a qubit transition. They are shown in Fig. 7.5. All of these transitions are possible candidates because of their long lifetimes and convenient access by laser excitation. Unfortunately, all of the following schemes require at least 4 lasers at different wavelengths.

Quadrupole $S_{1/2}$ to $D_{5/2}$ transition: For us, the biggest advantage of this transition is the fact that it is the same transition as the one that we are using for high resolution spectroscopy (i. e. temperature measurements) and which we plan to use for laser-cooling. On the other

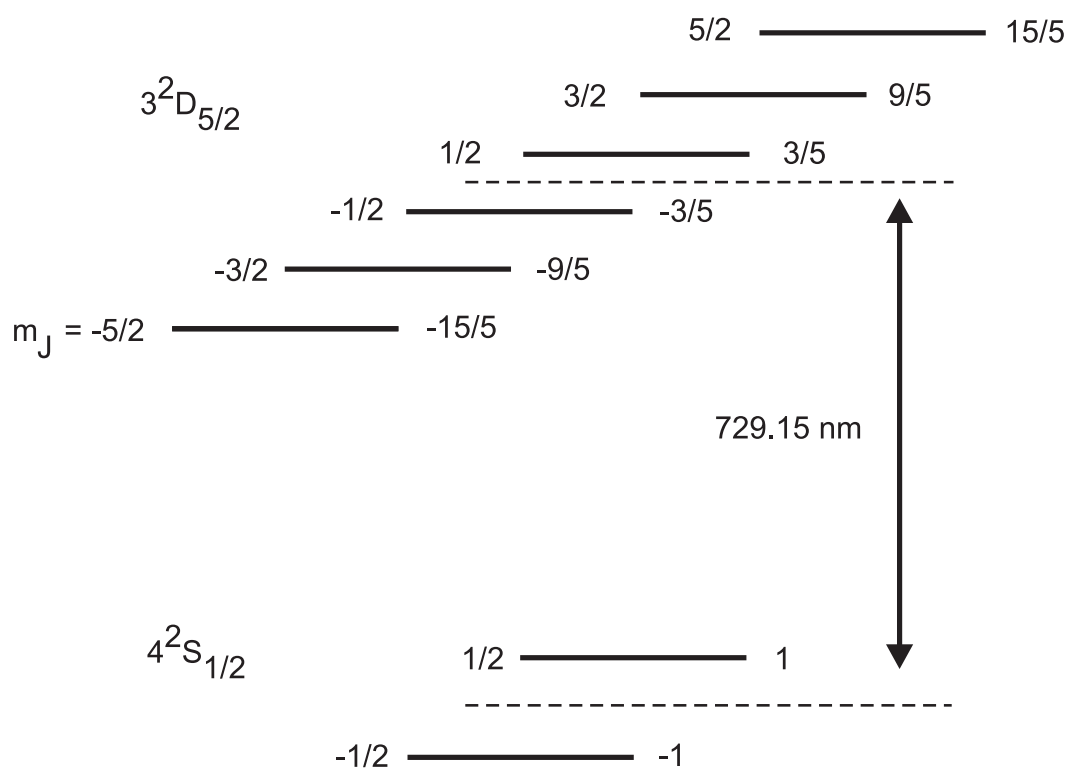


Figure 7.3: Zeeman splitting for the $S_{1/2} - D_{5/2}$ transition in $^{40}\text{Ca}^+$. On the right the numbers denote the product $m_J g_J$.

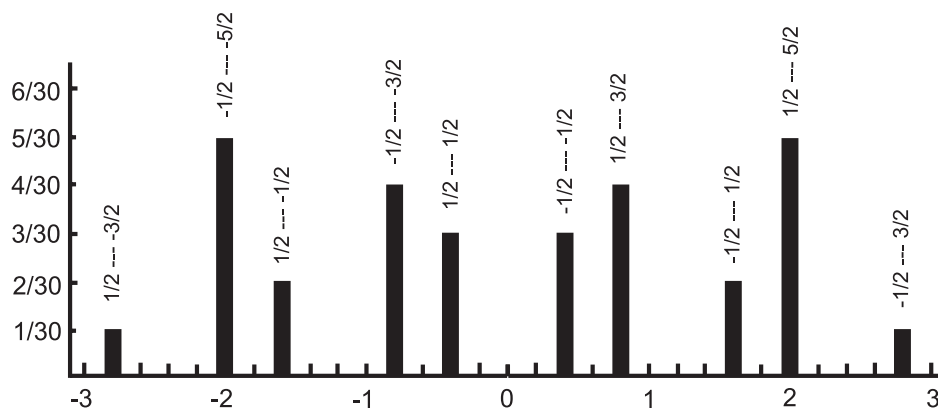


Figure 7.4: Zeeman resonances of the $S_{1/2} - D_{5/2}$ transition in $^{40}\text{Ca}^+$. The x-axis shows the detuning from Bohr's frequency in unit of Bohr's magneton. The y-axis shows the relative line strength.

hand the biggest drawback is the fact that all coherent evolution on this transition is limited by the performance of the 729 nm laser which drives this transition, namely its short term

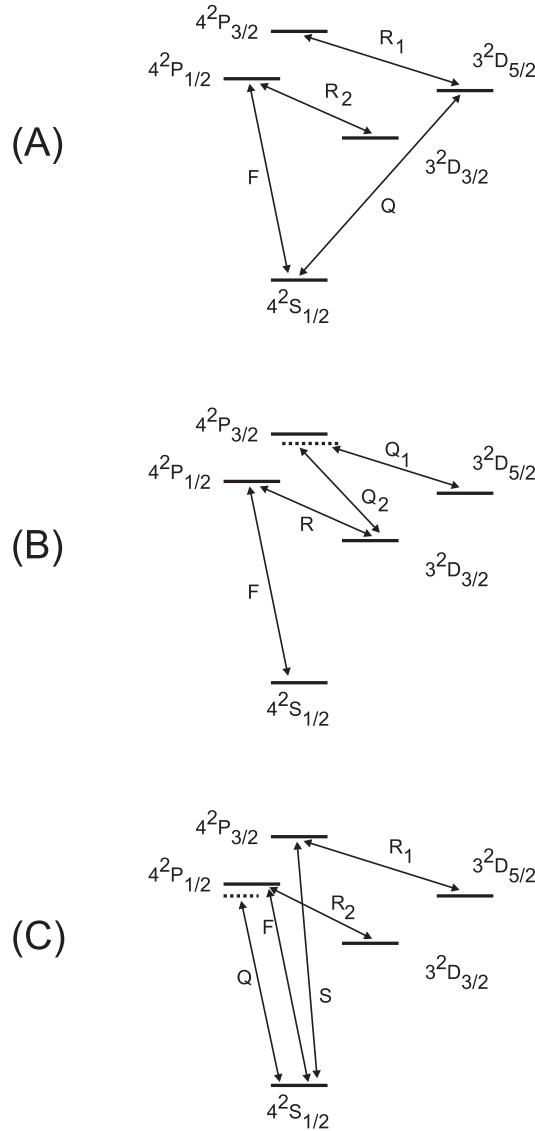


Figure 7.5: Qubit candidates for $^{40}\text{Ca}^+$: (A) Quadrupole $S_{1/2} - D_{5/2}$ transition. (B) Raman $D_{3/2} - D_{5/2}$ transition. (C) Raman $S_{1/2}(m_J = \pm 1/2) - S_{1/2}(m_J = 1/2)$ transition. Q is the qubit transition. Repumping lasers are denoted by R, F is the fluorescence transition, and S is the shelving laser. In (C) the necessary Zeeman splitting is not shown. Laser Q is a Raman laser, i. e. two lasers whose difference frequency is given by the Zeeman splitting. Laser F also needs to have two frequency components to prevent pumping into one of the Zeeman levels.

stability and its drift rate. Therefore, there is no real alternative to using a highly stabilized Ti:Sapphire laser which is locked to a highly stable reference such as a narrow linewidth ULE cavity suspended in vacuum. Though there might be a chance to use a diode laser for the

analysis purposes (it is well possible with some effort to stabilize a diode laser below 10 kHz), only a major effort would allow to use a diode laser if one requires coherence times on the order of 1 ms and longer. Also, there is the additional problem that no laser diodes are available which lase at 729 nm at room temperature. Here, the only solution is to cool a 750 nm laser diode to about -50°C requiring a vacuum chamber and some effort. In any case, we have to rely on a relatively expensive and complicated laser system. Another problem associated with this transition is its first order magnetic field sensitivity. This means that magnetic field drifts and ac magnetic fields need to be compensated for.

Raman $D_{3/2}$ to $D_{5/2}$ transition: Here, the major advantage is the possibility to drive this transition in Raman configuration using two phase locked diode lasers slightly detuned from the $P_{3/2}$ level, one at 850 nm and the other at 854 nm, to get rid of all laser frequency and phase fluctuations. Using a Raman transition mimics the situation in [17] where hyperfine sublevels of the $S_{1/2}$ ground state in ${}^9\text{Be}^+$ are used. There are two problems, one technical and the other of more fundamental nature: To lock these two lasers together one needs to bridge the 1.8 THz gap between the $D_{3/2}$ and $D_{5/2}$ levels (for Be^+ , the splitting is 1.25 GHz). This can be achieved, but only at the expense of a third diode laser at about 852 nm which drives a comb generator (EOM) to modulate sidebands onto the light, which stretch out to at least 0.9 THz so that one can lock the two lasers to one of these sidebands. Currently, we are setting up such a system. The second problem with using this Raman scheme is the fact that we are not coupling ground states, so that this Raman transition does not seem practical for laser cooling. In particular, there is no cycling transition. Spontaneous emission needed for cooling will most likely carry us out of the system.

Raman $S_{1/2}(m_J = \pm 1/2)$ to $S_{1/2}(m_J = 1/2)$ transition: Again, one would mimic the situation in [17]. In order to resolve the Zeeman sublevels of the $S_{1/2}$ level a magnetic field on the order of 50 G or more is needed to achieve a splitting. One would then drive Raman transitions between these levels, and one could also use this scheme for Raman sideband cooling, just as in the case of Be^+ . A major problem though is the fact that state detection is difficult. Using a laser at 393 nm to couple one of the $S_{1/2}$ Zeeman sublevels to the $P_{3/2}$ level for a cycling transition is not practical because of the decay into the lower lying D levels. This decay can be repumped, but only with the possibility of ending up in the other $S_{1/2}$ Zeeman sublevel. On the other hand, one could rely on the fact that most of the decay into the D levels goes into the $D_{5/2}$ level ($\simeq 90\%$). This level could therefore be used for shelving. State detection would then have a 10% error. Unfortunately, even if a laser on the quadrupole transition is not needed for this scheme, it still requires the laser at 393 nm. Also, because the Raman laser at 397 nm cannot be used for fluorescence scattering (because it is far detuned from the dipole transition), an additional laser at 397 nm is required.

7.4 New trap design

The electrode configuration used so far in this work has the disadvantage of slight geometrical misalignment. This is due to the fact that the distances between the electrodes have been arranged by hand. In particular, the centers of ring the electrodes do not perfectly lie on the

longitudinal trap axis given by the quadrupole electrodes. The ring electrodes therefore exert a force on the ions which is not quite parallel with the trap axis. The component of the force perpendicular to the trap axis therefore needs to be compensated for. As mentioned before, we estimate that most of the compensation voltage is needed to achieve this compensation. Also, the trap is sensitive to acoustical vibrations because of lack of spacer material (in fact, we have used macor spacers between all electrodes, but these spacers resulted in a radio-frequency short. Hence, they had to be removed). Therefore, a new trap (see Fig. 7.6) has been constructed which allows for high precision spacing while providing the same optical access and the same geometrical dimensions as the current trap. In addition, the dc electrodes for micromotion compensation have been added to the trap design and do not constitute a separate setup as for the current trap. They also function as rigid spacers between the macor parts that carry the ring electrodes and provide the spacing between the quadrupole electrodes. The ring electrodes are provided by the top part of cylinders which are aligned along the axial

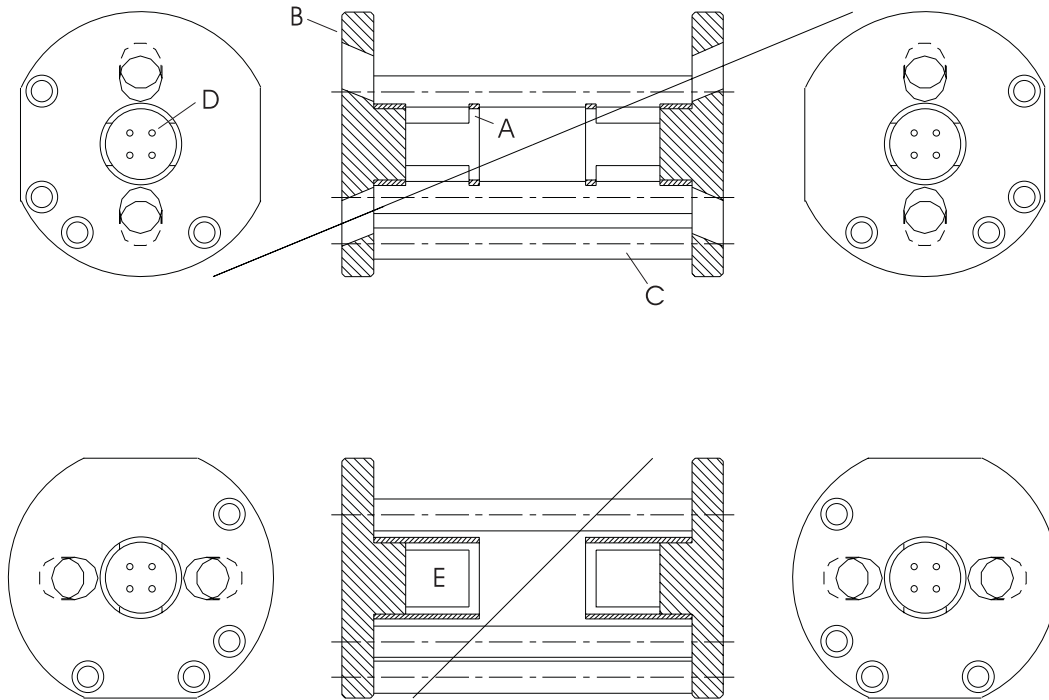


Figure 7.6: Design for new trap. Above: View from top. The straight line is at an angle of 22.5° . A: ring electrode, B: macor spacer, C: compensation electrodes, D: holes for quadrupole electrodes (not shown), E: window for laser beam at 22.5° . Below: View from side. The straight line is at an angle of 45° .

direction of the trap. These cylinders have 'windows' so that a laser beam from an angle of 22.5° can enter the trap. The spacing between the ring electrodes and between the quadrupole electrodes is the same as for the current trap. The distance from the compensation electrodes to the trap center is reduced by a factor of 3. This will also reduce the dc voltages on these electrodes necessary for compensation.

Bibliography

- [1] R. Blatt; Spectroscopy and quantum optics with stored ions, in: Atomic Physics **14**, ed. by D. J. Wineland, C. E. Wieman, and S. J. Smith, AIP New York, (219) 1995.
- [2] D. M. Meekhof, C. Monroe, B. E. King, W. M. Itano, and D. J. Wineland; Generation of nonclassical motional states of a trapped atom, Phys. Rev. Lett. **76**, 1796 (1996).
- [3] C. Monroe, D. M. Meekhof, B. E. King, and D. J. Wineland; A Schrödinger cat superposition of an atom, Science **272**, 1131 (1996).
- [4] J. I. Cirac, A. S. Parkins, R. Blatt, and P. Zoller; Nonclassical states of motion in an ion trap, Adv. At. Molec. Opt. Physics **37**, 238 (1996).
- [5] W. M. Itano, J. C. Bergquist, J. J. Bollinger, J. M. Gilligan, D. J. Heinzen, F. L. Moore, M. G. Raizen, and D. J. Wineland; Quantum projection noise: Population fluctuations in two-level systems, Phys. Rev. A **47**, 3554 (1993).
- [6] J. J. Bollinger, W. M. Itano, D. J. Wineland, and D. J. Heinzen; Optimal frequency measurements with maximally correlated states, Phys. Rev. A **54**, R4649 (1996).
- [7] D. M. Greenberger, M. A. Horne, A. Shimony, and A. Zeilinger; Bell's theorem without inequalities, Am. J. Phys. **58**, 1131 (1990).
- [8] N. D. Mermin; What's wrong with these elements of reality?, Phys. Today, 9 (June 1990).
- [9] W. H. Zurek; Decoherence and the transition from quantum to classical, Phys. Today, 36 (October 1991).
- [10] J. I. Cirac and P. Zoller; Quantum computations with cold trapped ions, Phys. Rev. Lett. **74**, 4091 (1995).
- [11] P. W. Shor; quant-ph/9508027.
- [12] N. A. Gershenfeld and I. L. Chuang; Bulk spin-resonance quantum computation, Science **275**, 350 (1997).
- [13] I. L. Chuang, N. A. Gershenfeld, and M. Kubinec; Experimental implementation of fast quantum searching, Phys. Rev. Lett. **80**, 3408 (1998).
- [14] Q. A. Turchette, C. J. Hood, W. Lange, H. Mabuchi, and H. J. Kimble; Measurement of conditional phase shifts for quantum logic, Phys. Rev. Lett. **75**, 4714 (1995).

Bibliography

- [15] X. Maître, E. Hagle, G. Nogues, C. Wunderlich, P. Goy, M. Brune, J. M. Raimond, and S. Haroche; Quantum memory with a single photon in a cavity, *Phys. Rev. Lett.* **79**, 769 (1997).
- [16] D. P. DiVincenzo; Two-bit gates are universal for quantum computation, *Phys. Rev. A* **51**, 1015 (1995).
- [17] C. Monroe, D. M. Meekhof, B. E. King, W. M. Itano, and D. J. Wineland, Demonstration of a fundamental quantum logic gate, *Phys. Rev. Lett.* **75**, 4714 (1995).
- [18] D. J. Wineland and W. M. Itano; Laser Cooling of Atoms, *Phys. Rev. A* **20**, 1521 (1979).
- [19] R. P. Ghosh; Ion traps, Clarendon Press, Oxford (1995).
- [20] J. D. Prestage, G. J. Dick, and L. Malecki; New ion trap for frequency standard applications, *J. Appl. Phys.* **66**, 1013 (1989).
- [21] G. R. Janik, J. D. Prestage, and L. Malecki; Simple analytic potentials for linear ion traps, *J. Appl. Phys.* **67**, 6050 (1990).
- [22] J. D. Prestage, G. R. Janik, G. J. Dick, and L. Malecki; Linear ion trap for second-order Doppler shift reduction in frequency standard applications, *IEEE Trans. on Ultrasonics, Ferroelectrics and Frequency Control* **37**, 535 (1990).
- [23] R. K. Melbourne, J. D. Prestage, and L. Malecki; Analytic potential in a linear radio-frequency quadrupole trap with cylindrical electrodes, *J. Appl. Phys.* **69**, 2768 (1991).
- [24] J. D. Prestage, G. J. Dick, and L. Malecki; Linear ion trap based atomic frequency standard, *IEEE Trans. on Instrumentation and Measurement* **40**, 132 (1991).
- [25] M. G. Raizen, J. M. Gilligan, J. C. Bergquist, W. M. Itano, and D. J. Wineland; Ionic crystals in a linear Paul trap, *Phys. Rev. A* **45**, 6493 (1992).
- [26] J. D. Prestage, R. L. Tjoelker, G. J. Dick, and L. Malecki; Ultrastable Hg^+ trapped ion frequency standard, *J. of Mod. Optics* **39**, 221 (1992).
- [27] M. G. Raizen, J. M. Gilligan, J. C. Bergquist, W. M. Itano, and D. J. Wineland; Linear trap for high-accuracy spectroscopy of stored ions, *J. of Mod. Optics* **39**, 233 (1992).
- [28] W. Paul and H. Steinwedel; Quadrupole mass filter, *Z. Naturforsch.* **A8**, 448 (1953).
- [29] D. J. Berkeland, J. D. Miller, J. C. Berquist, W. M. Itano, and D. J. Wineland; Minimization of ion micromotion in a Paul trap, *J. Appl. Phys.* **83**, 5025 (1998).
- [30] A. Steane; The ion trap quantum information processor, *Appl. Phys. B* **64**, 623 (1997).
- [31] D. F. V. James; Quantum dynamics of cold trapped ions with application to quantum computation, *Appl. Phys. B* **66**, 181 (1998).
- [32] G. Alzetta, A. Gozzini, L. Moi, and G. Orriols; An experimental method for the observation of rf transitions and laser beat resonances in oriented Na vapour, *Nuovo Cimento B* **36**, 5 (1976).

- [33] I. Siemers; Über die Dunkelresonanz im Anregungsspektrum eines einzelnen gespeicherten Ions, Dissertation, Hamburg (1991).
- [34] T. Hänsch and A. Schawlow; Cooling of gases by laser radiation, *Opt. Commun.* **13**, 68 (1975).
- [35] D. J. Wineland and H. G. Dehmelt, *Bull. Am. Soc.* **20**, 637 (1975).
- [36] W. Neuhauser, M. Hohenstatt, P. Toschek, and H. Dehmelt; Optical-sideband cooling of visible atom cloud confined in parabolic well, *Phys. Rev. Lett.* **41**, 223 (1978).
- [37] D. J. Wineland, R. E. Drullinger, and F. L. Walls; Radiation-pressure cooling of bound resonant absorbers, *Phys. Rev. Lett.* **40**, 1639 (1978).
- [38] F. Diedrich, J. C. Berquist, W. M. Itano, and D. J. Wineland; Laser Cooling to the Zero-Point Energy of Motion, *Phys. Rev. Lett.* **4**, 403 (1989).
- [39] C. Monroe, D. M. Meekhof, B. E. King, S. R. Jeffers, W. M. Itano, D. J. Wineland, and P. Gould; Resolved-sideband Raman cooling of a bound atom to the 3D zero-point energy, *Phys. Rev. Lett.* **75**, 4011 (1995).
- [40] D. J. Wineland; Laser-cooling limits and single-ion spectroscopy, *Phys. Rev. A* **36**, 2220 (1987).
- [41] I. Marzoli, J. I. Cirac, R. Blatt, and P. Zoller; Laser cooling of trapped three-level ions: Designing two-level systems for sideband cooling, *Phys. Rev. A* **49**, 2771 (1994).
- [42] G. Morigi, J. I. Cirac, M. Lewenstein, and P. Zoller; Ground state laser cooling beyond the Lamb-Dicke limit, *Europhys. Lett.* **23**, 1 (1997).
- [43] R. P. Feynman; Simulating physics with computers, *Int. Journ. of Theor. Physics* **21**, 467 (1982).
- [44] D. Deutsch; Quantum computation, *Physics World* **5**, 57 (June 1992).
- [45] A. Ekert; Quantum Computation, in: *Atomic Physics 14*, ed. by D. J. Wineland, C. E. Wieman, and S. J. Smith, AIP New York, 450 (1995).
- [46] A. Steane; Quantum computing, *Rep. Prog. Phys.* **61**, 117 (1998).
- [47] J. J. Bollinger, D. J. Heinzen, W. M. Itano, S. L. Gilbert, and D. J. Wineland; A 303-MHz frequency standard based on trapped Be^+ ions, *IEEE Trans. on Instrumentation and Measurement* **40**, 126 (1991).
- [48] W. Nagourney, J. Sandberg, and H. Dehmelt; Shelved optical electron amplifier: Observation of quantum jumps, *Phys. Rev. Lett.* **56**, 2797 (1986).
- [49] T. Sauter, W. Neuhauser, R. Blatt, and P. E. Toschek; Observation of quantum jumps, *Phys. Rev. Lett.* **57**, 1696 (1986).

- [50] J. C. Bergquist, R. G. Hulet, W. M. Itano, and D. J. Wineland; Observation of quantum jumps in a single atom, *Phys. Rev. Lett.* **57**, 1699 (1986).
- [51] J. I. Cirac, P. Zoller, H. J. Kimble, and H. Mabuchi; Quantum state transfer and entanglement distribution among distant nodes in quantum network, *Phys. Rev. Lett.* **78**, 3221 (1997).
- [52] S. van Enk, J. I. Cirac, and P. Zoller; Ideal communication over noisy channels: a quantum optical implementation, *Phys. Rev. Lett.* **78**, 4293 (1997).
- [53] D. J. Wineland, C. Monroe, W. M. Itano, B. E. King, D. M. Meekhof, C. Myatt, and C. Wood; Experimental primer on the trapped ion quantum computer, *Fortschr. Phys.* **46**, 363 (1998).
- [54] D. F. Walls and G. J. Milburn; *Quantum Optics*, Springer-Verlag Berlin (1994).
- [55] A. Einstein, B. Podolsky, and N. Rosen; Can quantum-mechanical description of physical reality be considered complete?, *Phys. Rev.* **47**, 770 (1935).
- [56] D. J. Wineland, J. J. Bollinger, W. M. Itano, and D. J. Heinzen; Squeezed atomic states and projection noise in spectroscopy, *Phys. Rev. A* **50**, 67 (1994).
- [57] D. Nührmann; *Das große Werkbuch Elektronik*, 5. Auflage, Francis Verlag GmbH, München (1989).
- [58] R. W. P. Drever, J. L. Hall, F. V. Kowalski, J. Hough, G. M. Ford, A. J. Munley, and H. Ward; Laser phase and frequency stabilization using an optical resonator, *Appl. Phys. B* **31**, 97 (1983).
- [59] T. W. Hänsch and B. Couillaud; Laser frequency stabilization by polarization spectroscopy of a reflecting reference cavity, *Opt. Comm.* **35** 441 (1980).
- [60] J. C. Bergquist, W. M. Itano, and D. J. Wineland; Laser stabilization to a single ion, in: *Frontiers in Laser Spectroscopy*, Proc. International School of Physics, Course CXX, ed. by T. W. Hänsch and M. Inguscio, North Holland, Amsterdam, 359 (1994).
- [61] W. Bechter; Frequenzstabilisierung eines Diodenlasers bei 866 nm zur Spektroskopie an Ca^+ -Ionen, Diplomarbeit, Innsbruck (1998).
- [62] C. E. Wieman and L. Hollberg; Using diode lasers for atomic physics, *Rev. Sci. Instrum.* **62**, 1 (1991).
- [63] L. Ricci, M. Weidemüller, T. Esslinger, A. Hemmerich, C. Zimmermann, V. Vuletic, W. König, and T. W. Hänsch; A compact grating-stabilized diode laser system for atomic physics, *Opt. Comm.* **117**, 541 (1995).
- [64] H. C. Nägerl, D. Leibfried, F. Schmidt-Kaler, J. Eschner, and R. Blatt; Coherent excitation of normal modes in a string of Ca^+ ions, *Opt. Express* **3**, 89 (1998), <http://www.osa.org/oearchive/source/4515.htm>.

- [65] H. C. Nägerl, W. Bechter, J. Eschner, F. Schmidt-Kaler, and R. Blatt; Ion strings for quantum gates, *Appl. Phys. B* **66**, 603 (1998).
- [66] <http://heart-c704.uibk.ac.at/>.

Danksagung

Diese Arbeit ist erst durch die Hilfe, die Mühe und die Geduld anderer möglich geworden.

Als erster Stelle möchte ich mich bei meinen Eltern, Prof. Dr. Hans und Dietlinde Nägerl bedanken. Sie haben mir das Studium der Physik ermöglicht und mir stets Unterstützung gewährt.

Meiner Freundin Juliane gebührt ein besonderer Dank für das große Verständnis, das sie mir entgegen gebracht hat, und für vieles weiteres, was nicht in Worte zu fassen ist.

Herrn Prof. Dr. Rainer Blatt bin ich zu großem Dank verpflichtet. Er hat es mir ermöglicht, in seiner Arbeitsgruppe an diesem interessanten Projekt zu arbeiten. Es ist sein Verdienst, daß unsere Arbeitsgruppe im Verlauf dieser Arbeit von Göttingen nach Innsbruck wechselte und daß wir hier in Innsbruck ein Labor mit großzügiger Ausstattung aufbauen konnten. Von seiner kompetenten Anleitung hat diese Arbeit in großem Maße profitiert.

Allen Mitarbeitern unserer Arbeitsgruppe möchte ich danken. Sie alle haben zum Gelingen dieser Arbeit beigetragen. Speziell erwähnen möchte ich Ferdinand Schmidt-Kaler, Dietrich Leibfried, Jürgen Eschner, Wolfgang Bechter, Harald Rohde, Gregor Thalhammer und meine Mitbewohner Christoph Raab und Christian Roos. Ihre Mithilfe an der Arbeit ist von unschätzbarem Wert.

Auch bei den Mitarbeitern der Arbeitsgruppe von Prof. Zeilinger möchte ich mich bedanken. Ihre freundschaftliche Hilfe, insbesondere die von Jörg Schmiedmayer, ist von großem Wert für diese Arbeit. Mathew Daniell danke ich für das Korrekturlesen der Arbeit.

Nicht vergessen möchte ich die Mitarbeiter am Dritten Physikalischen Institut der Universität Göttingen, an welchem mit dieser Arbeit begonnen wurde. Stellvertretend für alle möchte ich Herrn Prof. Dr. Lauterborn danken. Seine Großzügigkeit und Hilfsbereitschaft haben den Umzug nach Innsbruck erheblich erleichtert.

Schließlich danke ich den Mitarbeitern in der Werkstatt, insbesondere den Herren Anton Schönherr und Stefan Haslwanter. Ihre feinmechanischen Arbeiten haben vieles erst ermöglicht.